

UCLA

UCLA Electronic Theses and Dissertations

Title

MRI Contrast Enhancement by Nonlinear Spin Dynamics using Active-Feedback Magnetic Resonance Technique

Permalink

<https://escholarship.org/uc/item/2ps044nh>

Author

Yang, Huimin

Publication Date

2019

Peer reviewed|Thesis/dissertation

UNIVERSITY OF CALIFORNIA

Los Angeles

MRI Contrast Enhancement by Nonlinear Spin Dynamics
using Active-Feedback Magnetic Resonance Technique

A dissertation submitted in partial satisfaction of the
requirements for the degree Doctor of Philosophy
in Chemistry

by

Huimin Yang

2019

© Copyright by

Huimin Yang

2019

ABSTRACT OF THE DISSERTATION

MRI Contrast Enhancement by Nonlinear Spin Dynamics
using Active-Feedback Magnetic Resonance Technique

by

Huimin Yang

Doctor of Philosophy in Chemistry

University of California, Los Angeles, 2019

Professor William M. Gelbart, Chair

Brain tumors are one of the leading death causes worldwide. Magnetic resonance imaging is the most commonly applied imaging technique for brain tumor detection. However, magnetic resonance imaging loses its power when it comes to detect early stage tumor differs from normal tissue in terms of relaxation properties. To overcome this difficulty in early tumor detection, I investigated chaotic spin dynamics generated by radiation damping and utilized a novel MRI technique called the active-feedback to enhance the imaging contrast between normal tissue and early stage brain tumor. The theme of my Ph.D. thesis is summarized as following:

(1) Fixed Point Imaging with Continuous Wave in Presence of Active-feedback Field. Active-feedback field is a time-dependent magnetic field irradiation inspired by a natural radiation damping. It is shown that active-feedback field yields unique fixed points in spin evolution. Spins are excited to opposite directions by the field until they reach their corresponding fixed points.

(2) Contrast enhancement by selective self-excitation with active-feedback magnetic resonance imaging. It is shown by both theory and simulation that active-feedback magnetic resonance technique generates a selective self-excitation process that selectively excites spins and thus makes this technique very sensitive to local magnetic field inhomogeneity. Active-feedback shows potential in detecting tumors at an early stage.

(3) Local-magnetic-field-dependent active-feedback magnetic resonance imaging and its application in early glioblastoma detection. The active-feedback technique is further developed and an advanced technique called local-field-dependent active-feedback magnetic resonance imaging is introduced. This technique is tested on an early stage glioblastoma multiforme model to show its potential in detecting brain tumors at a very early stage.

The dissertation of Huimin Yang is approved.

Charles M. Knobler

Michael Albert Thomas

Benjamin Joel Schwartz

William M. Gelbart, Committee Chair

University of California, Los Angeles

2019

TABLE OF CONTENTS

Abstract	ii
Table of Contents	v
List of Figures	viii
List of Tables	x
List of Symbols	xi
Acknowledgements	xiii
Vita	xv

1. Introduction and Highlights

1.0 Introduction.....	1
1.1 Research Highlights	2
References.....	4

Part I. Fixed Point Imaging with Active-Feedback Field

2. Fixed-Point Imaging with Continuous-Wave in Presence of Active-Feedback Field

2.0 Abstract.....	5
2.1 Introduction.....	6
2.2 Theory and Method.....	7
2.2.1 Nuclear Magnetic Resonance and Magnetic Resonance Imaging	
2.2.2 Radiation Damping and Active-Feedback Field	
2.2.3 Fixed Point with Continuous-Wave	
2.2.4 Computer Simulation	
2.3 Results and Discussion	18
2.3.1 Simulation of Two-Spin Components	
2.3.2 Simulation of 4000-Spin Components	
2.3.3 The Effect of CW Strength	
2.3.4 The Effect of Active-Feedback Time Constant	
2.4 Conclusions.....	32

References.....	34
-----------------	----

Part II. Contrast Enhancement with Active-Feedback Magnetic Resonance

3. Contrast Enhancement by Selective Self-Excitation in Active-Feedback Magnetic Resonance: Insights from Monte Carlo Simulations

3.0 Abstract.....	37
3.1 Introduction.....	38
3.2 Theory and Method.....	40
3.2.1 Nonlinear Spin Dynamics	
3.2.2 Contrast Accumulation Mechanism by Selective Self-Excitation	
3.2.3 Different Contrast Mechanism and Pulse Sequence	
3.2.4 Monte Carlo Simulation	
3.2.5 Computational Parameters	
3.3 Results and Discussion	53
3.3.1 Frequency Selection by Selective Self-Excitation: Simple Spin Models	
3.3.2 Frequency Selection by Selective Self-Excitation: Multi-Cylinder Model	
3.3.3 MR Contrast using “++++” Pulse Sequence	
3.4 Conclusions.....	73
References.....	75

4. Local-Magnetic-Field-Dependent Active-Feedback Magnetic Resonance and its Application in Early Glioblastoma Detection

4.0 Abstract.....	81
4.1 Introduction.....	82
4.2 Theory and Method.....	83
4.2.1 Active-feedback Field and Selective Self-Excitation	
4.2.2 Local-Magnetic-Field-Dependent Active-feedback MR	
4.2.3 Monte Carlo Simulation and Tumor Model	
4.3 Results and Discussion	90
4.3.1 Effect of Active-Feedback Phase on Selective Self-Excitation	
4.3.2 MR Contrast with Local-Magnetic-Field-Dependent Active-Feedback Field	

4.3.3 Contrast Enhancement in Early-Stage GBM	
4.4 Conclusions	106
References	108
5. Conclusions and Outlook	112

List of Figures

2.1 Discription of energy splitting in the presence of magnetic field	8
2.2 The active-feedback electronic device.....	13
2.3 Graphic description of the active-feedback phase with and without local-magnetic-field.....	16
2.4 The SPIO induced magnetic field distribution in Hz.....	17
2.5 The simulation flow chart of the at every step.....	18
2.6 Two-component spin evolution and fixed points with strong active-feedback field.....	19
2.7 Two-component spin evolution and fixed points with weaker active-feedback field	21
2.8 Two-component spin evolution and fixed points in absence with active-feedback field	22
2.9 Graphic description of Rabi cycle and phase accumulation	24
2.10 Relaxation of 4000 spins with SPIO-induced magnetic field without active-feedback field and CW	26
2.11 Relaxation of spins with SPIO-induced magnetic field in the presence of an active-feedback field and CW	27
2.12 The simulation result with changing CW strength ω_1	29
2.13 Simulation results for different active-feedback time constants.....	31
3.1 A graphic description of the mechanism of active-feedback phase on spin system.....	42
3.2 The graphic description of active-feedback phase and its effect on spin evolution	43
3.3 The graphic description of the contrast accumulation mechanism by selective self-excitation process.....	45
3.4 Pulse sequences used for different imaging methods	48
3.5 Simulation model of blood vessels and tissue	50
3.6 Selective self-excitation of spins with different frequency.....	54
3.7 Selective self-excitation of three spin groups with different centers of frequency.....	55
3.8 Selective self-excitation process of three spin groups centered at different frequencies	57
3.9 Simulation results based on the multi-cylinder model with only one π pulse.....	59
3.10 Simulation result (dot) and exponential fit (line) with different oxygen saturation levels....	62
3.11 Simulation result (dot) and exponential fit (line) with different blood-vessel radii	64
3.12 Simulation result (dot) and exponential fit (line) with different diffusion coefficients.....	66

3.13 Simulation result (dot) and exponential fit (line) with different blood volume fractions.....	68
3.14 Maximum contrast with different changes in intrinsic tissue properties	70
4.1 Demonstration of contrast along z direction created by selective self-excitation	83
4.2 Graphic description of the active-feedback phase with and without local-magnetic-field dependence.....	85
4.3 Graphic description of the local-magnetic-field-dependent active-feedback phase (blue line) and frequency distribution with different blood-oxygen saturation	86
4.4 The evolution of one spin with different feedback phases	90
4.5 The evolution of two spin packets with different active-feedback phases	92
4.6 Decay of magnetization of tissues with different oxygen saturation levels and the contrast using different MR methods	97
4.7 The plot of maximum contrast under local-magnetic-field dependent active-feedback MR with different slopes.....	99
4.8 Frequency distribution of early stage GBM and normal tissue and the difference	102
4.9 Simulation results of normal tissue and early-stage GBM using different MR methods	104

List of Tables

3.1 Experimental parameters used in the multi-cylinder model (fixed value)	52
3.2 Experimental parameters used in the multi-cylinder model (baseline value)	52
3.3 Relaxation time, maximum contrast and contrast enhancement using different methods with different oxygen saturation	63
3.4 Relaxation time, maximum contrast and contrast enhancement using different methods with different blood-vessel radii	65
3.5 Relaxation time, maximum contrast and contrast enhancement using different methods with different diffusion coefficients.....	67
3.6 Relaxation time, maximum contrast and contrast enhancement using different methods with different blood volume fractions.....	69
4.1 Parameters used to model early-stage GBM and healthy tissue	89
4.2 Simulation results of different blood-oxygen saturation ($Y = 0.6$ and $Y = 0.62$) using different methods	98
4.3 Relaxation and contrast for normal tissue and early stage GBM using different methods....	105

List of Symbols

S : spin angular momentum

$\vec{\mu}$: magnetic momentum

\vec{B}_0 : external field along the longitudinal direction

μ_z : the z-component of the magnetic moment

m : magnetic quantum number

\hbar : reduced Planck constant

ΔE : energy gap

E : energy

γ : gyromagnetic ratio

$\delta\omega(\vec{r})$: resonance offset

ω_0 : Larmor frequency

ω_1 : frequency of CW

ν : carrying frequency of CW

\vec{B}_+ : local field on the transverse plane

T_1 : longitudinal relaxation time

T_2 : transverse relaxation time

T_2^* : effective transverse relaxation time

D : self-diffusion constant

R : radius of SPIO

$\Delta\omega_r$: frequency shift on the surface of SPIO

d : distance of spin to the center of SPIO

ϑ : angle between spin position to the longitudinal direction

\vec{m} : normalized magnetization

M_0 : equilibrium magnetization

M_z : longitudinal magnetization

M_{xy} : transverse magnetization

$B_{+,AF}$: active-feedback field

m_+ : normalized transverse magnetization

τ_{AF} : active-feedback time constant

φ : active-feedback phase

B_c : deoxyhemoglobin-induced local magnetic field

Hct: hematocrit

$\Delta\chi$: susceptibility difference

θ : angle between the applied field B_0 and the blood-vessel axis;

a : blood-vessel radius;

r : distance between a point of interest and the center of the vessel cross section in the plane normal to the vessel

ϕ : angle between the vector r and the component of applied field in the plane

Y : oxygenation saturation

$(1 - Y)$: degree of deoxyhemoglobin;

f : blood volume fraction

ACKNOWLEDGEMENTS

I would like to express my sincere gratitude to a number of individuals who have been supporting and motivating me over the past five years.

I want to first thank Dr. Yung-Ya Lin for his guidance through most of my research projects. Dr. Lin served a fundamental role in my Ph.D career. He introduced me to the world of magnetic resonance imaging and provided me great opportunities to work with brilliant people all over the world. His guidance to be an independent researcher and thinker is the greatest treasure of my Ph.D life. I deeply appreciate his constant mentorship. I could never achieve what I have without him. I also want to sincerely thank Dr. Gelbart for his enormous support all the time. I deeply respect his enthusiasm for science and attitudes of life. My Ph.D journey was extra tough sometimes but a conversation with him would bring me light and keep me moving forward. I am so grateful for him and all of the advices I've received from him in both scientific and non-scientific matters. My sincere thanks also go to the rest of my dissertation committee for their support and interest in my research. It includes Dr. Charles M. Knobler, Dr. Albert M. Thomas, and Dr. Benjamin J. Schwartz. They are wise men and always willing to share their insights. Their comments and advices have broadened the scope of my research and their encouragements have kept me motivated in even the darkest moments.

In addition, I am very grateful to Justyna Glodé, Nick Baerg, Anne Carpenter from the graduate office of the Department of Chemistry and Biochemistry at UCLA. They were friendly, patient, and always offering help. They made my Ph.D journey much easier by helping me solve many issues related to both science and life.

I also want to express my thanks to my fellow labmates Chao-Hsiung Hsu, Chencai Wang, Sayoni Ray, Fang-Chu Lin, and Zhao Li for the tireless discussion and their continuous support over the past few years and my friends Yang Deng, Yan Xu, and Wilson Huang for their continuous encouragement. I could not imagine the journey without them. They are the invaluable gift of my life.

Last but not least, I want to thank my parents and grandparents for their endless love, guidance and support. They have witnessed everything in my life—from my joy to my tears. Those short reunions and overseas calls are what encouraged me the most. They give me not only a life but also a meaningful being.

VITA

Education

- Candidate in Philosophy in Chemistry, University of California Los Angeles, Los Angeles, California, June, 2016
- Bachelor of Science in Physics, Fudan University, Shanghai, China, June 2014

Honors & Awards

- ISMRM Trainee (Educational) Stipend from International Society for Magnetic Resonance in Medicine (ISMRM), 2017
- UCLA Doctoral Student Travel Grant from the University of California, Los Angeles, 2017
- Distinguished Graduate of Shanghai, China, 2014
- First Prize of People's Scholarship, China, 2012
- China National Scholarship, China, 2012

Selected Publications & Presentations

- Huimin Yang, Chao-Hsiung Hsu, Yung-Ya Lin, "MRI Signal Enhancement in Early-Stage GBM Detection by Nonlinear Spin Dynamics using Active Feedback Fields" Proc. Intl. Soc. Mag. Reson. Med. Apr. 2017
- Huimin Yang, Chao-Hsiung Hsu, Yung-Ya Lin, "Early Brain Tumor Detection by Selective Self-Excitation in Active-Feedback MRI", Annual University of California Chemical Symposium (UCCS), 2019 accepted

Chapter 1

Introduction and Highlights

1.0 Introduction

Brain tumor is one of the leading death causes worldwide. It is estimated that around 700,000 people in the United States suffer from brain tumor. Among them, 69.1% tumors are benign and 30.1% are malignant¹. More than that, the average survival rate for malignant brain tumor patients is about 35%. Patients living with glioblastoma multiforme, the most commonly found and aggressive brain tumor^{2,3}, have only 5.6% five-year relative survival rate¹. Therefore, successfully enhancing the imaging contrast in early detection of high-grade malignancy, such as glioblastoma multiforme, can significantly increase not only the available treatment options, but also the patient survival rate. To achieve this goal, I investigated chaotic spin dynamics inspired by radiation damping and utilized a novel MRI technique called active-feedback to enhance the imaging contrast between normal tissue and early stage brain tumor.

The theme of my Ph.D. thesis can be divided into two parts and are summarized in this dissertation:

(1) The theory of active-feedback and its effect on spin evolution. Active-feedback field (AFF) is a time-dependent magnetic field irradiation inspired by natural radiation damping. Chapter 2 gives a detailed description and explanation of this active-feedback field and the unique fixed points it yields. It can be shown that spins will move in opposite directions and spin motion stops at the unique fixed point.

(2) Contrast enhancement by selective self-excitation in active-feedback magnetic resonance imaging. Chapter 3 shows that the active-feedback magnetic resonance technique generates a selective self-excitation process that selectively excites spins and makes the technique very sensitive to local magnetic field inhomogeneity. Thus, the active-feedback technique has the potential for detecting tumor in the early stage. In Chapter 4, the active-feedback technique is further developed and an advanced technique called local-field-dependent active-feedback magnetic resonance imaging is introduced. This technique is tested on an early stage glioblastoma multiforme model to show the power in detecting brain tumor at a very early stage.

1.1 Research Highlights

My research achievements regarding contrast enhancement and early tumor detection with active-feedback magnetic resonance technique include:

(1) Developed an original work in fixed-point imaging with continuous wave (CW) in the presence of active-feedback field(AFF). AFF causes nonlinear spin dynamics characterized by nonlinear Bloch Equations. The interference of AFF with CW yields unexpected fixed points not along the direction of equilibrium. Two spins move toward different directions and reach their fixed points on the opposite sides on the Bloch sphere when there is a strong AFF. And two spins keep rotating and do not separate from each other in absence with AFF or when AFF is extremely weak.

(2) Investigated early-stage tumor and normal tissue properties and developed a mathematical model to accurately simulate tissue with different intrinsic properties. The model simulates the blood oxygen level dependent (BOLD) signal based on different tissue properties including blood oxygen saturation level, blood volume fraction, blood vessel radius and diffusion. The results from

simulation match literature value of MRI experiments^{4,5}. Tissue has different relaxation rate with different tissue property. As blood oxygen saturation level or blood vessel radius increases, the relaxation rate decreases; as diffusion coefficient or blood volume fraction increases, the relaxation rate increases.

(3) Utilized active-feedback magnetic technique to enhance image contrast. With a small difference in relaxation property, active-feedback technique enhances contrast by 4 times when compared to T_2 -weighted imaging and enhances contrast by 2 times when compared to T_2^* imaging.

(4) Invented an advanced active-feedback method with local-magnetic-field-dependent phase. When performed on early stage glioblastoma multiforme model, simulation shows that the local-field-dependent active-feedback method generates a contrast 7.2 times greater than that from T_2 -weighted imaging. The contrast enhancement is confirmed by in vivo experiments.

References

- [1] <https://braintumor.org/brain-tumor-information/brain-tumor-facts>
- [2] Louis, D. N., Ohgaki, H., Wiestler, O. D., Cavenee, W. K., Burger, P. C., Jouvet, A., Scheithauer, B. W. Kleihues, P. The 2007 WHO classification of tumours of the central nervous system. *Acta Neuropathol* 2007, 114, 97-109.
- [3] Bleeker, F. E., Molenaar, R. J., Leenstra, S. Recent advances in the molecular understanding of glioblastoma. *Journal of Neuro-Oncology* 2012, 108(1), 11-27.
- [4] Boxerman, J. L., Hamberg, L. M., Rosen, B. R. & Weisskoff, R. M. MR Contrast Due to Intravascular Magnetic Susceptibility Perturbations. *Magnetic Resonance in Medicine* 1995, 34 (4), 555-566.
- [5] Uludag, K., Müller-Bierl, B., Ugurbil, K. An integrative model for neuronal activity-induced signal changes for gradient and spin echo functional imaging. *NeuroImage* 2009, 48, 150-165.

Chapter 2

Fixed Point Imaging with Continuous-Wave in Presence of Active-Feedback Field

2.0 Abstract

Magnetic resonance imaging (MRI) is one of the most commonly used imaging techniques for biomedical diagnostics and imaging because of its low energy and nonionizing radiation. The imaging contrast in magnetic resonance imaging largely depends on the molecular dynamics of different tissues which cause difference in relaxation. Unfortunately, the MRI technique is very limiting when it comes to distinguish tissues with subtle differences in tissue properties. A notorious example is the detection of early stage tumor from normal tissue.

In this work, we take advantage of a novel MR method called active-feedback field (AFF) and continuous-wave (CW) irradiation to enhance the sensitivity to small magnetic susceptibility differences. More than that, this technique produces unique fixed points or constants of motion of spins.

The theory of the active-feedback field with continuous-wave and the resulting fixed-point imaging is presented in this work. Computer simulations are performed to confirm the theory. Simulation results clearly demonstrate the interference of the active-feedback field with continuous-wave in spin motions and the evolution of magnetization to the fixed points. Effects of important active-feedback field and continuous-wave parameters are demonstrated and discussed. Both theory and simulation show that the application of continuous-wave in presence of active-feedback field is sensitive to local field environment and has the potential to distinguish tissues

with small relaxation differences.

2.1 Introduction

Nuclear magnetic resonance first served as imaging tool in 1971. Since then, magnetic resonance imaging (MRI) has been largely used in biomedical imaging and diagnostics due to its advantages such as low-energy and nonionizing radio-frequency radiation¹. The principle of MRI involves three components: a constant magnetic field to which magnetic nuclear spins align; an oscillating magnetic field that perturbs the alignment, usually called radio frequency (RF) pulse; a receiving coil that detects the NMR signal during or after RF pulses².

The applications of MRI range from diagnostic medicine, biomedical research to producing various chemical and physical data. Besides traditional relaxation-based imaging techniques such as T_1 and T_2 weighted imaging, novel MRI techniques such as functional MRI (fMRI), perfusion-weighted MRI and diffusion-weighted MRI have enlarged its application to a much broader area. For example, fMRI uses the blood-oxygen-level-dependent (BOLD) contrast to measure brain activity by detecting changes associated with blood flow³. While MRI provides extensive information on anatomy and physiological processes of the body, because the contrast in MRI comes from different relaxation properties, it loses its power when it comes to a situation where there is only a slight difference in relaxation parameters.

In this work, an active-feedback field (AFF) is introduced to overcome the problem of low sensitivity to local magnetic susceptibility. The AFF is inspired by the natural radiation damping effect that has been shown to produce chaotic dynamics at high fields^{4,5}. According to Lenz's law, the oscillating current in the receiving coil will induce an oscillating magnetic field, that will act on the sample and accelerate the process reestablishing the equilibrium along z direction. In many

MRI experiments, radiation damping produces adverse effects in signal acquisition since the radiation damping field drives spins to the +z axis at a much faster rate than the longitudinal relaxation rate ($1/T_1$)⁶. However, in this work, we take advantage of the chaotic spin dynamics and create an “active-feedback field” that alters spin behavior. The addition of the AFF essentially introduces non-linear spin dynamics that is very sensitive to local-field environment. A home-built electronic device is used to generate and control the AFF as well as to eliminate the natural radiation damping. The device has the function of filtering, phase shifting and amplifying the signal from the receiving coil and converting the signal to an RF pulse and feed the pulse back to the sample. The device can be controlled by computer to modify active-feedback phase and feedback strength, which allows us to select optimal field parameters for different purposes. The effects of active-feedback parameters are demonstrated and discussed in this work.

Continuous-wave (CW) has been largely used in spectroscopy and imaging such as being used to change the effective magnetic field to study relaxation behaviors^{7,8}. Moreover, Warren has previously shown that in a single-spin system, the application of a CW in the presence of radiation damping generates unexpected dynamics⁹. In this work, it is shown by both theory and simulation that the application of weak CW in presence of AFF yields fixed points or constants of motion when the CW is placed off-resonance. And this novel technique is sensitive to the local field and has the potential to differentiate tissues with small relaxation differences.

2.2 Theory and Method

2.2.1 Nuclear Magnetic Resonance and Magnetic Resonance Imaging

Atoms such as ^1H and ^{13}C that have an odd number of protons have non-zero nuclear spin. In the absence of an external magnetic field, the nuclear spin angular momentum S has $(2S + 1)$

degenerate angular momentum states. When an external field B_0 is added to the system along the longitudinal direction, the field perturbs to the nuclear spin and splits the degenerate state into $2S + 1$ different levels¹⁰.

The energy perturbation induced by the external field is described by¹¹:

$$E = -\vec{\mu} \cdot \vec{B}_0 = -\mu_z B_0 = -\gamma m \hbar B_0 \quad (1)$$

where $\vec{\mu}$ is the magnetic moment of the atom; \vec{B}_0 is the external field along the longitudinal direction with magnitude B_0 ; μ_z is the z-component of the magnetic moment; γ is the gyromagnetic ratio; m is the magnetic quantum number, which can take integer values from $-S$ to $+S$; \hbar is the reduced Planck constant. The spin energy is split into $(2S + 1)$ states each with different energy. As shown in figure 1 with $S = 1/2$ and $m = \pm 1/2$.

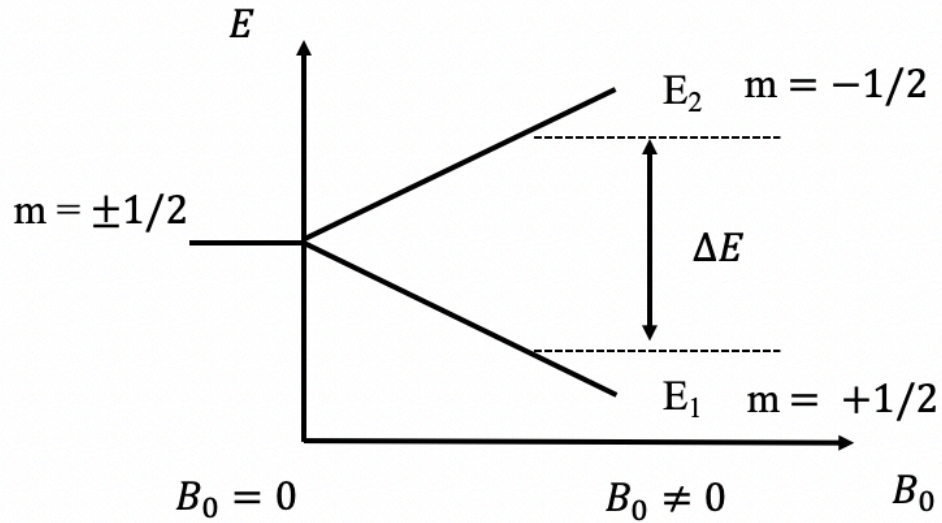


Figure 1. Description of energy splitting in the presence of magnetic field. Spin has a degenerate state without the external field. The degenerate energy level splits into two states one with lower energy ($m = 1/2$) and another with a higher energy ($m = -1/2$).

With spin $S = 1/2$ and $m = \pm 1/2$, the energy gap between two levels is:

$$\Delta E = \gamma \hbar B_0 \quad (2)$$

This energy splitting results in a distribution of population in the two energy levels with slightly more spins in the lower energy level ($m = 1/2$, spin up) and less spins stay in the higher energy level ($m = -1/2$, spin down) in thermal equilibrium. With more spins pointing up, the net result is a small magnetization pointing in the same direction as the external field B_0 . This magnetization has a precessional motion of the direction of the applied magnetic field with Larmor frequency¹²:

$$\omega_0 = -\gamma B_0 \quad (3)$$

When a radio frequency (RF) pulse with a frequency that matches the Larmor frequency of the nuclear magnetization is applied, the energy from the RF pulse will be absorbed by spins. Some of the spins in the lower energy level are excited to the higher energy level, which results a change in spin population¹³. This process is called nuclear magnetic resonance. With different strength and application time, the RF pulse can rotate the magnetization from the original position along $+z$ to a different position. A 90° RF pulse rotates magnetization 90° from $+z$ direction to transverse plane and 180° pulse rotates the magnetization 180° to a position pointing down.

After the RF pulse stops, the magnetization undergoes two types of relaxation processes to reestablish the thermodynamic equilibrium. The nuclear spins that are excited return to thermal equilibrium and the longitudinal component grows to its initial maximum value parallel to B_0 . This process is called T_1 relaxation, “longitudinal relaxation” or “spin-lattice” relaxation¹⁴. Magnetizations that are aligned by an RF pulse will go out of phase and the transverse components of magnetization decay to zero. This process is call T_2 relaxation, “transverse relaxation” or “spin-spin” relaxation¹⁵. T_1 and T_2 are the corresponding relaxation times that can be characterized by

the following equations^{16, 17, 18, 19}:

$$M_z = M_0(1 - e^{-t/T_1}) \quad (4a)$$

$$M_{xy} = M_{xy0}e^{-t/T_2} \quad (4b)$$

where M_0 is the magnetization in thermodynamic equilibrium; M_z and M_{xy} are the longitudinal and transverse component respectively; M_{xy0} is the transverse magnetization under thermal equilibrium.

The relaxation signal can be received through the receiving coil, and transformed into images. Different tissues will have different imaging intensity and contrast due to their difference in relaxation properties, which results in different T_1 and T_2 times.

2.2.2 Radiation Damping and Active-feedback Field

The AFF is inspired by the natural radiation damping effect²⁰⁻²² that has been shown to produce chaotic dynamics at high fields and was first introduced in 2008²³⁻²⁵. AFF drives the magnetization to equilibrium along the z direction faster than the T_1 relaxation. AFF can be seen as a special RF pulse but with two differences. First, AFF always tilts the magnetization back to equilibrium (+z) while the RF pulse drives the magnetization away from equilibrium. Second, the RF pulse drives the magnetization at a constant rate so that the phase away from equilibrium is proportional to the time during which the pulse is applied. However, the AFF drives the magnetization at a changing rate that is dependent on the transverse magnetization. The magnetization is driven faster when there is a stronger transverse magnetization. With AFF, the phase α of magnetization can be expressed by:

$$\frac{d\alpha}{dt} = \gamma B_{AF} = \frac{-\sin\alpha}{\tau_{AF}} \quad (5)$$

where B_{AF} is the AFF and τ_{AF} is the active-feedback time constant, which can be expressed by:

$$\tau_{AF} = \frac{2}{\mu_0 \gamma \eta Q M_0} \quad (6)$$

where μ_0 is the space permeability; η is the number of circles on the receiving coil; M_0 is the net magnetization in the sample, which is affected by the external magnetic field and spin density. The magnitude of AFF is inversely proportional to the feedback time constant. A longer feedback time constant yields a smaller AFF.

AFF is a time-dependent oscillating field added on the transverse plane and it is proportional to the averaged transverse magnetization. AFF only affects the magnetization along the longitudinal direction and does not produce any dephasing. This field is characterized by:

$$\gamma \vec{B}_{+,AF}(t) = \frac{ie^{i\varphi}}{\tau_{AF}V} \int_V \vec{m}_+(\vec{r}, t) d^3\vec{r} \quad (7)$$

where $\vec{B}_+ = B_x + iB_y$, is the field added on the transverse plane; $\vec{m}_+ = m_x + im_y$ is the transpose component of the normalized magnetization; φ is the active-feedback phase that determines the phase difference between the transverse magnetization vector and AFF vector. For a perfectly tuned probe, AFF 90° lag behind the transverse magnetization when $\varphi = 180^\circ$, corresponding to the natural radiation damping which accelerates the process to equilibrium along +z. The AFF can be further expressed by:

$$\begin{aligned} \vec{B}_{+,AF}(t) &= \frac{ie^{i\varphi}}{\gamma \tau_{AF}V} \int_V \vec{m}_+(\vec{r}, t) d^3\vec{r} \\ &= \frac{1}{\gamma \tau_{AF}} \langle i\vec{m}_+(\vec{r}, t) \rangle e^{i\varphi} \\ &= \frac{1}{\gamma \tau_{AF}} (i\langle m_x \rangle - \langle m_y \rangle) e^{i\varphi} \end{aligned} \quad (8)$$

Under a rotation frame, the spin evolution can be described by the Bloch equation:

$$\frac{\partial \vec{m}(\vec{r}, t)}{\partial t} = \gamma \vec{m}(\vec{r}, t) \times \left[\frac{\delta \omega(\vec{r})}{\gamma} \hat{z} + \vec{B}(\vec{r}, t) \right] - \frac{m_z - 1}{T_1} \hat{z} - \frac{m_x \hat{x} + m_y \hat{y}}{T_2} + D \nabla^2 \vec{m}(\vec{r}, t) \quad (9)$$

where $\delta\omega = \omega - \omega_0$ is the frequency difference between the system and the Larmor frequency; $\vec{B}(\vec{r}, t)$ is the total magnetic field; D is the diffusion coefficient; and $\vec{m}(\vec{r}, t) = \vec{M}(\vec{r})/M_{eq}$ is the normalized magnetization with respect to the equilibrium magnetization.

The Bloch equation is linear when the magnetic field is independent of the magnetization, which keeps the cross time in equation (9) the first order. However, when the AFF is applied to the system, this field, which depends on the instantaneous transverse magnetizations renders the equation nonlinear and introduces chaotic spin evolution^{26,27}. Moreover, it is difficult to solve the nonlinear Bloch equation for analytic solution and only numerical solutions can be obtained and used to explain the spin behavior.

A home-built electronic device is used to not only yield the AFF depending on the MRI signal but also to eliminate the natural radiation damping effect that is unstable and uncontrollable^{28, 29}. Both the active-feedback phase and the time constant are adjustable by the electronic device. The principle of the device is shown in figure 2. The device consists of three major parts: a signal amplifier that filters and amplifies the FID signal; a phase shifter that adjusts active-feedback phase and a receiver that receives the FID signal and send out active-feedback pulse sequences.

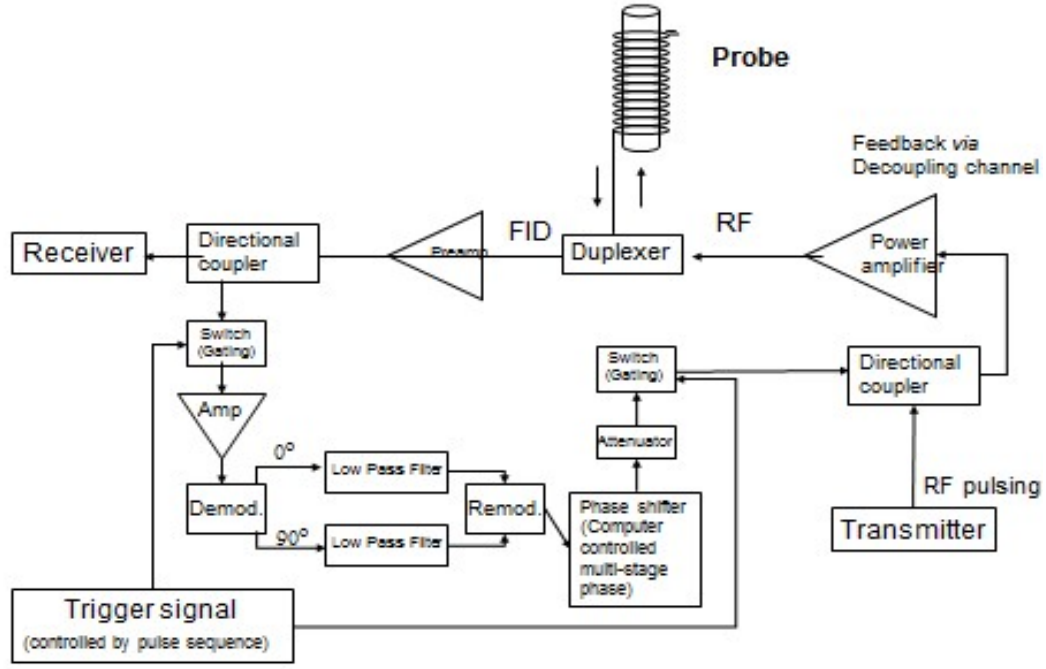


Figure 2. The active-feedback electronic device. It consists of three major parts: a signal amplifier to filter and amplify signal, a phase shifter to adjust phase and a receiver to receive FID signal and send out active-feedback pulse sequence.

2.2.3 Fixed Points with Continuous-wave

A fixed point is defined as no spin evolution. When the relaxation terms are neglected, obviously, this status will occur only when $\vec{m}(\vec{r}, t) \parallel \vec{B}(\vec{r}, t)$ or $\vec{B}(\vec{r}, t) = 0$ as $\vec{m}(\vec{r}, t) \times \vec{B}(\vec{r}, t) = 0$, resulting in $\partial \vec{m} / \partial t = 0$ in eqn. (9). Consider a single spin component, when $\varphi = 180^\circ$, the AFF can be simplified to $\gamma \vec{B}_{+,AF}(t) \propto i \vec{m}_+$ according to eqn. (7), indicating a 90° phase difference in the AFF vector and the transverse magnetization vector on the complex plane, i.e. $\vec{B}_{+,AF}(t) \perp \vec{m}_+$. As a result, with the external field along the +z direction and AFF, $\vec{m}(\vec{r}, t) \times \vec{B}(\vec{r}, t) = 0$ only happens when $\vec{m}_+(\vec{r}, t) = 0$. It can be shown that the fixed-points will happen when $m_z = \pm 1$.

$m_z = +1$, which is simply the equilibrium state, is a stable fixed-point while $m_z = -1$ is an unstable fixed-point.

It was shown by Warren that in a single-spin system, there are unexpected fixed-points that are different from $m_z = \pm 1$ when continuous-wave (CW) irradiation is applied in the presence of radiation damping and the CW is placed off-resonance⁹. Since the AFF has a similar effect with radiation damping, it is reasonable to suggest that the unexpected fixed-points will occur when CW is applied in the presence of AFF as well.

CW is a time-independent oscillating magnetic field that is applied to the transverse plane. It can be shown as:

$$\gamma \vec{B}_{+,cw} = \omega_1 e^{i2\pi v} \quad (10)$$

where ω_1 is the frequency of CW representing how strong the field is; v is the carrying frequency of CW representing the position at which the CW is placed and the degree of the off-resonance. With a proper rotation frame, CW can be reduced to a static magnetic field:

$$\vec{B}_{+,cw} = \omega_1 \hat{x} \quad (11)$$

and the effective magnetic field in the rotation frame is:

$$\gamma \vec{B}_e = \omega_1 \hat{x} + \delta \omega \hat{z} \quad (12)$$

It can be shown that adding CW to the system together with the AFF, $\vec{m} \parallel \vec{B}_e$ no longer yields $\partial \vec{m} / \partial t = 0$ as previously described. Instead, how to generating $\partial \vec{m} / \partial t = 0$ is determined by the active-feedback time constant τ_{AF} and the degree to which the off-resonance CW is placed with respect to magnetization.

The combination of CW with AFF will produce one stable fixed-point and one unstable fixed-point. With a single spin component, the Bloch equation shown in eqn. (9). can be easily broken down to three separate equations in the x, y, z dimensions and the integral in eqn. (7) can

be easily solved. With more spin components, the equations become much more complicated. Even with two spin components, three additional equations are required to be solved simultaneously and the integral in AFF is much more complicated as the relative volume contribution from the two components becomes important. To simplify the situation, we only consider the case in which two components have the same contribution to the integral. The two components have a frequency off-set $\Delta\omega_{ij} = |\delta\omega_i - \delta\omega_j|$ where i, j represents spin i and spin j. The CW is placed in the middle of the two components with $\delta\omega_i = -\delta\omega_j = \delta\omega$ and $\Delta\omega_{ij} = 2|\delta\omega|$. And the effective field for each of the component becomes:

$$\gamma\vec{B}_{e,i/j} = \omega_1\hat{x} + Re\left[\frac{ie^{i\varphi}}{\tau_{AFV}} \int_V \vec{m}_+(\vec{r}, t) d^3\vec{r}\right]\hat{x} + Im\left[\frac{ie^{i\varphi}}{\tau_{AFV}} \int_V \vec{m}_+(\vec{r}, t) d^3\vec{r}\right] + \delta\omega_{i/j}\hat{z} \quad (13)$$

For a weak AFF as compared to CW ($\omega_1\tau_{AF} \gg 1$), the integrals in eqn. (13) are dropped and the effective field can be written by:

$$\gamma\vec{B}_{e,i/j} = \omega_1\hat{x} + \delta\omega_{i/j}\hat{z} \quad (14)$$

It can be easily shown each spin component has two fixed-points, one points in the same direction as $\vec{B}_{e,i/j}$ ($|+\rangle$) and the other one points in the opposite direction with $\vec{B}_{e,i/j}$ ($|-\rangle$). As a result, there will be a total of four states for the two-components system, i.e. $|++\rangle$, $|+-\rangle$, $|-\rangle$, $--\rangle$. However, these states are neither stable fixed points nor unstable fixed points since little perturbation will move the system away.

For a strong AFF ($\omega_1\tau_{AF} \sim 1$), the effect of AFF is not negligible. The integral term $\int_V \vec{m}_+(\vec{r}, t) d^3\vec{r} \neq 0$ in both $|++\rangle$ and $--\rangle$ states since these states have a coherent transverse component that is nonzero, thus, $\vec{B}_{+,AF} \neq 0$. Figure 2(a) shows the situation in which $\vec{B}_{+,AF} \neq 0$ under state $|++\rangle$ and $--\rangle$ and there is a 90° phase difference between $\vec{B}_{+,AF}$ and $\int_V \vec{m}_+(\vec{r}, t) d^3\vec{r}$. It can be seen that $|++\rangle$ and $--\rangle$ are not valid fixed-points anymore since

the condition $\vec{m}(\vec{r}, t) \parallel \vec{B}_e(\vec{r}, t)$ does not hold. However, under states $|+-\rangle$ and $| - + \rangle$, the two spins are anti-parallel to each other resulting in $\int_V \vec{m}_+(\vec{r}, t) d^3\vec{r} = 0$, thus $\vec{B}_{+,AF} = 0$, as shown in figure 2(b), eqn. (13) once again reduces to eqn. (14). Therefore, both $|+-\rangle$ and $| - + \rangle$ are valid fixed points. One is a stable fixed-point and the other one is an unstable fixed-point. When $\delta\omega_i > 0$, $|+-\rangle$ is the stable fixed-point.

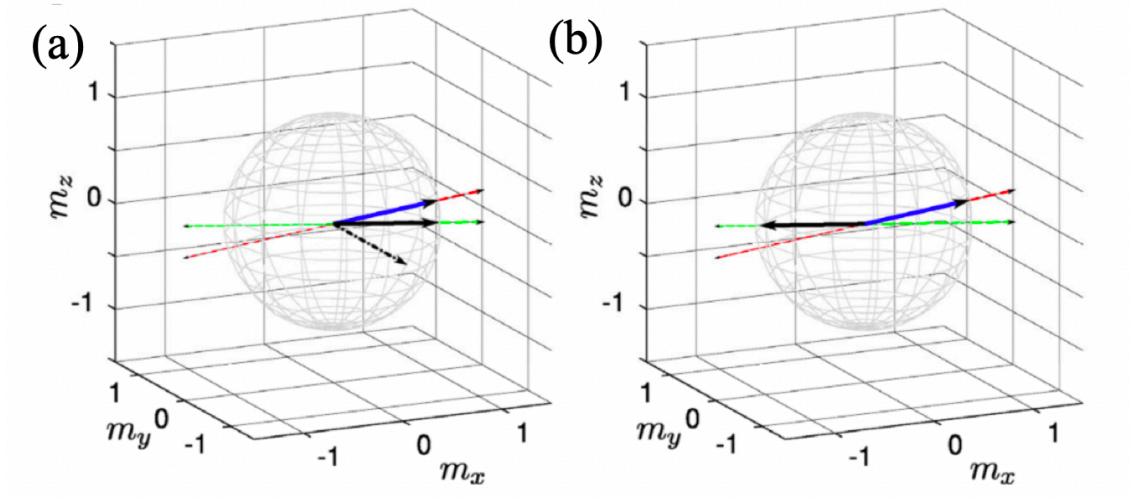


Figure 3. The graphic description of fixed-points for a strong AFF. (a) Two components in $|++\rangle$ or $|--\rangle$ states are either both parallel to their effective fields or anti-parallel to their effective fields resulting in nonzero $\int_V \vec{m}_+(\vec{r}, t) d^3\vec{r}$ and nonzero $\vec{B}_{+,AF}$. (b) Two components in $|+-\rangle$ or $| - + \rangle$ states. The two spins are anti-parallel to each other resulting in $\int_V \vec{m}_+(\vec{r}, t) d^3\vec{r} = 0$ and $\vec{B}_{+,AF} = 0$.

2.2.4 Computer Simulation

Analytical solutions for the nonlinear Bloch equation and the AFF are difficult to obtain when there is more than one spin in the system. However, computer simulation allows us to solve for the numerical solution.

Computer simulation is first carried out on a two-spin system to explain the fixed-points. Then it is performed on a 4000-spin system with superparamagnetic iron oxide (SPIO)³⁰ to examine the response of spin evolution to magnetic field variation in the presence of an AFF and CW. Last, different values of active-feedback time constant and CW strength are used to investigate the joint effect of CW and AFF.

The SPIO induced magnetic field can be characterized by:

$$B_z(d, \vartheta) = \sqrt{5/4} \frac{R^3 \Delta \omega_r}{\gamma d^3} (3 \cos^2 \vartheta - 1) \quad (15)$$

The field distribution is shown in figure 4.

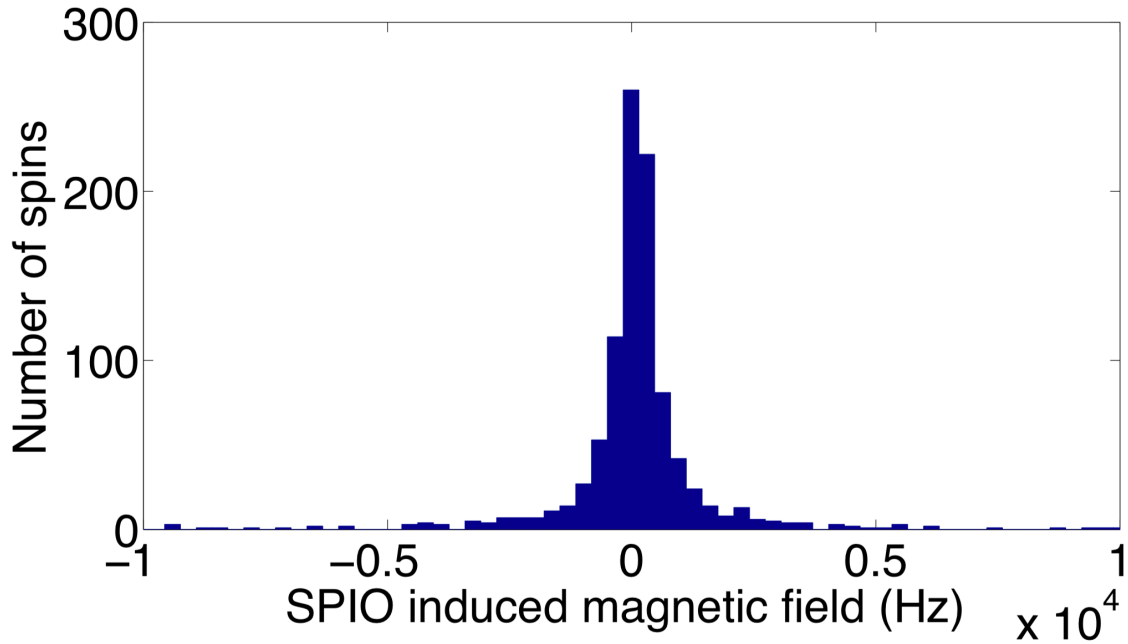


Figure 4. The SPIO-induced magnetic field distribution in Hz.

where R is the SPIO radius; $\Delta\omega_r$ is the frequency shift on the surface of the SPIO; d is the distance of the spin to the center of SPIO; ϑ is the angle between spin position and the longitudinal direction.

The flow chart of the simulation at every step is shown in figure 5. In every time step, AFF, CW and the SPIO-induced field are added to the total field in Bloch equation. Since it is very difficult to obtain analytic solutions to the nonlinear Bloch equation, we will use the rotation matrix to solve for numerical solutions.

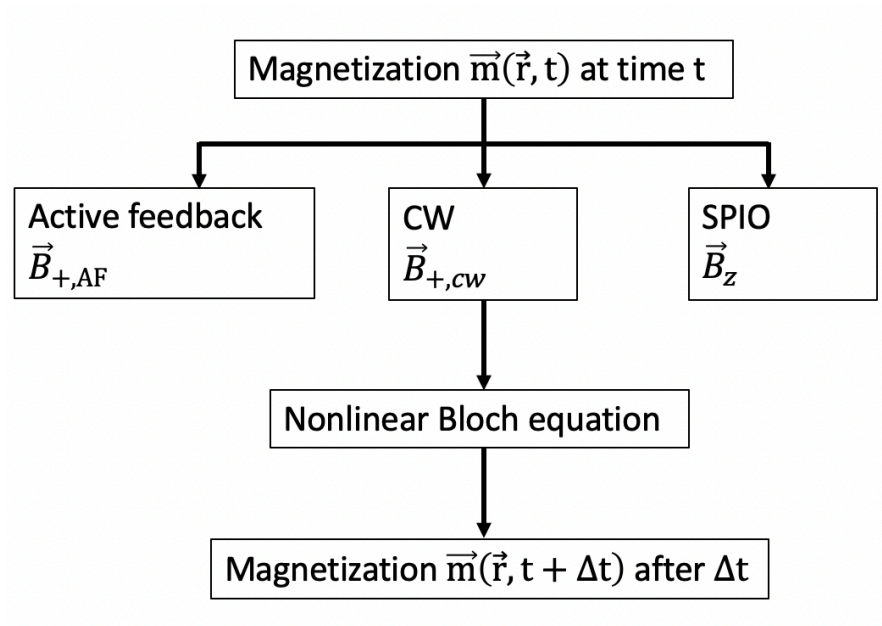


Figure 5. The simulation flow chart of the simulation in every step.

2.3 Results and Discussion

2.3.1 Simulation of Two-Spin Components

As described earlier, to reduce the complexity, the contributions of the two components are assumed to be equal. Following the simulation flow chart shown in figure 5, the evolution of the two components is shown in figure 6, 7, and 8.

Figure 6 shows the spin evolution and fixed points with a relatively large AFF (small active-feedback time constant $\tau_{AF} = 3.5ms$). Active-feedback phase $\varphi = 180^\circ$, the frequency offset of the two components $\Delta\omega = 10Hz$, CW is placed in the middle so that $\delta\omega_i = -\delta\omega_j = -5Hz$, CW frequency $\omega_1 = 45Hz$. It is clearly seen that under a relatively strong AFF, two components move in opposite directions from the same starting point and eventually reach their fixed points and the spin evolution stops.

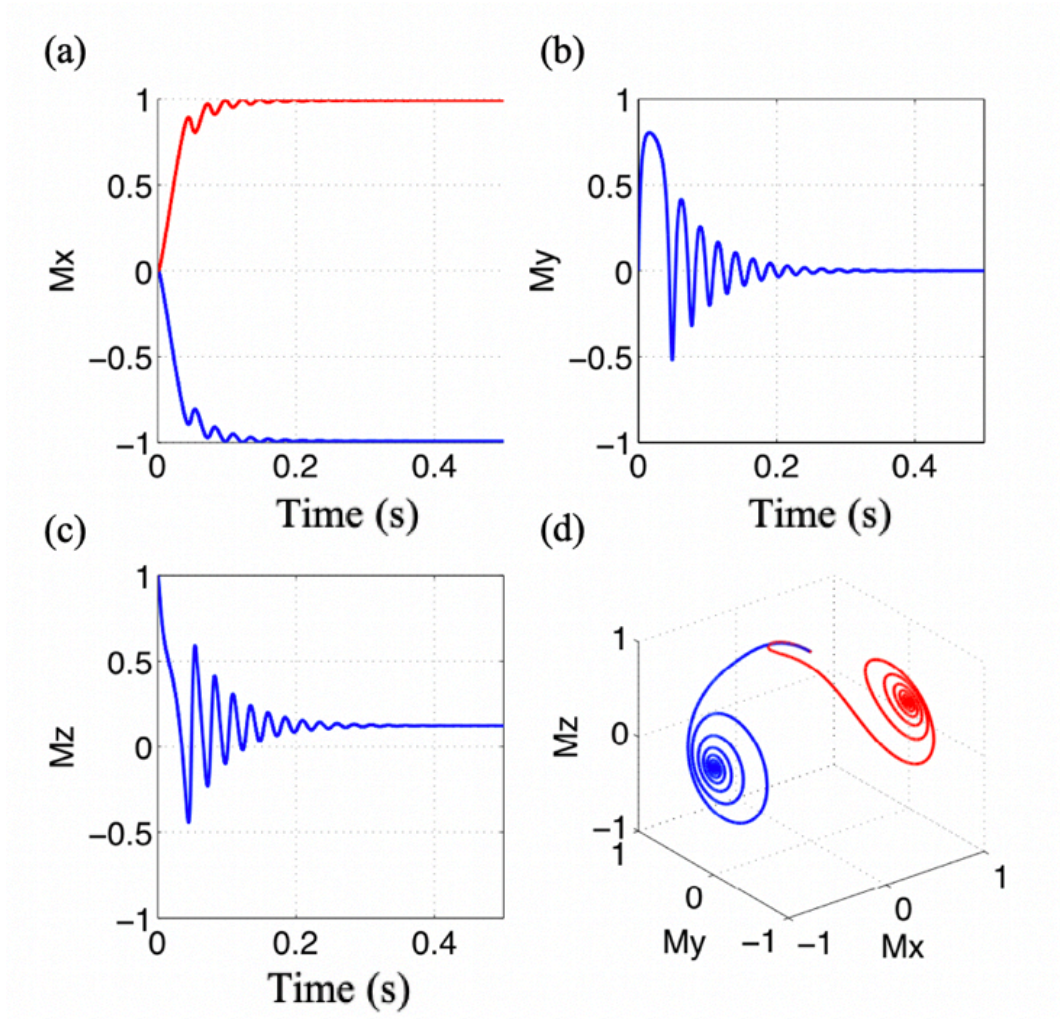


Figure 6. Two-component spin evolution and fixed points with strong AFF. $\tau_r = 3.5ms$, $\varphi = 180^\circ$, $\Delta\omega = 10Hz$, CW is placed in the middle and $\delta\omega_i = -\delta\omega_j = -5Hz$, $\omega_1 = 45Hz$. (a) Spin

evolution along the x component. Two spins are driven in different directions from the same point. (b) Plot of y component of the magnetization. (c) Plot of z component of the magnetization. Two spins have the same moving trajectory in y and z component. (d) The evolution on the Bloch sphere. Two spins move toward different directions and reach the fixed points.

Figure 7 shows the spin evolution and fixed points with a relatively weak AFF (active-feedback time constant $\tau_{AF} = 12ms$). Active-feedback phase $\varphi = 180^\circ$, the frequency offset of the two components $\Delta\omega = 10Hz$, CW is placed in the middle so that $\delta\omega_i = -\delta\omega_j = -5Hz$, CW frequency $\omega_1 = 45Hz$. It can be seen that under a slightly weaker AFF, two components still move apart to different directions but it takes a longer time and more oscillations to reach their fixed points.

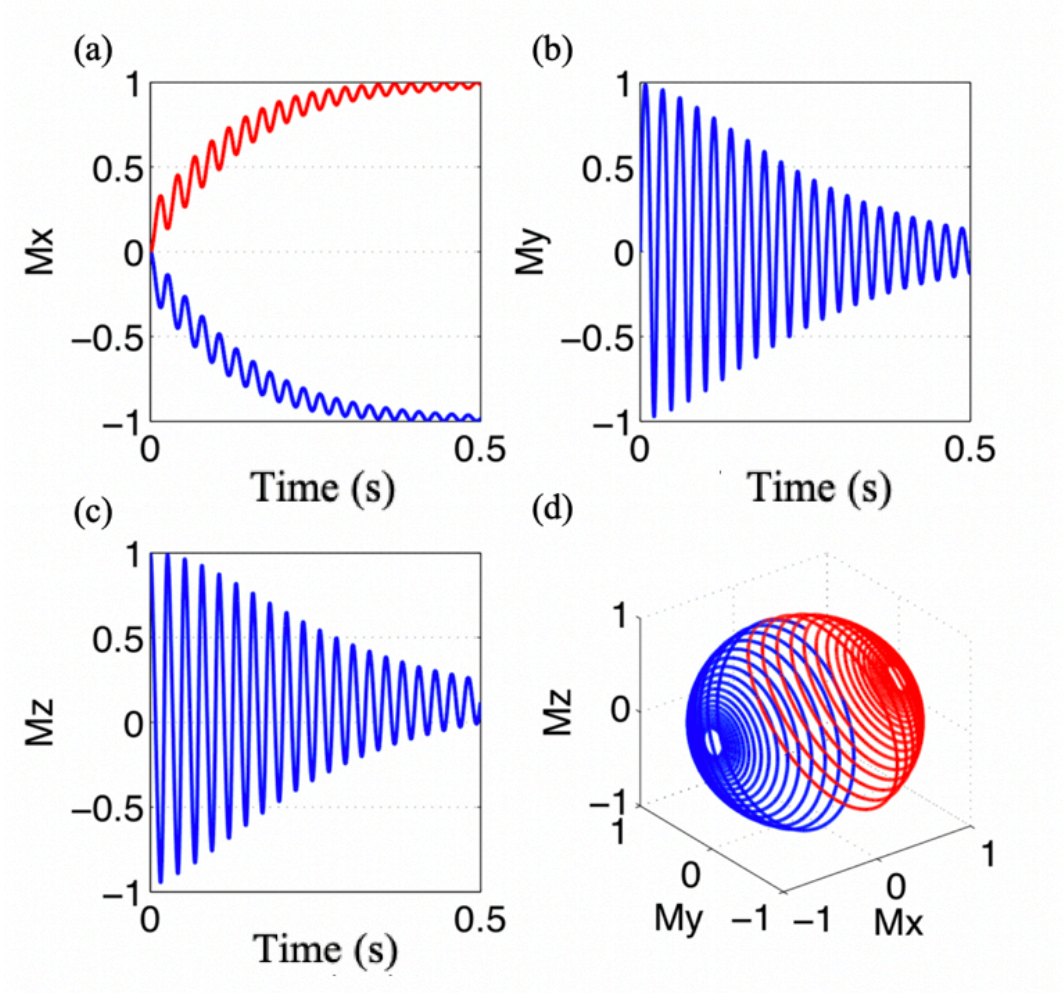


Figure 7. Two-component spin evolution and fixed points with weaker AFF. $\tau_r = 12ms$, $\varphi = 180^\circ$, $\Delta\omega = 10Hz$, CW is placed in the middle and $\delta\omega_i = -\delta\omega_j = -5Hz$, $\omega_1 = 45Hz$. (a) Spin evolution along the x component. Two spins are driven in different directions but it takes a longer time to reach ± 1 . (b) Plot of y component of the magnetization. (c) Plot of z component of the magnetization. (d) The evolution on the Bloch sphere. Two spins move in different directions and reach the fixed points. It takes more circles for spins to reach the fixed points

As shown by figures 6 and 7, with a relatively strong AFF ($\omega_1\tau_{AF} \sim 1$), there is one fixed point for each spin component, exactly as we predicted earlier.

Figure 8 shows the spin evolution and fixed points with a very weak AFF (active-feedback time constant $\tau_{AF} \rightarrow \infty$) with other conditions remain the same. In this case, the AFF disappears leaving CW the only factor to influence spin evolution. Without AFF, two components keep oscillating but never reach the fixed points, which matches the theory previously described.

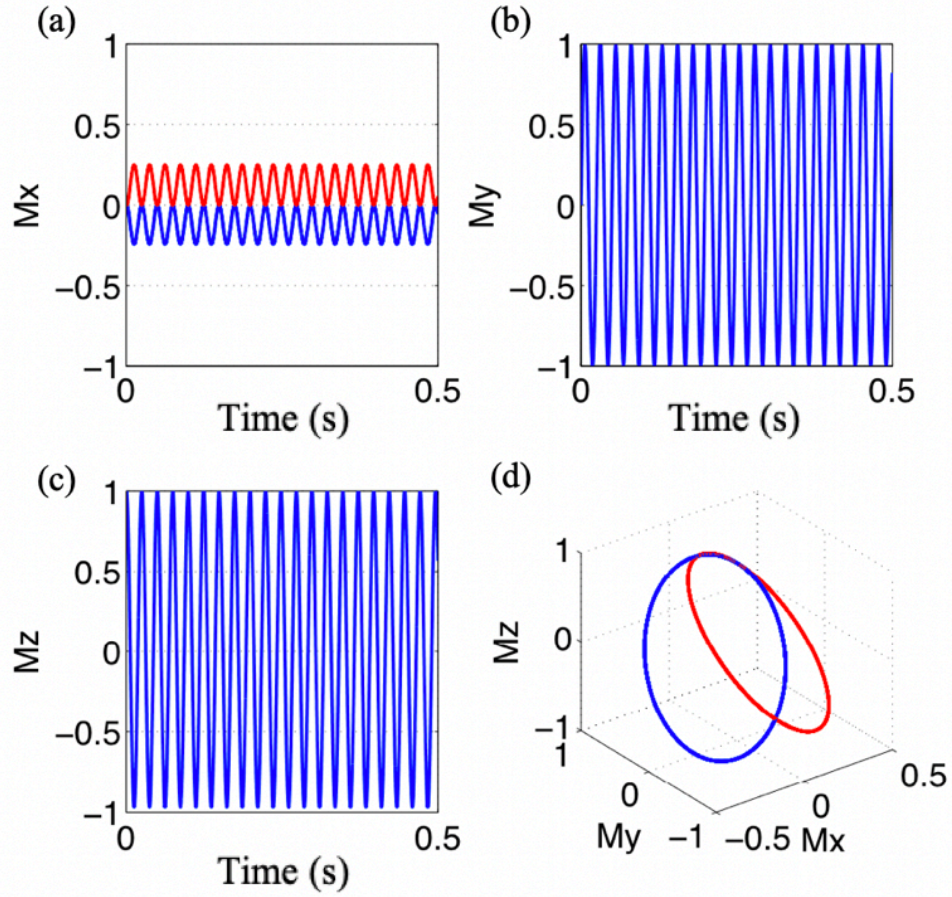


Figure 8. Two-component spin evolution and fixed points in absence of AFF. $\tau_{AF} \rightarrow \infty$, $\varphi = 180^\circ$, $\Delta\omega = 10\text{Hz}$, CW is placed in the middle and $\delta\omega_i = -\delta\omega_j = -5\text{Hz}$, $\omega_1 = 45\text{Hz}$. (a) Spin evolution along the x component. (b) Plot of y component of the magnetization. (c) Plot of z component of the magnetization. (d) Evolution on the Bloch sphere. Two spins keep oscillating and do not separate from each other anymore.

The effect of active-feedback on spin evolution can also be understood by an unbalanced Rabi cycle. CW excited spin to +z with a rate $\frac{d\alpha}{dt} = -\omega_1$ and to -z with a rate $\frac{d\alpha}{dt} = \omega_1$, where α is the phase of the spin with respect to the transverse plane. Therefore, in the absence of AFF, spin is excited to +z and -z using the same amount of time $t = (2\omega_1)^{-1}$. However, the AFF always excites the spin to the +z with a rate $\frac{d\alpha}{dt} = \frac{-\sin\alpha}{\tau_{AF}}$. It can be viewed as an interference with CW. When the spin is excited to -z, the effect of the AFF destructively interferes with CW, leaving the time required to reach -z greater than $(2\omega_1)^{-1}$. While the spin is excited to +z, the AFF constructively interferes with CW, which makes the time required to reach +z smaller than $(2\omega_1)^{-1}$. The joint effect of the AFF and CW results in $t_{-z} > t_{+z}$ and an unbalanced Rabi cycle. t_{-z} denotes the time needed to reach -z and t_{+z} denotes the time needed to reach +z.

The balanced and unbalanced Rabi cycle is shown in figure 9(a). The dashed line represents the balanced Rabi cycle with CW in absence of active field ($\tau_{AF} \rightarrow \infty$), $\omega_1 = 50\text{Hz}$, $t_{-z} = t_{+z} = 10\text{ms}$. The balanced Rabi cycle has the form of a sinusoidal function. When the AFF is relatively strong, the Rabi cycle becomes unbalanced, as shown by the solid line with $\tau_{AF} = 3.5\text{ms}$, $\omega_1 = 50\text{Hz}$, $t_{-z} = 41\text{ms}$, $t_{+z} = 6\text{ms}$.

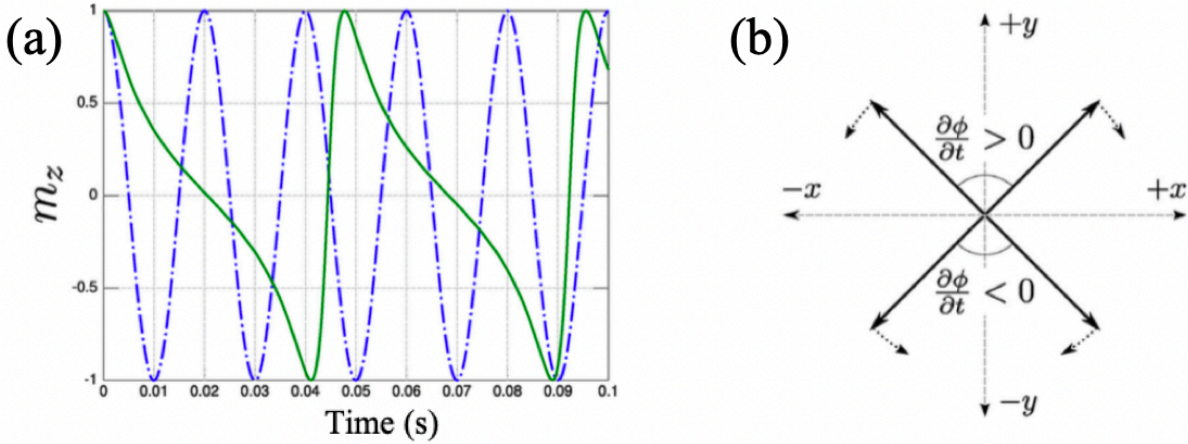


Figure 9. Graphic description of a Rabi cycle and phase accumulation. (a) The numerical solution for a balanced Rabi cycle (dashed line) with CW $\omega_1 = 50\text{Hz}$ and active field $\tau_{\text{AF}} \rightarrow \infty$, resulting $t_{-z} = t_{+z} = 10\text{ms}$; unbalanced Rabi cycle (solid line) with CW $\omega_1 = 50\text{Hz}$ and active field $\tau_{\text{AF}} = 3.5\text{ms}$, resulting $t_{-z} = 41\text{ms}$, $t_{+z} = 6\text{ms}$. (b) The phase accumulation in the two components system. When the spins are in the +y region, they begin to dephase and move away with a positive phase accumulation. When the spins are in -y region, they move closer to each other and refocus, resulting in a negative phase accumulation.

It is this unbalanced Rabi cycle that allows spins to reach their fixed points. The separation of the two components can also be explained by the phase accumulation between them. As shown in figure 9(b), when the two components are in the +y region, they begin to dephase and move away from each other while when they are in the -y region, they begin to refocus and move closer. Without an AFF, the same amount of time to +z / -z and the balanced Rabi cycle guarantees that the net phase after one cycle is zero. However, with a strong AFF, the time required to reach -z is greater than the time needed to reach +z ($t_{-z} > t_{+z}$), thus, there will be a net phase accumulation after each Rabi cycle. This accumulation will continue until spins reach their fixed points.

The amount of phase accumulated in one Rabi cycle is determined by the AFF strength, i.e. the inverse of active-feedback time constant. With a smaller active-feedback time constant, the Rabi cycle becomes more unbalanced, which yields a larger net phase in each cycle. And it can be seen clearly that fixed points are reached faster with more phase accumulated in one cycle. As a result, with a smaller active-feedback time constant, spins arrive at the fixed point faster with fewer oscillation as shown in figures 6, 7. And fixed points can be never reached without AFF, as shown in figure 8, since there is no net phase accumulation in a balanced Rabi cycle.

2.3.2 Simulation of 4000-Spin Components

With different radius, SPIO-induced field has different distribution. Two SPIO are used to model tissues with different relaxation properties. The radius of the two SPIO are $415\mu\text{m}$ and $400\mu\text{m}$. 4000 spins are assigned to each SPIO. Figures 10 and 11 shows the simulation results without and with an AFF and CW respectively.

The relaxation in the absence of the AFF and CW is shown in figure 10. The frequency offset of the two SPIO induced field is $\Delta\omega = 6\text{Hz}$, $\delta\omega_i = -\delta\omega_j = -3\text{Hz}$. The contrast in M_{xy} is around the level of noise and there is no contrast along M_z . Although there is an obvious contrast in M_x , it disappears within 0.05s. The 3D trajectory shows that there is no net phase accumulation and fixed points are not reached. It can also be seen that spins around each SPIO are not distinguishable.

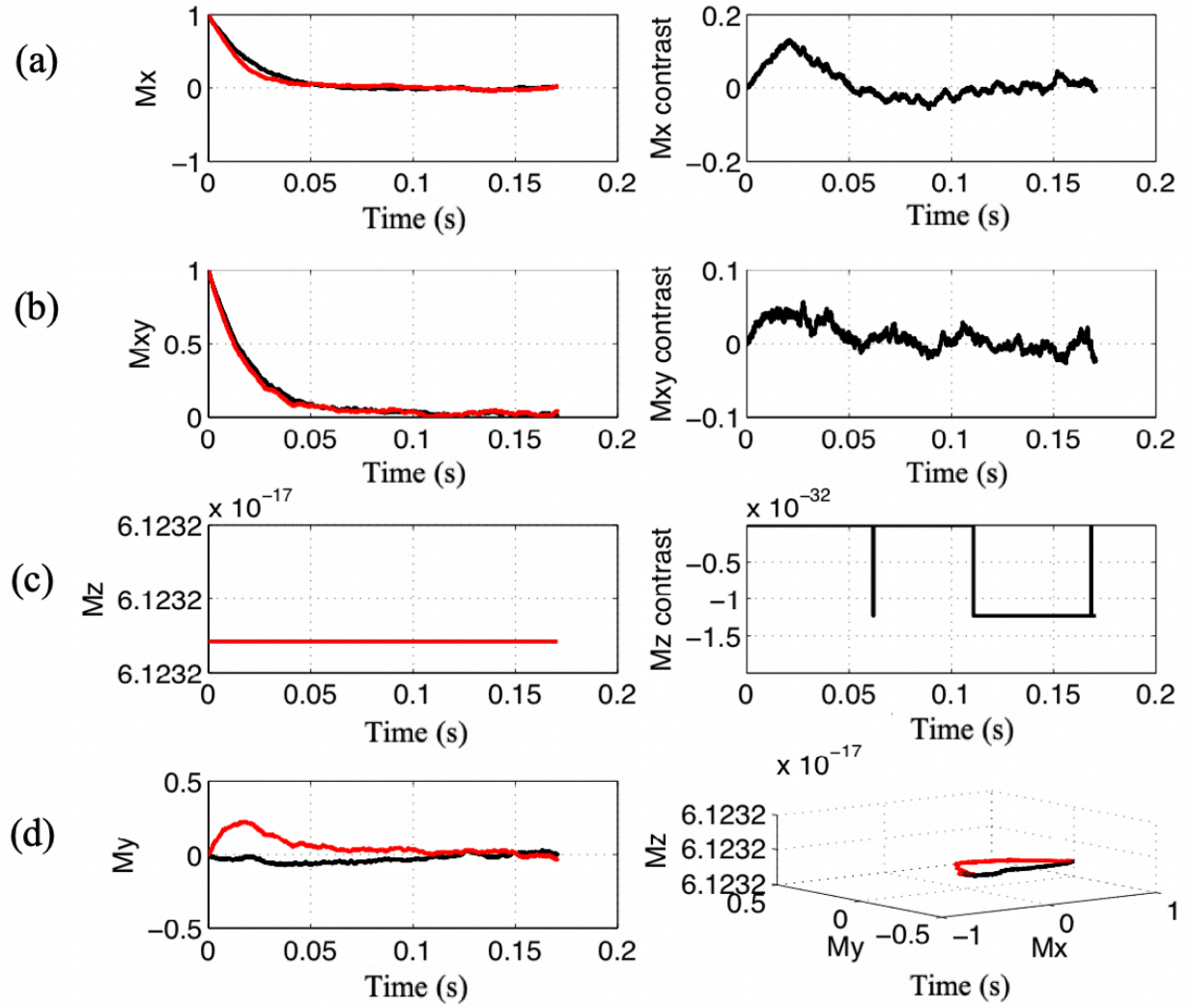


Figure 10. Relaxation of spins with SPIO-induced magnetic field without AFF and CW. (a) M_x and the contrast in M_x . A high contrast is observed but it disappears rapidly within 0.05s. (b) M_{xy} and contrast in M_{xy} . (c) M_z and contrast in M_z . (d) M_y and the 3D spin trajectory. There is no net phase accumulation and spins do not reach their fixed points.

Figure 11 shows the relaxation in presence of an AFF with $\tau_{AF} = 6ms$ and CW with $\omega_1 = 10Hz$, $\nu = -3Hz$, i.e. it is added to the center of one SPIO induced field. In this case, although there is still no obvious contrast in the x and y directions, the spins are clearly separated along the

z direction with a maximum contrast 0.25. Even with a strong oscillation, the contrast remains at a high level around 0.05. From the 3D trajectory it can be seen that the spins start from the same location gradually move toward different directions and remain still at their corresponding fixed points.

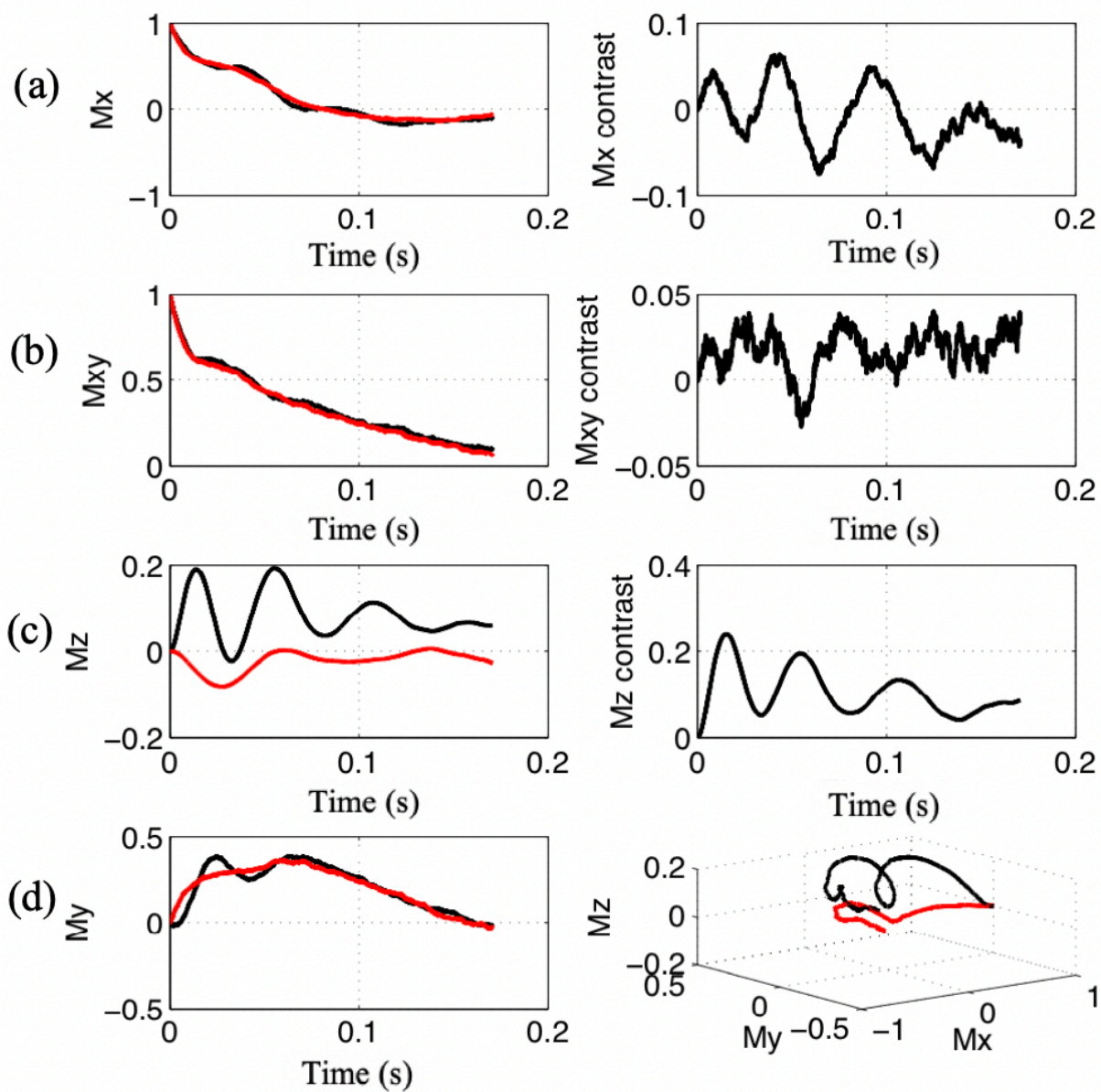


Figure 11. Relaxation of spins with SPIO-induced magnetic field in the presence of an AFF and

CW. (a) M_x and the contrast in M_x . (b) M_{xy} and contrast in M_{xy} . The contrast between the x and y components of magnetization remain at the level of the noise (c) M_z and contrast in M_z . The contrast in M_z is enhanced to 0.25 and remains at a high level around 0.05. (d) M_y and the 3D spin trajectory. Spins move in different directions and evolve to their fixed points.

2.3.3 The Effect of CW Strength

With two SPIO with a frequency off-set $\Delta\omega = 6\text{Hz}$, $\delta\omega_i = -\delta\omega_j = -3\text{Hz}$, AFF with a time constant $\tau_{AF} = 6\text{ms}$, CW with $\nu = -3\text{Hz}$. CW strength ω_1 is altered to investigate its influence on spin evolution.

With ω_1 equal to 0Hz, 20 Hz, 40 Hz, 60 Hz, simulated results are shown in figure 12. When $\omega_1 = 0\text{Hz}$, i.e. there is no CW, the spins around two SPIO arrive at the fixed-point quickly and stop evolving afterwards. As the strength is increased, the oscillation of spins is more wild and takes longer to reach the fixed point. The contrast of M_z decreases as CW strength gets larger.

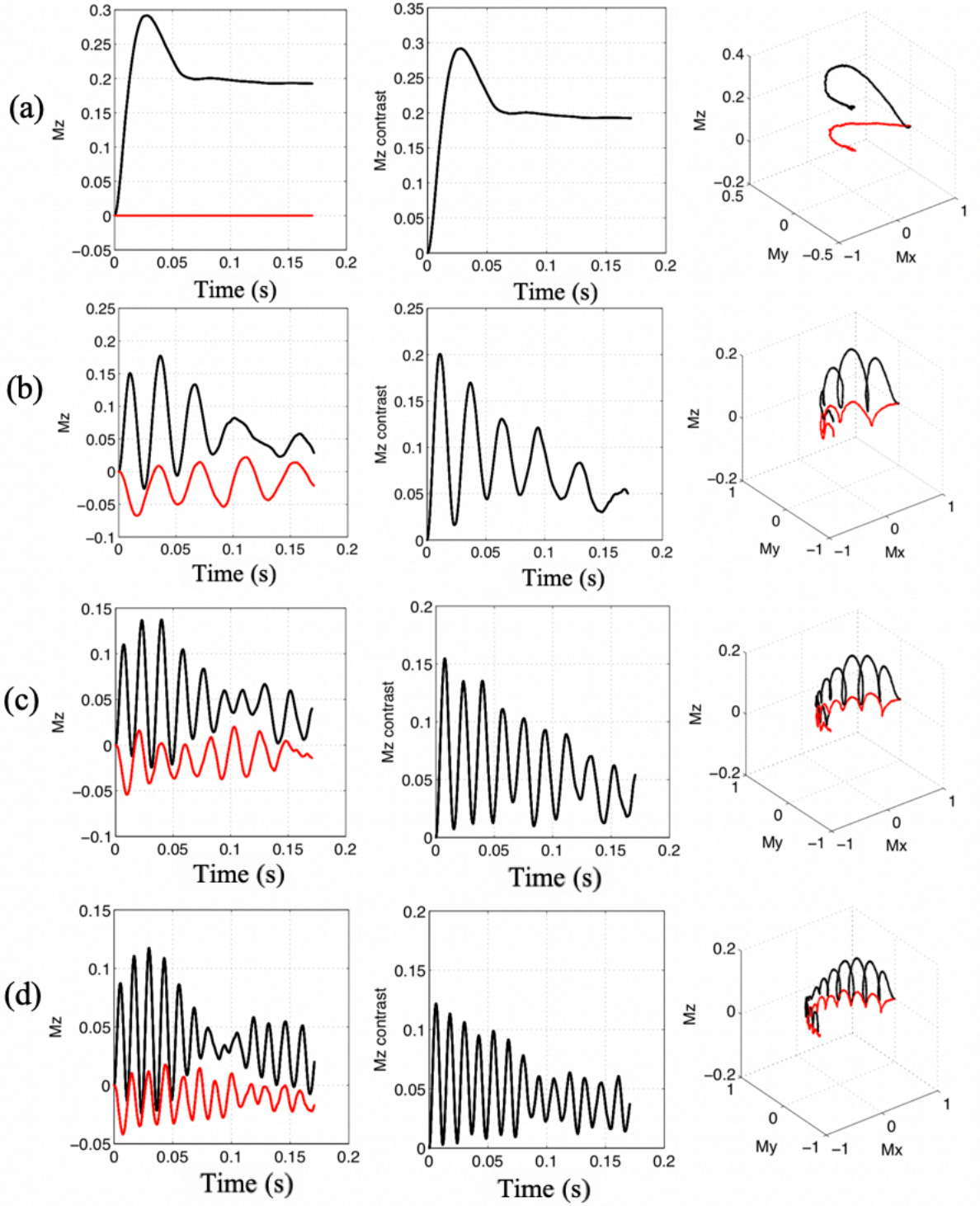


Figure 12. The simulation result with changing CW strength ω_1 . (a) $\omega_1 = 0\text{Hz}$. Spins arrive at a fixed point in one cycle. (b) $\omega_1 = 20\text{ Hz}$. Spins reach the fixed points in five cycles. (c) $\omega_1 = 40\text{ Hz}$. Spins keeps oscillating and take longer to reach fixed points. (d) $\omega_1 = 60\text{ Hz}$. It is very hard

for spins to reach fixed points.

These results matches the theory talked earlier, as CW becomes stronger, the AFF is relatively smaller resulting in a smaller net phase accumulation in each Rabi cycle. In a two-component system, CW is a necessary condition to generate fixed points, however, in the situation of more than two spins, although CW is eliminated with $\omega_1 = 0\text{Hz}$, spins can still reach the fixed point since the AFF can be treated as a static field with respect to some of the spin placed on-resonance with it and so it can take the place of the CW.

2.3.4 The Effect of Active-feedback Time Constant

With two SPIO with a frequency offset $\Delta\omega = 6\text{Hz}$, $\delta\omega_i = -\delta\omega_j = -3\text{Hz}$, CW with $\omega_1 = 5\text{Hz}$, $\nu = -3\text{Hz}$. The active-feedback time constant τ_{AF} is altered to investigate the influence of feedback field strength on spin evolution.

Simulation results for different feedback time constants are shown in figure 13 with τ_{AF} equal to 4, 6, 10 and 30ms. It can be observed that larger active-feedback time constants (i.e. a smaller AFF) drive spins to the fixed points more slowly. The oscillation of the spins becomes stronger and the contrast of M_z becomes smaller as the active-feedback time constant is larger. When the active-feedback time constant is so large that the field can be neglected, spins keep rotating and there are no fixed points anymore.

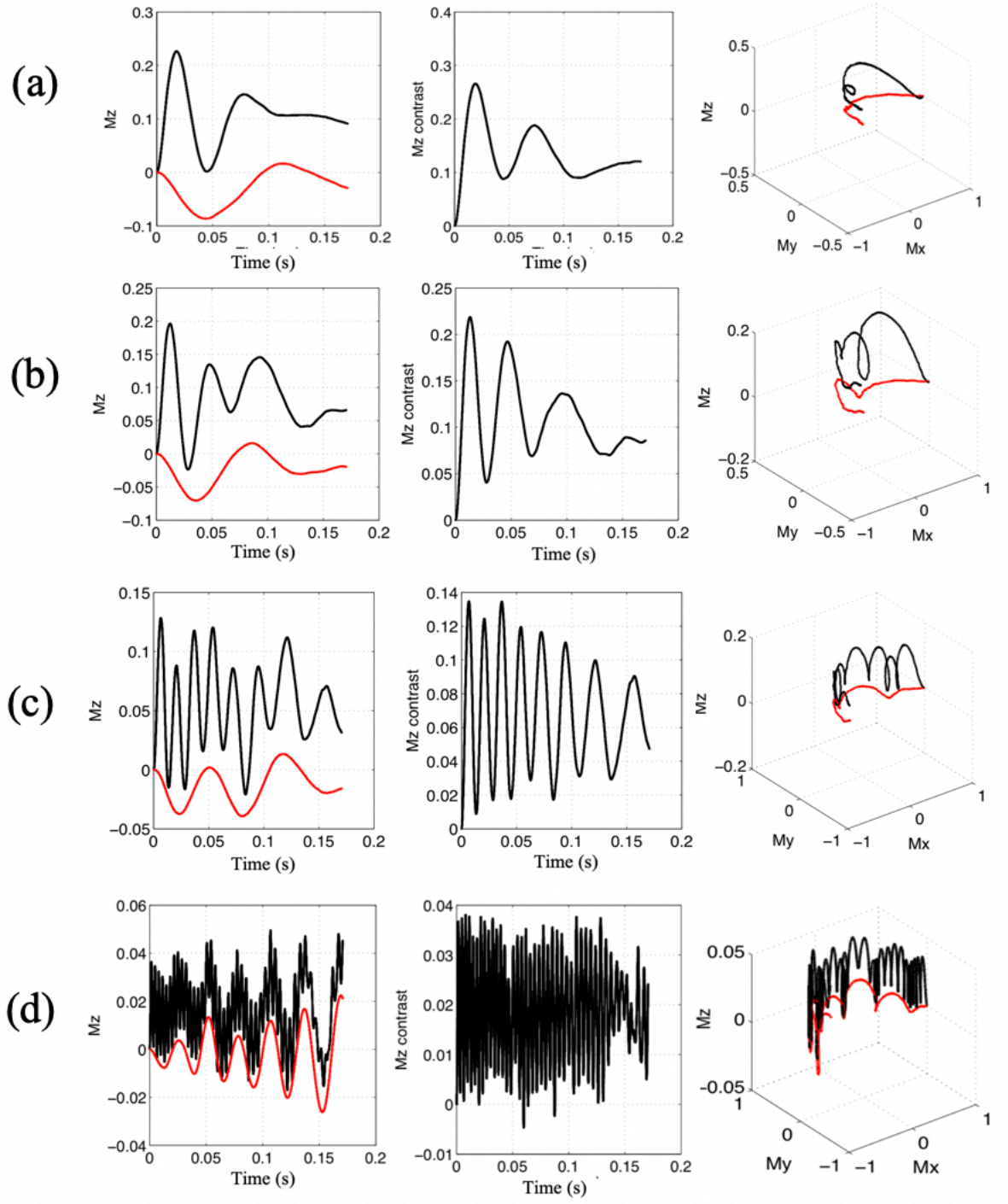


Figure 13. Simulation results for different active-feedback time constants. (a) $\tau_{AF} = 4ms$. Spins reach the fixed points in two oscillation with a small feedback time constant. (b) $\tau_{AF} = 6ms$. Spins takes more rotations and longer time to reach fixed points with a slightly higher feedback time constant. (c) $\tau_{AF} = 10ms$. With a relatively long feedback time constant, spins rotate rapidly and

do not seem to reach fixed points yet. (d) $\tau_{AF} = 30ms$. With a very long feedback time constant, AFF is nearly zero. Spins keep oscillating back and forth and there are no longer fixed points.

Just as explained earlier, as the AFF becomes weaker with a longer active-feedback time constant, it no longer effectively tilt spins to equilibrium along +z, which will make the Rabi cycle less unbalanced and less net phase will be accumulated. A large τ_{AF} such as 30ms makes it extremely hard to arrive at the fixed point for spins, thus, they keep oscillating back and forth, as shown in figure 13(d).

2.4 Conclusions

This work has a goal of demonstrating how the fixed points are generated by the joint effect of AFF and continuous-wave and the potential of using fixed point imaging to distinguish tissues with subtle differences.

This work introduced a novel MR technique call the active-feedback method, which is inspired by the natural radiation damping which causes chaotic spin dynamics and has the effect of exciting spins to the equilibrium +z position. The application of continuous-wave in the presence of AFF yields unexpected fixed points that do not align with +z or -z positions. It is shown that for a two-component system, the components move away from each other in opposite directions on the Bloch sphere in order to reach their most stable fixed points. Thus, they are separated. Such separation can be understood by an unbalanced Rabi cycle and the accumulation of net phase caused by the interference of the AFF and continuous-wave.

The motion of spins to different directions can be used to detect tissues with small relaxation differences that currently cannot be detected in experiments. Simulation results have

shown that with the AFF and continuous-wave, the contrast in the z component of the magnetization is significantly enhanced as compared with free relaxation without additional field. Important parameters such as the active-feedback time constant and continuous-wave strength are further investigated and discussed. When the AFF is relatively strong as compared to the continuous-wave, spins reach fixed point quickly. However, when the AFF is relatively small, spins have a strong oscillating motion and take longer time to reach the fixed points. In an extreme case where the AFF is nearly zero, spins no longer have fixed points.

References

- [1] E. Haacke, R. Brown, M. Thompson, R. Venkatesan, *Magnetic Resonance Imaging: Physical Principles and Sequence Design* Wiley, 1999.
- [2] Roberts, J. D. *Nuclear Magnetic Resonance: Applications to Organic Chemistry*. McGraw-Hill Book Company 1959
- [3] Logothetis, N. K., Pauls, J., Auguth, M., Trinath, T., Oeltermann, A. A neurophysiological investigation of the basis of the BOLD signal in fMRI. *Nature* 2001, 412 (6843), 150–157
- [4] Jeener, J. Dynamical instabilities in liquid nuclear magnetic resonance experiments with large nuclear magnetization, with and without pulsed field gradients *J. Chem. Phys.* 2002, 116, 8439.
- [5] Lin, Y. Y., Lisitza, N., Ahn, S., Warren, W. S. Resurrection of crushed magnetization and chaotic dynamics in solution NMR spectroscopy *Science* 2000, 290, 118-121.
- [6] Bloembergen, N., Pound, R. V. Radiation Damping in Magnetic Resonance Experiments. *Phys. Rev.* 1954, 95, 8.
- [7] Jones, G. P. Spin-Lattice Relaxation in the Rotating Frame: Weak-Collision Case *Phys. Rev.* 1966, 148, 332.
- [8] Ernst, R. R., Bodenhausen, G., Wokaun, A. *Principles of Nuclear Magnetic Resonance in One and Two Dimensions* Clarendon Press, Oxford 1987.
- [9] Warren, W. S., Hammes, S. L., Bates, J. L., Dynamics of radiation damping in nuclear magnetic resonance *J. Chem. Phys.* 1989, 91, 5895.
- [10] Forman, P. Alfred Landé and the anomalous Zeeman Effect, 1919-1921. *Historical Studies in the Physical Sciences.* 1970, 2: 153–261.
- [11] Griffiths, D. J. *Introduction to Quantum Mechanics* (2nd ed.). Prentice Hall 2004.

- [12] Cohen-Tannoudji, C., Diu, B., Laloe, F. Quantum Mechanics, Vol. 1, Wiley VCH, 1977
- [13] Abragam, A. The Principles of Nuclear Magnetism, Ch. 2, Oxford Clarendon Press, 1961.
- [14] Jarek, R. L., Flesher, R. J., Shin, S. K. Kinetics of Internal Rotation of N, N-Dimethylacetamide: A Spin-Saturation Transfer Experiment", Journal of Chemical Education 1997, 74, 978.
- [15] Malcolm, H. L. Spin Dynamics: Basics of Nuclear Magnetic Resonance, 2nd edition John Wiley & Sons New York 2008.
- [16] Yokoo, T., Bae, W. C., Hamilton, G., Karimi, A., Borgstede, J. P., Bowen, B. C., Sirlin, C. B., Chung, C. B., Crues, J.V., Bradley, W. G., Bydder G. M. A Quantitative Approach to Sequence and Image Weighting. Journal of Computer Assisted Tomography 2010, 34(3), 317-331.
- [17] Elster, A. D. An index system for comparative parameter weighting in MR imaging. Journal of Computer Assisted Tomography 1988, 12(1), 130-134
- [18] Mugler J. P. III. Basic principles. In: Edelman R. R., Hesselink J. R., Zlatkin M. B., Crues J. V., eds. Clinical magnetic resonance imaging. 3rd ed. Philadelphia, Pa: Saunders Elsevier, 2006; 23-57.
- [19] Nitz W. R., Reimer P. Contrast mechanisms in MR imaging. European Radiology 1999, 9, 1032-1046.
- [20] Louis-Joseph, A., Abergel, D., Lallemand. J. Y. Neutralization of radiation damping by selective feedback on a 400 MHz NMR spectrometer J. Biomol. NMR 1995, 5(2), 212-216.
- [21] Broekaert, P., Jeener, J. Suppression of Radiation Damping in NMR in Liquids by Active Electronic Feedback J. Magn. Reson. Ser. A 1995, 113(1), 60-64.
- [22] Abergel, D., LouisJoseph, A., Lallemand, J. Y. Amplification of radiation damping in a

- 600-MHz NMR spectrometer: application to the study of water-protein interactions. *J Biomol NMR* 1996, 8, 15–22.
- [23] Huang, S. Y., Chung, A. P., Lin, Y. Y. Visualizing Feedback-Enhanced Contrast in Magnetic Resonance Imaging. *Concepts Magn. Reson.* 2007, 36A(6), 378-393.
- [24] Datta, S., Huang, S. Y., Lin, Y.-Y. Understanding Spin Turbulence in Solution Magnetic Resonance Through Phase Space Dynamics and Instability. *Concepts Magn. Reson.* 2006, 28A(6), 410-421.
- [25] Huang, S. Y., Anklin, C., Walls, J. D., Lin, Y. Y. Sizable concentration-dependent frequency shifts in solution NMR using sensitive probes. *Journal of the American Chemical Society* 2004, 126(49), 15936-15937.
- [26] Abergel D, Delsuc, M. A., Lallemand J. Y. Comment on: Is multiple quantum nuclear magnetic resonance spectroscopy of liquid water real? *J. Chem. Phys.* 1002, 96(2), 1657-1658.
- [27] Abergel, D. Chaotic solutions of the feedback driven Bloch equations. *Phys. Lett. A* 2002, 302(1), 17-22.
- [28] Vlassenbroek, A., Jeener, J., Broekaert, P. Radiation damping in high resolution liquid NMR: A simulation study *J. Chem. Phys.* 1995, 103, 5886.
- [29] Louis-Joseph, A., Abergel, D., Lallemand, J. Y., Neutralization of radiation damping by selective feedback on a 400 MHz NMR spectrometer. *J. Biomol. NMR.* 1995, 5(2), 212-216
- [30] Yuri Matsumoto, Alan Jasanoff T2 relaxation induced by clusters of superparamagnetic nanoparticles: Monte Carlo simulations *Magnetic Resonance Imaging* 2008, 26(7), 994-998.

Chapter 3

Contrast Enhancement by Selective Self-Excitation in Active-Feedback Magnetic Resonance: Insights from Monte Carlo Simulations

3.0 Abstract

MR Contrast enhancement has been a major task in MRI study. Successful enhancement in contrast can benefit areas such as early tumor detection, study of various pathologies and study of brain structures. For this purpose, a novel active-feedback pulse sequence that sensitively detects local-magnetic-field gradient variations is introduced here. Variations in the precession frequency of the water ^1H magnetization are created due to different local magnetic fields. The behavior of the water ^1H magnetization with frequency can be manipulated by a process called “selective self-excitation” which only appears in the presence of an active-feedback field. This process is essential to contrast enhancement. Simulation results suggest that the active-feedback MR can enhance contrast significantly when there is a subtle difference in inherent tissue properties. In comparison to T_2 -weighted imaging, the active-feedback method improved signal contrast by 2.0 times with a 3% difference in blood-oxygen saturation, 3.5 times with a 4% difference in blood-vessel radius, 3.4 times with a 5% difference in diffusion coefficient and 7.6 times with a 7% difference in blood volume fraction. When it is compared with T_2^* -imaging, active-feedback imaging improved contrast by 1.7 times with a 3% difference in blood-oxygen saturation, 1.3 times with a 4% difference in blood-vessel radius, 1.8 times with a 7% difference in blood volume fraction, and 2.0 times with a 5% difference in diffusion coefficient. The theory

of selective self-excitation under active-feedback field is shown and its sensitivity to the local-magnetic-field inhomogeneity is confirmed by Monte Carlo simulation.

3.1 Introduction

The topic of contrast enhancement has been studied for over ten years because of its importance in the study of pathologies, brain structures, tumor detection, tumor characterization and so on. Besides traditional magnetic resonance imaging methodology such as T_1 -, T_2 - and T_2^* -weighted imaging, the use of a contrast agent has been popular method to improve medicine imaging contrast. For example, Gadolinium-based contrast agents have been largely used in enhancing imaging contrast¹. They enhance imaging contrast and enhance diagnosis by altering the intrinsic properties of tissue. However, the application of contrast agents is limiting. A well-known instance is brain related imaging such as brain activity imaging and brain tumor detection since the existence of brain-blood-barrier prevents blood-driven products such as contrast agents from entering the brain². As a result, it is very important to develop a contrast enhancement mechanism that depends only on inherent tissue properties and is free from the use of external contrast agent.

The major determinants of imaging signal are susceptibility and proton motion. In the human body, the concentration of deoxyhemoglobin (deoxy-Hb) and the blood-oxygen saturation directly affect the susceptibility gradient; the diffusion properties have a strong effect on proton motion; blood-vessel structure indirectly affects both susceptibility and proton motion. Susceptibility variation can be induced by the presence of deoxy-Hb, the form of hemoglobin lacking oxygen. Studies have shown that deoxy-Hb is strongly paramagnetic and the presence of this molecule in blood vessels induces irreversible magnetic field inhomogeneity,

which influences the signal in MR imaging³. Blood-oxygen saturation is directly related to the degree of deoxy-Hb in the relation that the higher level of blood-oxygen saturation indicates a lower level of deoxy-Hb thereby it affecting the spin relaxation and imaging contrast^{4,5}. Different tissues have different characteristic diffusion properties due to differences in intrinsic tissue structure and transport processes. Such differences affect the spin motion and field gradient experienced by spin, and thus influences MR signal and relaxation⁶. Blood vessel structures such as radius and blood volume fraction influence MR signal and contrast because they introduce field distortion due to blood-flow direction and the amount of blood flow through⁷.

Relaxation-based contrast mechanisms such as T_1 -, T_2 - and T_2^* - methods are very powerful and the most commonly used MRI techniques in medical imaging. However, without contrast agents, these methods are very limiting when it comes to the detection of differences between tissues with tiny differences. To solve this problem, a new approach called “active-feedback MR” that is very sensitive to tissue intrinsic properties is established.

In this work, an active-feedback field (AFF) is introduced to enhance the signal contrast of tissues with little difference in inherent properties. The theory of this approach is based on the nonlinear and chaotic spin dynamics and was first introduced in 2004⁸⁻¹⁰.

The AFF is added to the spin system through an external active-feedback device. This active-feedback device has the ability to pick up the magnetization information of the system. The information is then used to create AFF which is added to the system. As a result, small changes of magnetization of the spin system are immediately fed back into the feedback circuit and influence the spin evolution. Such nonlinear spin dynamics result in a selective self-excitation process that is very sensitive to small magnetic susceptibility differences¹¹.

Monte Carlo simulation is performed on simple spin models to understand the spin evolution and the contrast enhancement process caused by the AFF. Simulation is also performed on complex multi-cylinder models to show effects of the AFF on tissues with different intrinsic properties and the contrast improvement is compared to that of other methods. Simulation results have shown that this new method is able to continue accumulating contrast until a fixed point⁸ is reached. In comparison with T₂-weighted image generated using spin echo pulse sequence, the active-feedback pulse sequence enhanced contrast by 2.0 times with a 3% difference in blood-oxygen saturation, 3.5 times with a 4% difference in blood-vessel radius, 3.4 times with a 5% difference in diffusion coefficient and 7.6 times with a 7% difference in blood volume fraction. When it is compared with the T2* WI generated by gradient echo sequence, the contrast is enhanced 1.7 times with a 3% difference in blood-oxygen saturation, 1.3 times with a 4% difference in blood-vessel radius, 1.8 times with a 7% difference in blood volume fraction, and 2.0 times with a 5% difference in diffusion coefficient.

Simulation results have shown that the nonlinear spin dynamics induced by an AFF successfully enhances the influence of the weak field perturbations and generates robust contrast from subtle differences in inherent tissue properties.

3.2 Theory and Method

3.2.1 Nonlinear Spin Dynamics

Within a rotating frame with frequency ω_0 , the evolution of a normalized magnetization is very well-characterized by the Bloch equation:

$$\frac{\partial \vec{m}(\vec{r}, t)}{\partial t} = \gamma \vec{m}(\vec{r}, t) \times \left[\frac{\delta \omega(\vec{r})}{\gamma} \hat{z} + \vec{B}_+(\vec{r}, t) \right] - \frac{m_z - 1}{T_1} \hat{z} - \frac{m_x \hat{x} + m_y \hat{y}}{T_2} + D \nabla^2 \vec{m}(\vec{r}, t) \quad (1)$$

where γ is the gyromagnetic ratio; $\delta\omega(\vec{r}) = \omega - \omega_0$ is the resonance offset from the Larmor frequency $\omega_0 = \gamma B_0$; \vec{B}_+ is the local field in the transverse plane; T_1 and T_2 are the longitudinal and transverse relaxation times respectively; D is the self-diffusion constant; and $\vec{m}(\vec{r}, t) = \vec{M}(\vec{r}, t)/M_0$ is the normalized magnetization with respect to the equilibrium magnetization M_0 .

Typically, the local magnetic field is independent of the normalized magnetization \vec{m} , which makes the Bloch equation a linear differential equation and results in linear spin dynamics. However, when the local magnetic field is dependent on the instantaneous normalized magnetization \vec{m} , the Bloch equation becomes nonlinear because the cross-product term in Eqn. (1) is not first-order with respect to \vec{m} anymore, resulting in chaotic behavior of spins.

This dependence on the instantaneous magnetization and the resulting nonlinear spin dynamics is achieved by the AFF generated by an external active-feedback device. To make long story short, the circuit picks up information about the transverse magnetization of the system and generates a magnetic field that depends on that information. This field is then added to the spin system.

The AFF can be modeled by^{12,13}

$$\gamma \vec{B}_{+,AF}(r, t) = \frac{1}{\tau_{AF}} \langle i \vec{m}_+(\vec{r}, t) \rangle e^{i\varphi} \quad (2)$$

Both the magnitude and direction of the AFF $\vec{B}_{+,AF}$ are dependent on the average transverse magnetization vector $\vec{m}_+(\vec{r}, t)$. The AFF can be denoted by $B_{+,AF}(t) \equiv B_{AF,x} + iB_{AF,y}$ and the average transverse magnetization can be written as $m_+(t) \equiv m_x + im_y$.

Another way of understanding the mechanism of the AFF on the spin system is shown in figure 1. Adding $\vec{B}_{+,AF}$ to the system leads to chaotic dynamics^{14,15,16} as the field contains information about the spin system. Without the AFF, the spin evolution depends only on the

equilibrium condition $\vec{m}(t_0)$ and the local field $\vec{B}(t)$. When the AFF that contains information about the spin magnetization is added to the local field, it produces a chaotic spin dynamic due to self-directing, just like the avalanching effect in which the system picks up a few pieces of information each time but the information keeps accumulating, eventually leading to noticeable effects.

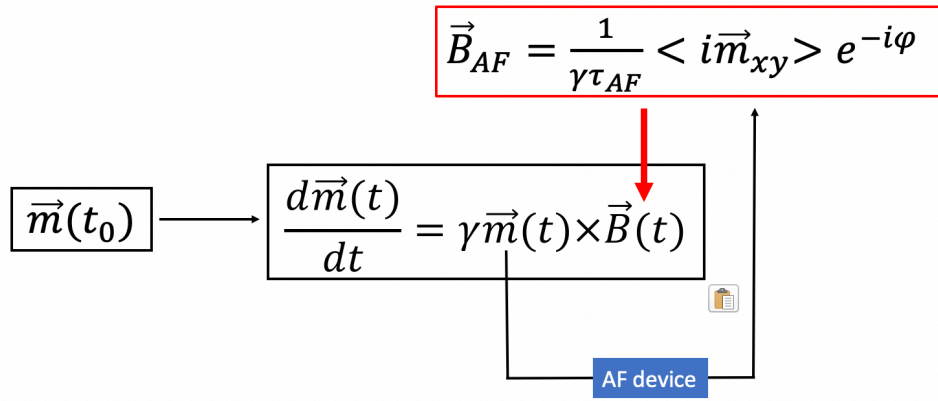


Figure 1. A graphic description of the mechanism of active-feedback phase on a spin system. Initially, the magnetization is only controlled by the local field $\vec{B}(t)$ and equilibrium state $\vec{m}(t_0)$. Through a feedback device, information about the system magnetization $\vec{m}(t)$ is picked up and used to produce an extra AFF, \vec{B}_{AF} . This field is then added back to the spin system to direct the spin evolution. As a result, all the information in the system is fed back through AFF.

There are two tunable parameters that effectively control the AFF and thus control the spin evolution. One is the active-feedback time constant, denoted by τ_{AF} , another is the active-feedback phase φ .

Similar to the T_1 and T_2 time constants, the active-feedback time constant τ_{AF} is an estimate of the time scale of the spin dynamics under AFF. τ_{AF} controls the AFF magnitude. The inverse of the time constant, $1/\tau_{AF}$, characterizes the active-feedback strength. With a shorter active-feedback time constant, the AFF is stronger. With a stronger AFF, spin is driven to $+z$ or $-z$ direction faster.

The active-feedback phase, φ , is defined from 0° to 180° since for any active-feedback phase with $\varphi > 180^\circ$ the influence on spin is identical with a phase with $\varphi - 180^\circ$. This active-feedback phase determines the angle between the AFF, $\vec{B}_{+,AF}$, and the average transverse magnetization, $\langle \vec{m}_+(\vec{r}, t) \rangle$, through the term $e^{i\varphi}$ in Eqn. (2). How the phase is defined and how it controls the spin evolution is illustrated in Figure 2.

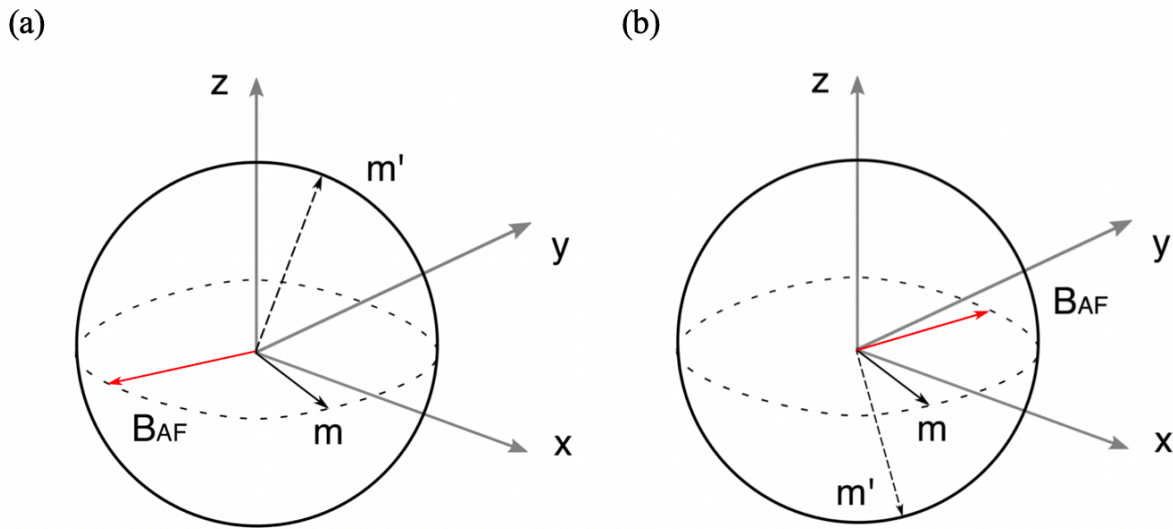


Figure 2. The graphic description of (a) positive active-feedback phase and (b) negative active-feedback phase. (a) Positive active-feedback phase with $90^\circ < \varphi \leq 180^\circ$. AFF $\vec{B}_{+,AF}$ is behind the transverse component of magnetization. In a right-handed system, the AFF that has a phase lag tilts spin up towards $+z$ direction from m to a new position m' . (b) Negative active-feedback

phase with $0^\circ \leq \varphi < 90^\circ$, $\vec{B}_{+,AF}$ is always ahead of the average transverse magnetization and such field tilts spin downwards from m to m' in a right-handed system.

Figure 2(a) shows the positive feedback phase (denoted as “+”) where $90^\circ < \varphi \leq 180^\circ$. In a right-handed system, $\vec{B}_{+,AF}$ is always behind the average transverse magnetization, $\langle \vec{m}_+(\vec{r}, t) \rangle$ and thus, it drives the magnetization towards the positive z direction (+z). Therefore, it is called the positive phase. Especially, when the feedback phase is 180° , the lag of $\vec{B}_{+,AF}$ is 90° which drives $\vec{m}_+(\vec{r}, t)$ toward the +z direction most effectively among all positive phases. As shown in Figure 2(b), $\vec{B}_{+,AF}$ is ahead of the average transverse magnetization $\langle \vec{m}_+(\vec{r}, t) \rangle$ when $0^\circ \leq \varphi < 90^\circ$. The feedback phase that produces a feedback field which is always ahead of $\langle \vec{m}_+(\vec{r}, t) \rangle$ is called the negative feedback phase (denoted as “-”). Under the right-handed system, the negative feedback phase tilts the magnetization toward the negative z direction (-z). $\vec{B}_{+,AF}$ is 90° ahead of $\langle \vec{m}_+(\vec{r}, t) \rangle$ when the active-feedback phase $\varphi = 0^\circ$ under which the AFF drives the magnetization most effectively towards -z. A special case is when $\varphi = 90^\circ$, the angle between $\vec{B}_{+,AF}$ and $\langle \vec{m}_+(\vec{r}, t) \rangle$ is 0° . When the AFF and magnetization are aligned, the magnetization hardly feels the AFF and thus, hardly moves from the original point.

3.2.2 Contrast Accumulation Mechanism by Selective Self-Excitation

One major concept in the active-feedback method is the selective self-excitation, which is the key to sensitively detect inherent tissue inhomogeneity and enhance contrast.

The principle of selective self-excitation¹⁷ is shown in figure 3. To simplify the principle, consider two types of spin with different precession frequency, shown in figure 3(a) as blue and black arrows. They are initially aligned up with the external Zeeman field at equilibrium. A 170° RF pulse tilts them to a position near -z which creates a small transverse magnetization, as shown

in figure 3(b). This small transverse magnetization generates an AFF and initiates the selective self-excitation process. In the situation that the number of blue spins is much greater than the number of black spins, the system magnetization is mainly determined by the blue spins. Consequently, the AFF depends more on the blue spins since it is dependent on the average transverse component of the magnetization. As a result, the AFF will possess a frequency much closer to the precession frequency of the blue spins. Since the frequency of the AFF matches the frequency of the blue spins, these spins are in resonance with the field and are excited. When the active-feedback phase φ is set to be positive, spins that are on resonance are tilted up to the $+z$ direction. While the blue spins are tilted up effectively, the black spins are far away from the resonance condition and are tilted up much slowly due to frequency mismatch. As the AFF is continually adding to the system, the selective self-excitation process results in a contrast along z direction, as shown in figure 3(c).

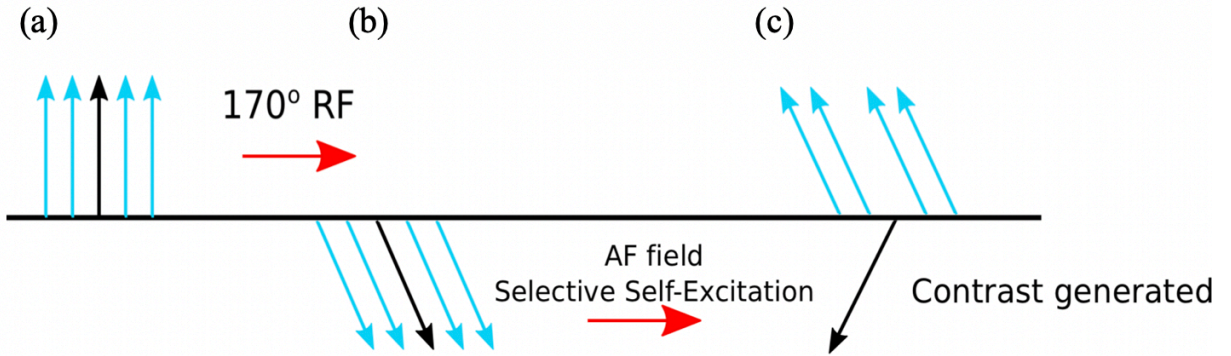


Figure 3. The graphic description of the contrast accumulation mechanism by selective self-excitation process. Two types of spin with different precession frequencies are denoted by blue arrows and the black arrows. Blue spins outnumber black spins. (a) All the spins are initially in equilibrium with the external Zeeman field along the $+z$ direction. (b) A 170° RF pulse tilts the

spins away from +z to a position close to -z and generates a small transverse magnetization. (c) An AFF is created by the small transverse magnetization. The AFF is mainly controlled by the blue spins and possesses a frequency much closer to that of the blue spins. (c) With a positive feedback phase, blue spins are excited and driven to the +z direction much more efficiently than black spins due to the resonance condition. Consequently, contrast along the z direction is generated.

3.2.3 Different Contrast Mechanism and Pulse Sequence

In this chapter, the active-feedback contrast mechanism is compared with relaxation-based contrast mechanisms such as T_2 - and T_2^* -weighted images. The T_1 -weighted image is not used since the task is to look for new techniques that are sensitive to local field variations while T_1 -relaxation is normally known as “thermal relaxation” which means that there must be a stimulation from an external source^{18,19}. Thus, a T_1 -weighted image is generally insensitive to small local environment inhomogeneities^{20,21}. T_2 -weighted image and T_2^* -weighted image are based on the transverse relaxation and are very sensitive to local inhomogeneity and difference in inherent properties^{22,23}. T_2 relaxation, also called “spin-spin relaxation”, is the real transverse relaxation due to spin dephasing. This dephasing is an irreversible dephasing process resulting from random atomic or molecular interactions^{24,25}. However, there is also a reversible spin dephasing process that is induced by local magnetic inhomogeneity. This reversible dephasing process is characterized by the T_2^* relaxation²⁶. The source of the T_2^* relaxation can be the non-uniform Zeeman field, differences in magnetic susceptibility of different tissue, chemical shift and MRI gradient encoding²⁷. The relationship between T_2 and T_2^* is characterized by the following equation:

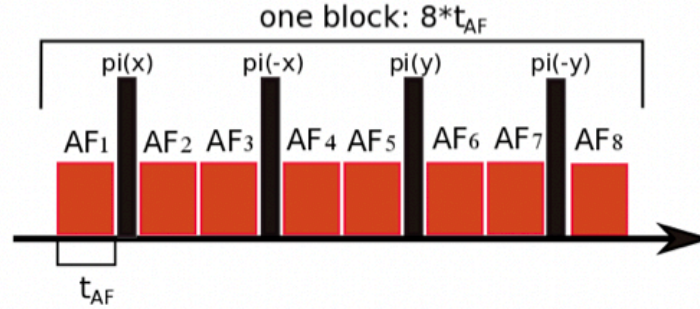
$$\frac{1}{T_2^*} = \frac{1}{T_2} + \frac{1}{T_{2i}} \quad (3)$$

where T_{2i} is the relaxation time constant that attributable to field inhomogeneity.

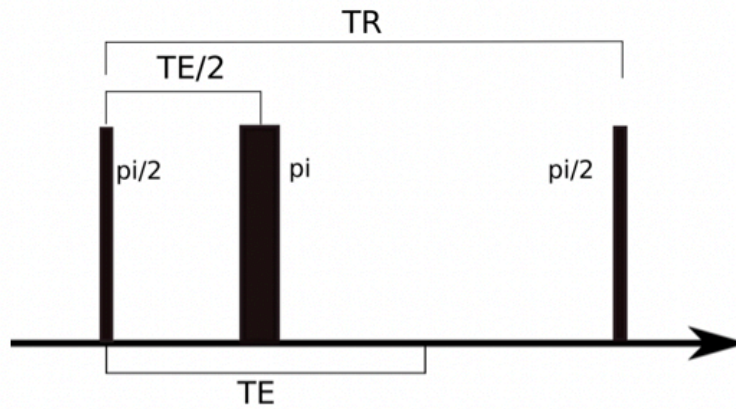
A simple graphic description of pulse sequences used for simulation is shown in figure 4. The pulse sequence for the active-feedback method is shown in figure 4(a). One block in the active-feedback sequence consists of eight sub-blocks each with feedback duration t_{FB} during which the AFF is added. Signal is collected at the end of each block at every $8t_{FB}$. The active-feedback phase is set to be positive at all times so this sequence is also called a “++++” sequence. The active-feedback time constant is tunable but fixed throughout. In this simulation, active-feedback phase is always set to 180° (+). With 180° phase, on resonance spins are driven upwards to $+z$ and eventually reach at a fixed point around $+z^{17}$. π pulses are applied between each sub-block. The π pulses have a function of moving spins away from equilibrium and creating a small AFF to reinitiate the selective self-excitation.

Figure 4(b) shows the spin echo sequence used for T_2 -weighted imaging. A $\pi/2$ pulse first tilts spins to the transverse plane and a following π pulse refocuses the spins resulting in a signal echo at echo time (TE). The π pulse is applied at half of the echo time. Another $\pi/2$ pulse and a following π pulse is applied repeatedly after TR, which is called the repetition time²⁸. Figure 4(c) shows the gradient echo sequence for T_2^* -weighted imaging, as compared to the spin echo sequence, there is no π pulse to refocus the spin dephasing process²⁹.

(a) AF ++++ sequence



(b) Spin echo sequence



(c) Gradient echo sequence

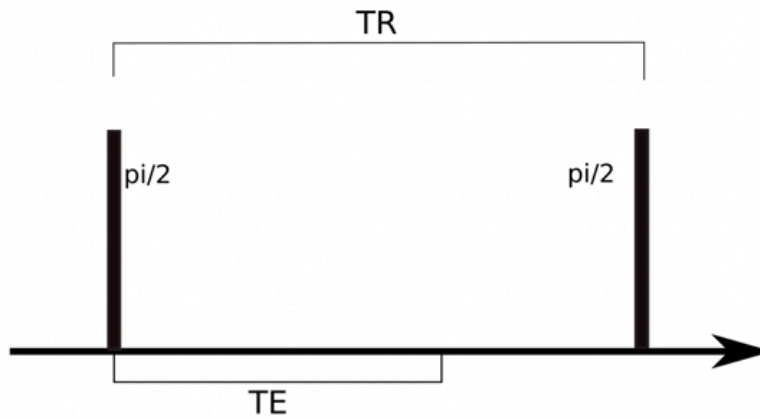


Figure 4. Graphic description of (a) active-feedback sequence, (b) spin echo sequence, (c) gradient echo sequence. (a) “++++” pulse sequence for active-feedback method. One feedback block consists of eight feedback sub-blocks and each sub-block lasts t_{FB} . π pulses are applied between

sub-blocks. The active-feedback phase is set to be 180° (+) at all times. Signal is collected at the end of each block (every $8t_{FB}$). (b) The spin echo sequence for T2-weighted imaging. A $\pi/2$ pulse first tilts spins onto the transverse plane and a following π pulse is applied at half echo time to rephase the spins. The echo signal appears at TE. (c) The gradient echo sequence for T2*-weighted imaging. A $\pi/2$ pulse is applied to flip spins to the transverse plane.

3.2.4 Monte Carlo Simulation

To test the active-feedback MR method, simulations were carried out based on a multi-cylinder model^{30–32}.

Blood vessels are modeled as straight cylinders. The deoxy-Hb-induced local magnetic field B_c , given as the component along the direction of the applied Zeeman field (B_0 , along +z direction), is expressed by^{32,33}:

Outside cylinder:

$$B_c = 2\pi\Delta\chi * Hct * (1 - Y)B_0\sin^2(\theta)\left(\frac{a}{r}\right)^2 \cos(2\phi) \quad (3a)$$

Inside cylinder:

$$B_c = 2\pi\Delta\chi * Hct * (1 - Y)B_0(3\cos^2(\theta) - 1)/3 \quad (3b)$$

where Hct is the hematocrit; $\Delta\chi$ is the susceptibility difference between the fully oxygenated and fully deoxygenated hemoglobin; θ is the angle between the applied field B_0 and the blood-vessel axis; a is the blood-vessel radius; r is the distance between a point of interest and the center of the vessel cross section in the plane normal to the vessel; ϕ is the angle between the vector r and the component of B_0 in the plane; Y is the oxygenation saturation so $(1 - Y)$ is the degree of deoxy-Hb; $B_0 = 7T$, $\Delta\chi = 0.27\text{ppm}$ and $Hct = 40\%$ ³⁴ is used.

As shown in figure 5, tissues that contain blood vessels and water protons are modeled as voxels. The center voxel that contains randomly oriented cylinders with a fixed blood volume fraction, f , is the area of interest. Since the MR signal is mainly contributed from bulk water protons that are far from the deoxy-Hb induced dipolar center, 100 voxels without blood vessels are generated to model the signal contribution from bulk water. Simulation with the number of voxels greater than 100 generates similar results. Under this model, spins that are in the center voxel experience the deoxy-Hb-induced local field while spins in the surrounding voxels are only affected by the T_2 relaxation in tissue^{35,36}. The average magnetization of all spins is calculated and later is used to generate the AFF.

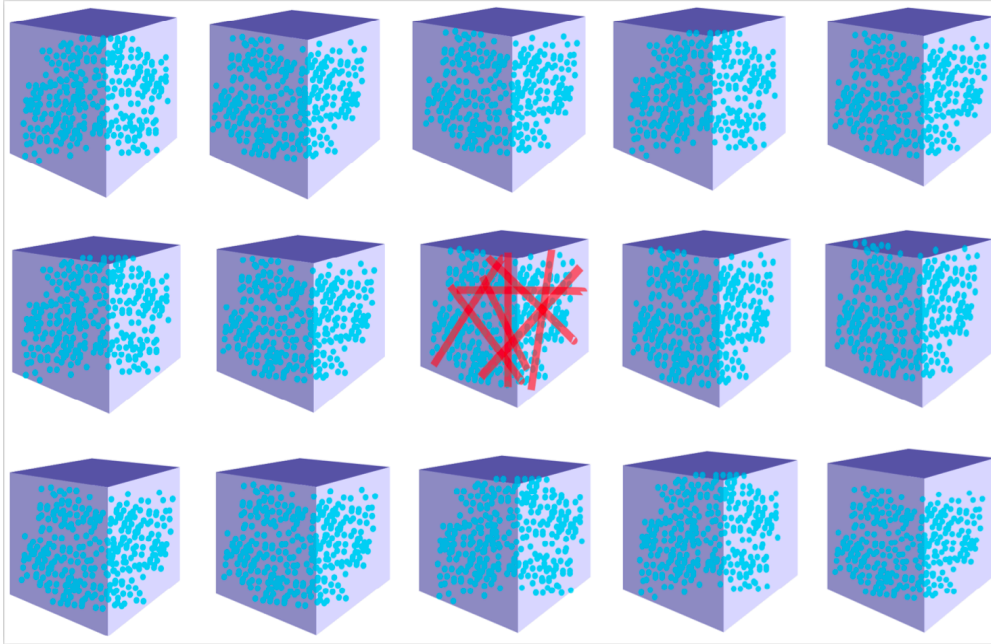


Figure 5. Simulation model of blood vessels and tissue. Blood vessels are modeled as straight cylinders. The center voxel that contains randomly oriented blood vessels is the area of interest. Surrounding voxels that do not contain blood vessels are used to model the effect from the bulk water protons that are far away from the induced dipolar center. Spins inside the center voxel

experience the deoxy-Hb-induced local magnetic field while spins in the surrounding voxels are not affected by the induced magnetic field.

8000 ^1H spins are initially distributed in each voxel using a $20 \times 20 \times 20$ grid. Every spin performs a three-dimensional random walk with diffusion coefficient D . The three-dimensional step size is $\sqrt{6D\Delta t}$ with step time $\Delta t = 0.1\text{ms}$ and the result converges with smaller step time. The size of each voxel is $30 \times 30 \times 30 \mu\text{m}^3$. This number was chosen for two reasons. First, to model the blood vessels as straight cylinders, the size of voxel should be significantly less than the typical length of an unbranched segment of brain capillary ($\sim 110 \mu\text{m}$)³⁷. Second, the size of the voxel should be long enough for diffusion with one-dimensional diffusion step $\sqrt{2DTE}$ ($TE \sim 100\text{ms}$).

To reduce the computational cost, the water permeability³⁸ was neglected, so that, protons that are initially in the blood-vessel remain inside the blood-vessel and protons initially outside the vessel will not diffuse into the blood vessel. Besides, to assure the accuracy of the average assemble magnetization, the number of spins in each voxel remains fixed. If one spin diffuses out of the voxel, another spin will diffuse into the voxel from the opposite surface.

3.2.5 Computational Parameters

Table 1 shows the parameters that are fixed during simulation, including the parameters that are based on the model assumptions such as number of protons and voxel size and the parameters that typically do not change in different tissues such as the susceptibility difference.

The intrinsic tissue properties such as oxygen saturation and blood-vessel radius are usually different in different tissues. Baseline values are defined for these parameters, as shown in table 2. The baseline values of intrinsic tissue properties are chosen from values of healthy tissue. These

values will be altered later to test the sensitivity of different imaging methods to intrinsic tissue properties.

Table 1. Experimental parameters used in the multi-cylinder model (fixed value), including parameters that are based on the model assumptions and parameters that do not change in different tissues.

Parameter	Value
Applied Zeeman field, B_0 (T)	7
Susceptibility difference, $\Delta\chi$ (ppm)	0.27
Hematocrit, Hct (%)	40
Number of voxel	101
Voxel size (μm)	30
Number of spins in each voxel	8000
step time, Δt (ms)	0.1

Table 2. Experimental parameters used in the multi-cylinder model (baseline value), including intrinsic tissue properties. The baseline values are chosen from values of healthy tissue and are used as a control group.

Parameter	Value
blood-vessel radius, a (μm)	5.3
blood volume fraction, f (%)	6.0
Oxygenation saturation, Y	0.60
diffusion coefficient, D ($10^{-10} \text{ m}^2/\text{s}$)	6.63

3.3 Results and Discussion

To gain insight into the selective self-excitation process and the contrast enhancing mechanism in the active-feedback method, the simulation was first carried out using a simple spin evolution model without cylinders. After that, simulation was performed on multi-cylinder model to compare different contrast generating mechanism in different imaging methods.

3.3.1 Frequency Selection by Selective Self-Excitation: Simple Spin Models

To better understand the contrast along the longitudinal direction generated by the selective self-excitation with AFF, simulations were carried out on a spin model.

Ninety spins with frequency at 0Hz and ten spins with frequency at 10Hz were simulated. All the spins evolve under the AFF. In calculating the system magnetization, the ninety spins that are at 0Hz contributes 90% to the average transverse magnetization, and the ten spins at 10Hz only contribute 10% to the average transverse magnetization. Recall that the AFF is controlled by the average transverse magnetization: it will possess a frequency much closer to 0 Hz since spins with 0 Hz contribute the most to the transverse magnetization. As a result, these spins meet the on resonance condition. To distinguish more easily the two spin groups, spins with frequency 0Hz are denoted as “on-resonance” and the 10Hz spins are denoted as “off-resonance”. The simulation result is shown in figure 6.

Figure 6(a) and (b) show the magnetization of the on-resonance spins (0Hz) and off-resonance spins (10Hz) respectively. The on-resonance spins are driven to the +z direction much faster than the off-resonance spin (10Hz) with a 180° active-feedback phase and an 8ms feedback time constant. On-resonance spins arrive at the +z axis around 0.05s while the off-resonance spins have longitudinal magnetization 0.5 at around 0.3s. Similar results are shown in figure 6(c): the

on-resonance spins are excited more efficiently while the off-resonance spin keeps oscillating around its effective field near +z. Consequently, a contrast along z direction is generated.

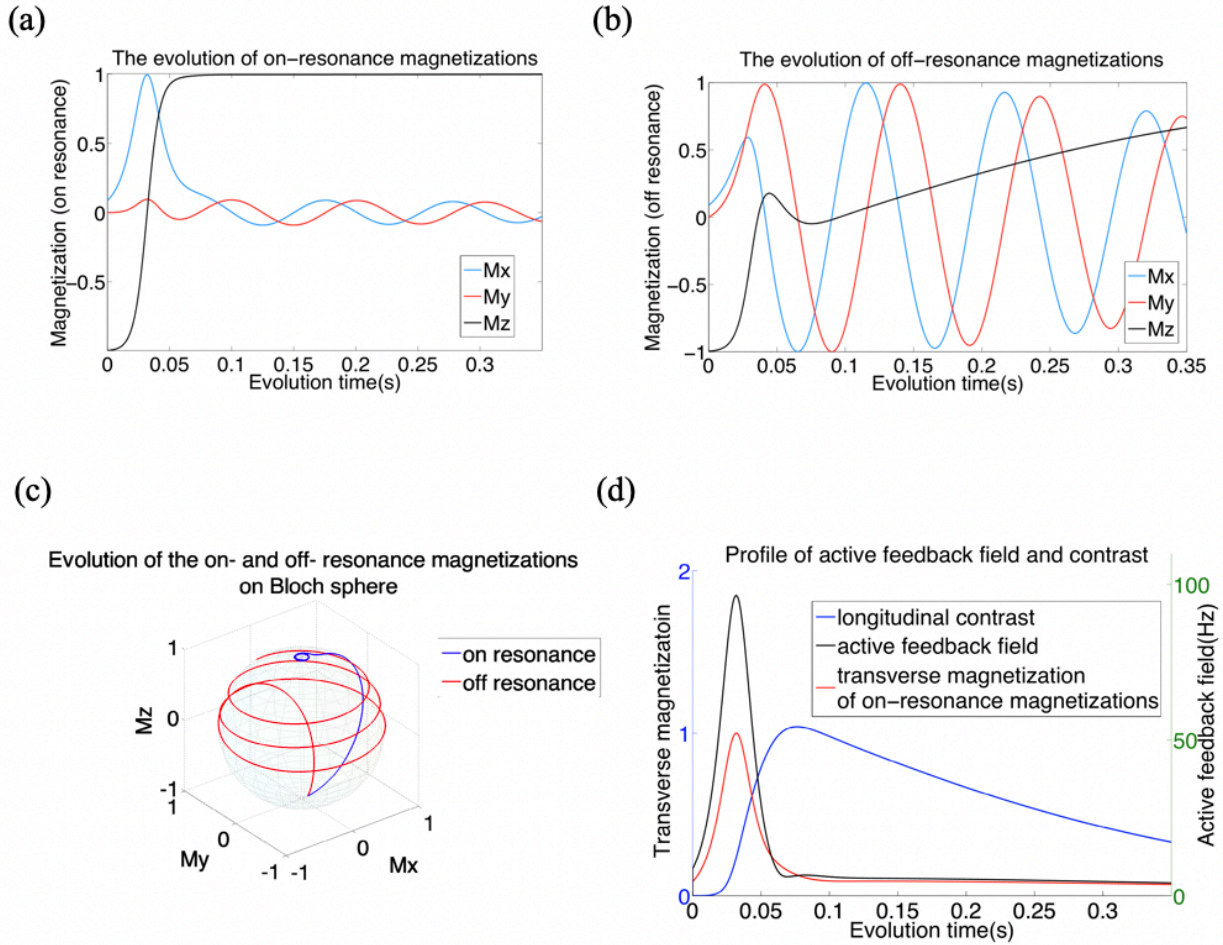


Figure 6. Selective self-excitation of spins with different frequency. 100 spins total, 90 spins at 0Hz meet the on-resonance condition and 10 spins at 10Hz are off-resonance. $\varphi = 180^\circ$. $\tau_{AF} = 8\text{ms}$. (a) The magnetization of the on-resonance spin. Spin reaches equilibrium along the z direction at around 0.5s. (b) The magnetization of off-resonance spin. Spin does not reach the z axis within the testing time (0.35s). (c) The evolution of on-resonance and off-resonance spins on the Bloch sphere. On-resonance spin is excited more efficiently and tilted to +z much faster than off-resonance spin, resulting in a contrast along the longitudinal direction. (d) Profiles of the AFF,

transverse magnetization of on-resonance spin and the longitudinal contrast. The profile of the AFF matches the transverse magnetization of no-resonance spin very well. Longitudinal contrast is generated and accumulates when active-feedback exists. Contrast reaches maximum when active-feedback reaches its minimum.

The selective self-excitation process is clearly demonstrated in figure 6(d). The AFF profile matches the transverse magnetization of on-resonance spins very well, which indicates that the spin evolution process is dominated by the on-resonance spin. More interestingly, the AFF controlled by on-resonance spin only excites the on-resonance spin and thus selects itself from the rest. Moreover, the contrast along the z direction only accumulates in the presence of AFF. The loss of transverse magnetization diminishes the AFF and hinders contrast accumulation. When the on-resonance spin reaches the fixed point on +z, the AFF and transverse magnetization reach the minimum and contrast hits the maximum.

The simulation was performed on a model with three spin groups. As shown in figure 7, the three spin groups have the same frequency width (2Hz) but different center of frequency: 0Hz, -10Hz and +10Hz, with 700 spins, 250 spins and 50 spins respectively.

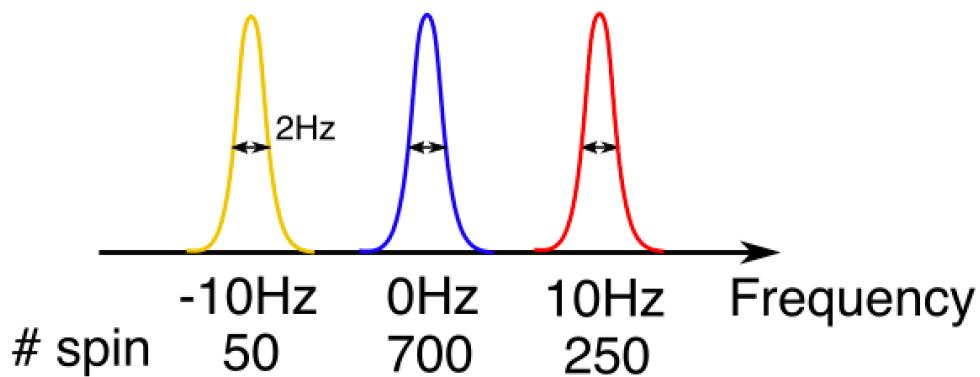


Figure 7. Selective self-excitation of three spin groups with different centers of frequency, 0, 10 and -10Hz. The frequency width is 2Hz for the three groups. The total number of spins is 1000, with 700 in the group centered at 0Hz, 250 in the group centered at 10Hz and 50 in the group centered at -10Hz.

The average transverse magnetization of the three-spin group is calculated and used to create the AFF ($\varphi = 180^\circ$, $\tau_{AF} = 8\text{ms}$). Three groups that are centered at 0, 10 and -10Hz are denoted as “on resonance”, “off resonance1” and “off resonance2”, respectively as the group centered at 0Hz contributes the most. Results are shown in figure 8. Figures 8(a) and (b) show the longitudinal magnetization. The spin group that contributes the most to the average transverse magnetization (70%, on resonance, blue line) is excited the most effectively and driven to the +z direction the fastest. The spin group that contributes the second (25%, off resonance1, red line) is tilted toward the +z direction less effectively but still faster than the one contributes the least (5%, off resonance2, yellow line). Due to the different excitation efficiency, three spin groups are successfully distinguished. As shown in figure 8(c), the AFF perfectly matches the trend of on-resonance transverse magnetization. The AFF becomes very small when the on-resonance spin reaches the fixed point and loses most of its transverse magnetization. This dependence guarantees that the off-resonance spins cannot reach the self-excitation of the on-resonance spins. Therefore, stable longitudinal contrast is promised.

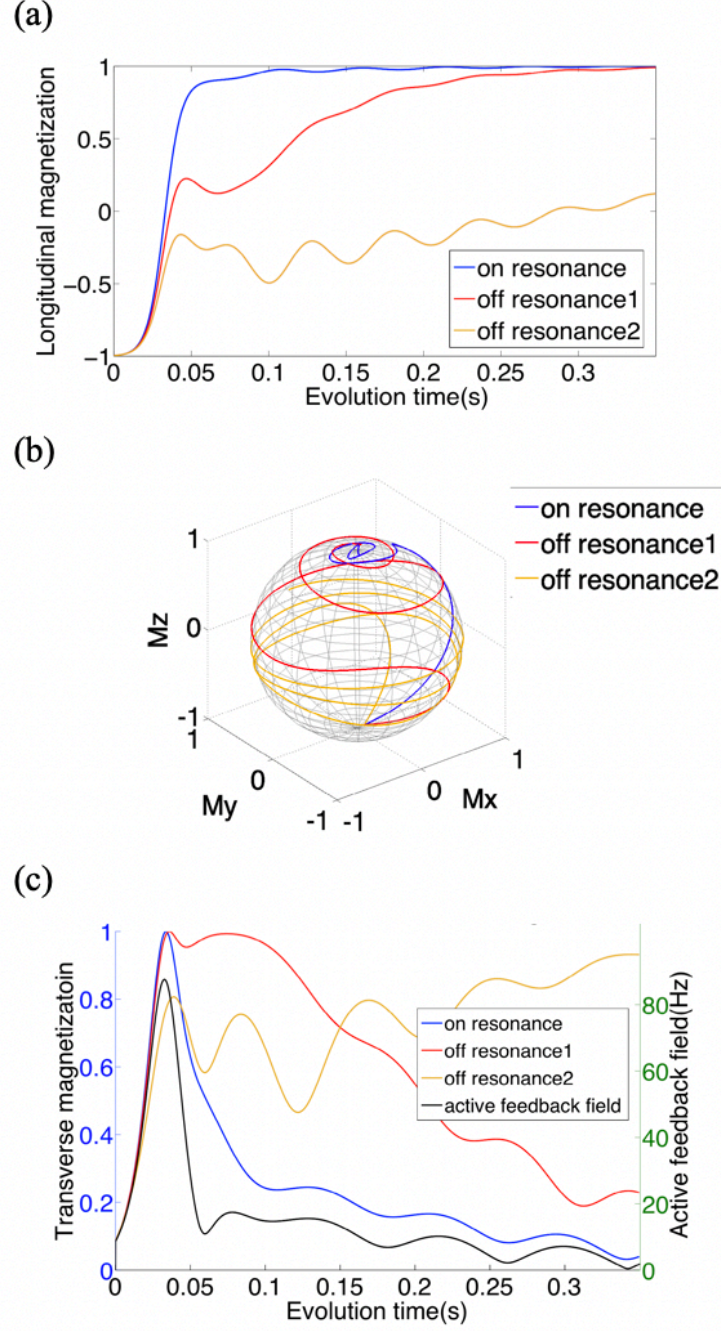


Figure 8. Selective self-excitation process of three spin groups centered at different frequencies. Three spin groups are denoted as on-resonance, off-resonance1 and off-resonance2 as they have 70%, 25% and 5% contribution to the AFF, respectively. $\varphi = 180^\circ$, $\tau_{AF} = 8\text{ms}$. (a) The plot of longitudinal magnetization under AFF. The on-resonance group (70%, blue) is driven up more

quickly than the other two packets (25%, red and 5%, yellow). (b) Spins evolution on the Bloch sphere. The on-resonance spin group is excited most efficiently and the three spin packets are distinguished. (c) The profile of the AFF and transverse magnetization. The trend of the AFF matches the on-resonance spin packet the most. It stays at a low level when the transverse magnetization of the on-resonance spin group reaches its minimum level.

Since the AFF results from the average transverse magnetization, it is very important to recover the transverse magnetization so the selective self-excitation process continues. The average transverse magnetization is recovered in two ways. Firstly, π pulses applied between each sub-block will tilt the magnetization away from fixed point so small transverse magnetization is created to reinitiate the selective-self excitation process. Secondly, π pulses refocus the dephasing transverse magnetization caused by field distortions. As the average transverse magnetization is recovered, the selective self-excitation process persists and contrast keeps growing.

The active-feedback phase was chosen to be 180° because this phase creates an AFF with a 90° lag that drives the spin toward $+z$ most effectively. The choice of the active-feedback time constant is different in each system and needs to be tested. The ideal time contrast should be small so the active-feedback strength is large enough to tilt the spins effectively and develop enough contrast before the next π pulse that reinitiates the selective self-excitation process. But a time constant too short will drive the spin to fixed point before the contrast is fully developed. Spin and contrast is frozen at the fixed point until the next π pulse.

3.3.2 Frequency Selection by Selective Self-Excitation: Multi-Cylinder Model

To understand the selective self-excitation process in the multi-cylinder model described above, only one imperfect π pulse is applied at the beginning of the process to create a small transverse magnetization. The simulation result is shown in figure 9.

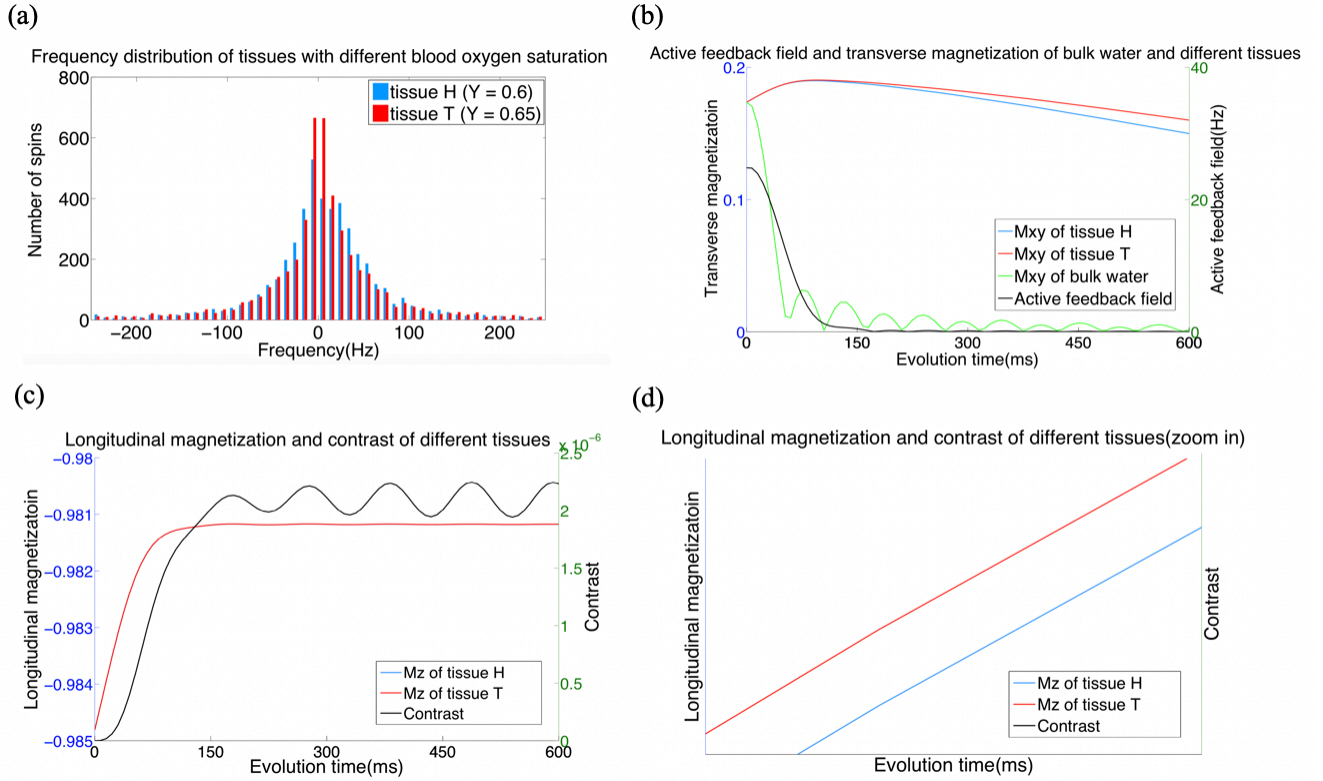


Figure 9. Simulation results based on the multi-cylinder model with one π pulse only. Feedback phase $\varphi = 180^\circ$, time constant $\tau_{AF} = 5\text{ms}$. (a) The frequency distribution of tissues with different blood-oxygen saturation ($Y_H = 0.6$ and $Y_T = 0.65$). $D = 6.63 \times 10^{-10}\text{m}^2/\text{s}$ 28,29, $a = 5.3\mu\text{m}$, $f = 6.0\%$. Tissue H: centered at 3Hz, FWHM is 60Hz. Tissue T: centered at 1Hz, FWHM is 35Hz. (b) Transverse magnetization of different spins and the AFF. The AFF is dominated by the transverse magnetization of bulk water protons. The oscillation of the bulk water magnetization is due to the background T_2 relaxation. (c) Longitudinal magnetization of tissues and the contrast. Contrast is generated and stops accumulating because the AFF vanished after transverse

magnetization of bulk water spins reaches zero. (d) Zoom in of (c). Spin in tissue T is driven to +z more effectively than spins in tissue H and two tissues are distinguished.

Similar to the simple spin model, spins in the multi-cylinder model can also be grouped into different groups with different frequencies: bulk water ^1H spins and ^1H spins in tissues with different inherent tissue properties. While all spins evolve under the AFF ($\varphi = 180^\circ$, $\tau_{\text{AF}} = 5\text{ms}$), bulk water ^1H spins are free from the deoxy-Hb-induced local-field gradient but undergo a field inhomogeneity due to T_2 relaxation ($T_2 = 200\text{ms}$) in the brain^{35,36}.

Tissues with a different degree of deoxy-Hb and blood vessel structure results in a slightly different frequency distribution. Figure 9(a) shows the spin frequency distribution in tissues with different oxygen saturation. Tissues H and T have different blood-oxygen saturation ($Y_{\text{H}} = 0.6$ ³⁹ and $Y_{\text{T}} = 0.65$) but share the same diffusion coefficient, blood-vessel size and blood volume fraction ($D = 6.63 \times 10^{-10}\text{m}^2/\text{s}$ ^{28,29}, $a = 5.3\mu\text{m}$, $f = 6.0\%$ ⁴²). The frequency distribution of tissue H is centered at 3Hz with a full width half maximum around 60Hz and the frequency distribution of tissue T is centered at 1Hz with a full width half maximum around 35Hz. Because the number of bulk water protons (100 voxels with 8000 protons in each voxel) is much greater than the number of protons in tissue H and tissue T (1 voxel with 8000 protons), the bulk water spins are on resonance and dominate the active-feedback behavior. As shown in figure 9(b), the active-feedback phase decreases as the transverse magnetization of the bulk water spins decreases despite the spins in tissue H and tissue T remaining at a very high level. The transverse magnetization of bulk water spins undergoes a periodic dephasing and rephasing process because of the T_2 relaxation in the brain.

The narrower frequency distribution and a center closer to 0Hz of tissue T as compared with that of tissue H indicates that fewer spins in tissue T shift to a high frequency domain and most of the spins remain in the on-resonance domain. Therefore, spins in tissue T are driven up more quickly than spins in tissue H due to better frequency match. As shown in figure 7(c)(d), longitudinal magnetization of tissue T is driven faster to the +z axis than those of tissue H. Hence, tissues with different blood-oxygen saturation are separated. The contrast is quite small here since only one π pulse is applied. The spin evolution and contrast accumulation stops after the transverse magnetization of bulk water spins reduces to zero or when the bulk water spins reach the fixed point²⁹.

3.3.3 MR Contrast using “++++” Pulse Sequence

Simulations were carried out using the “++++” pulse sequences with different intrinsic properties (i.e. blood-oxygen saturation, blood-vessel radius, blood volume fraction and diffusion coefficient). Baseline values used were blood-oxygen saturation $Y = 0.6$,^{31,39} blood-vessel radius $a = 5.3\mu\text{m}$, blood volume fraction $f = 6.0\%$, diffusion coefficient $D = 6.63 \times 10^{-10} \text{m}^2/\text{s}$.⁴⁰⁻⁴² Detailed parameters are shown in table 1 and table 2.

The simulation results with a changing blood-oxygen saturation using active-feedback method (AF, $t_{\text{FB}} = 2\text{ms}$, $\varphi = 180^\circ$, $\tau_{\text{AF}} = 10\text{ms}$), spin echo method (SE, $TE = 100\text{ms}$), gradient echo method (GRE, $TE = 40\text{ms}$) are shown in figure 10 and table 3. The blood-oxygen saturation in tissue H and T are $Y_{\text{H}} = 0.6$, $Y_{\text{T}} = 0.65$, respectively. Figures 10(a)(c)(e) show the longitudinal magnetization using the active-feedback method and the transverse magnetization using SE and GRE. Figures 10(b)(d)(f) show the contrast calculated from decay curves.

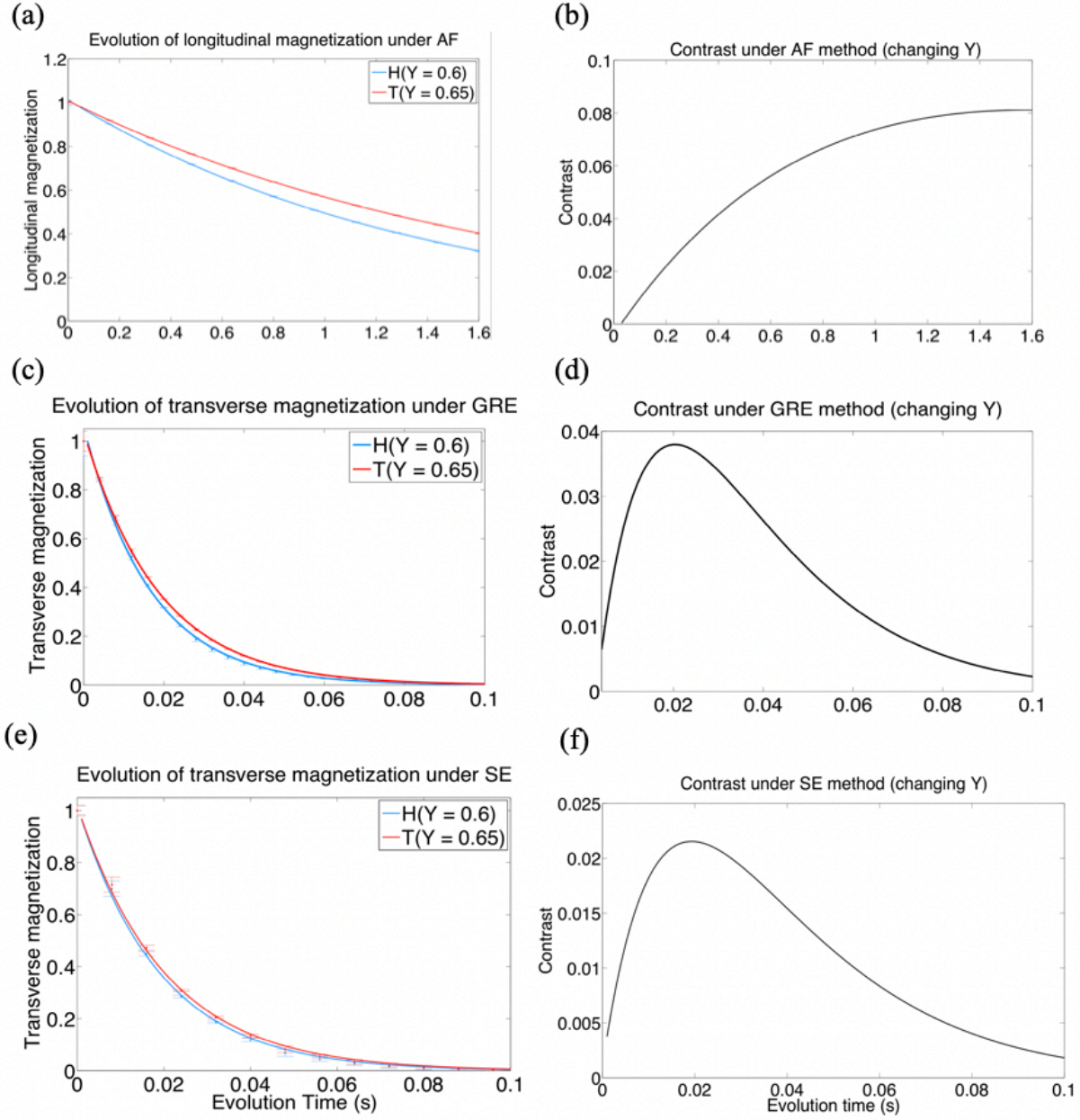


Figure 10. Simulation result (dot) and exponential fit (line) with different oxygen saturation levels ($Y_H = 0.6$ and $Y_T = 0.65$). (a) The longitudinal magnetization decay under the active-feedback method. Feedback phase $\varphi = 180^\circ$, time constant $\tau_{AF} = 10\text{ms}$, one sub-block time duration $t_{FB} = 2\text{ms}$. (b) The contrast under the active-feedback method, the maximum contrast appears at 0.083. (c) The transverse magnetization decay under the gradient echo sequence. $TE = 40\text{ms}$. (d) The

contrast under the GRE method; the maximum contrast appears at 0.037. (e) The transverse magnetization decay under the spin echo sequence. TE = 100ms. (d) The contrast under the SE method; the maximum contrast appears at 0.021.

Table 3. Relaxation time, maximum contrast and contrast enhancement using different methods with different oxygen saturation. $Y_H = 0.6$, $Y_T = 0.65$

method	Relaxation time	Max contrast	Enhancement
T_2	$T_H = 30.5\text{ms}$, $T_T = 32.4\text{ms}$	0.021	-
T_2^*	$T_H = 16.5\text{ms}$, $T_T = 18.6\text{ms}$	0.037	1.76
AF	$T_H = 1.42\text{s}$, $T_T = 1.70\text{s}$	0.083	3.95

A huge enhancement in contrast is observed in figure 10. Shown in table 3, with a 0.05 difference in blood-oxygen saturation, maximum contrast 0.083, 0.037 and 0.021 is reached using the active-feedback method, gradient echo and spin echo pulse sequence, respectively. As compared with T_2 -weighted imaging, the active-feedback method enhances the contrast by 3.95 times while T_2^* enhances contrast by 1.76 times.

Simulation result with different blood-vessel radius, a , is shown in figure 11 and table 4. The radius in tissue H and T are $a_H = 5.3 \mu\text{m}$, $a_T = 6.5 \mu\text{m}$, respectively.

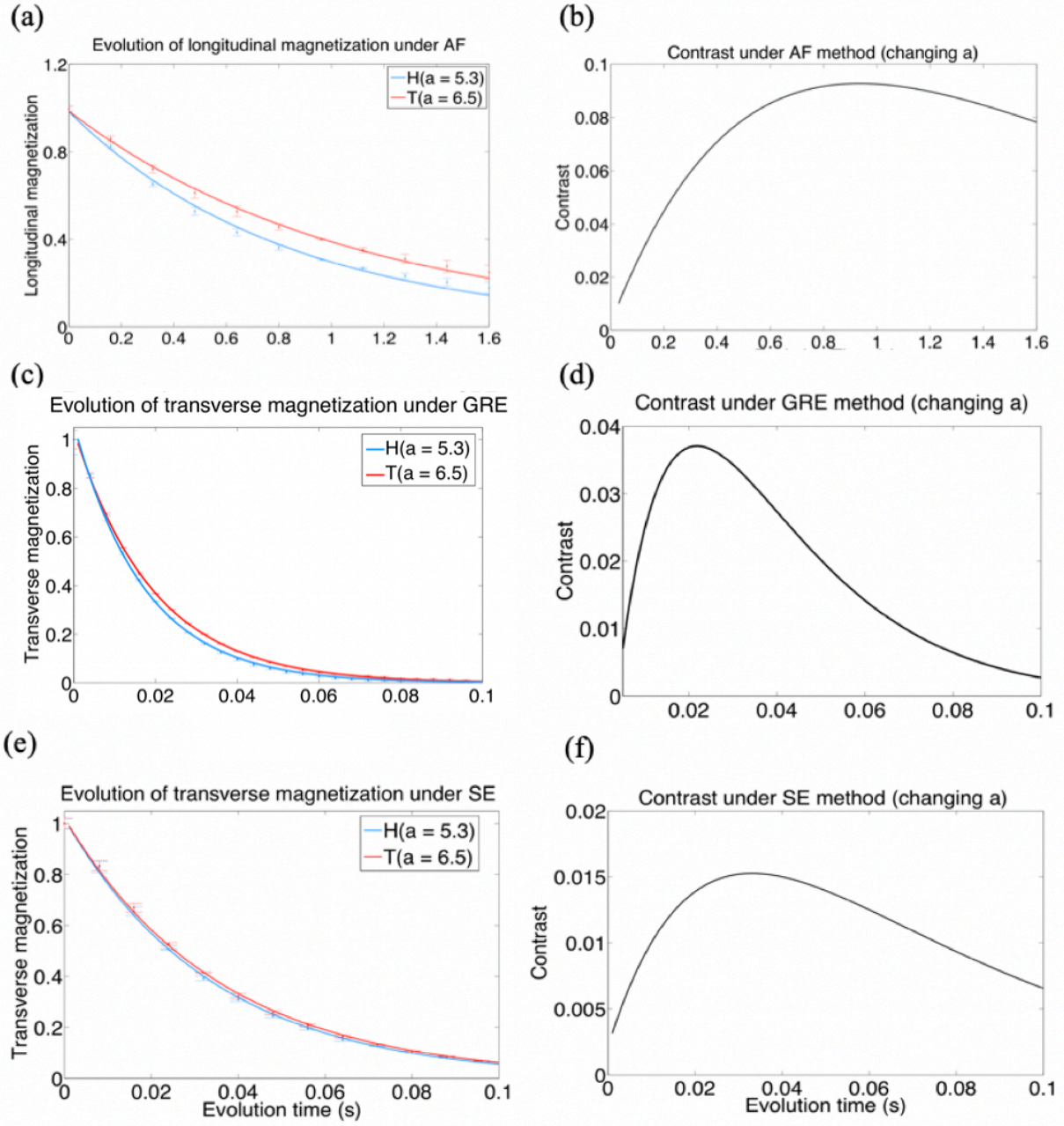


Figure 11. Simulation result (dot) and exponential fit (line) with different blood-vessel radii ($a_H = 5.3 \mu\text{m}$, $a_T = 6.5 \mu\text{m}$). (a) The longitudinal magnetization decay under the active-feedback method. Feedback phase $\varphi = 180^\circ$, time constant $\tau_{AF} = 10\text{ms}$, one sub-block time duration $t_{FB} = 2\text{ms}$. (b) The contrast under the active-feedback method, the maximum contrast appears at 0.093. (c) The transverse magnetization decay under the gradient echo sequence. $TE = 40\text{ms}$. (d) The contrast

under the GRE method, the maximum contrast appears at 0.037. (e) The transverse magnetization decay under the spin echo sequence. TE = 100ms. (d) The contrast under the SE method, the maximum contrast appears at 0.015.

Table 4. Relaxation time, maximum contrast and contrast enhancement using different method with different blood-vessel radii. $a_H = 5.3 \mu\text{m}$, $a_T = 6.5 \mu\text{m}$

method	Relaxation time	Max contrast	Enhancement
T_2	$T_H = 34.3\text{ms}$, $T_T = 35.7\text{ms}$	0.015	-
T_2^*	$T_H = 17.2\text{ms}$, $T_T = 19.3\text{ms}$	0.037	2.47
AF	$T_H = 0.83\text{s}$, $T_T = 1.12\text{s}$	0.093	6.20

With a $1.2\mu\text{m}$ difference in blood-vessel radius, active-feedback method, gradient echo and spin echo pulse sequences generate maximum contrast 0.093, 0.037 and 0.015, respectively. As compared with T_2 -weighted imaging, the active-feedback method enhances the contrast by 6.20 times and T_2^* enhances contrast by 1.76 times.

Simulation results with different diffusion coefficient are shown in figure 12 and table 5. The diffusion coefficient in tissue H and T are $D_H = 6.63 * 10^{-10} \text{ m}^2/\text{s}$, $D_T = 7.5 * 10^{-10} \text{ m}^2/\text{s}$, respectively.

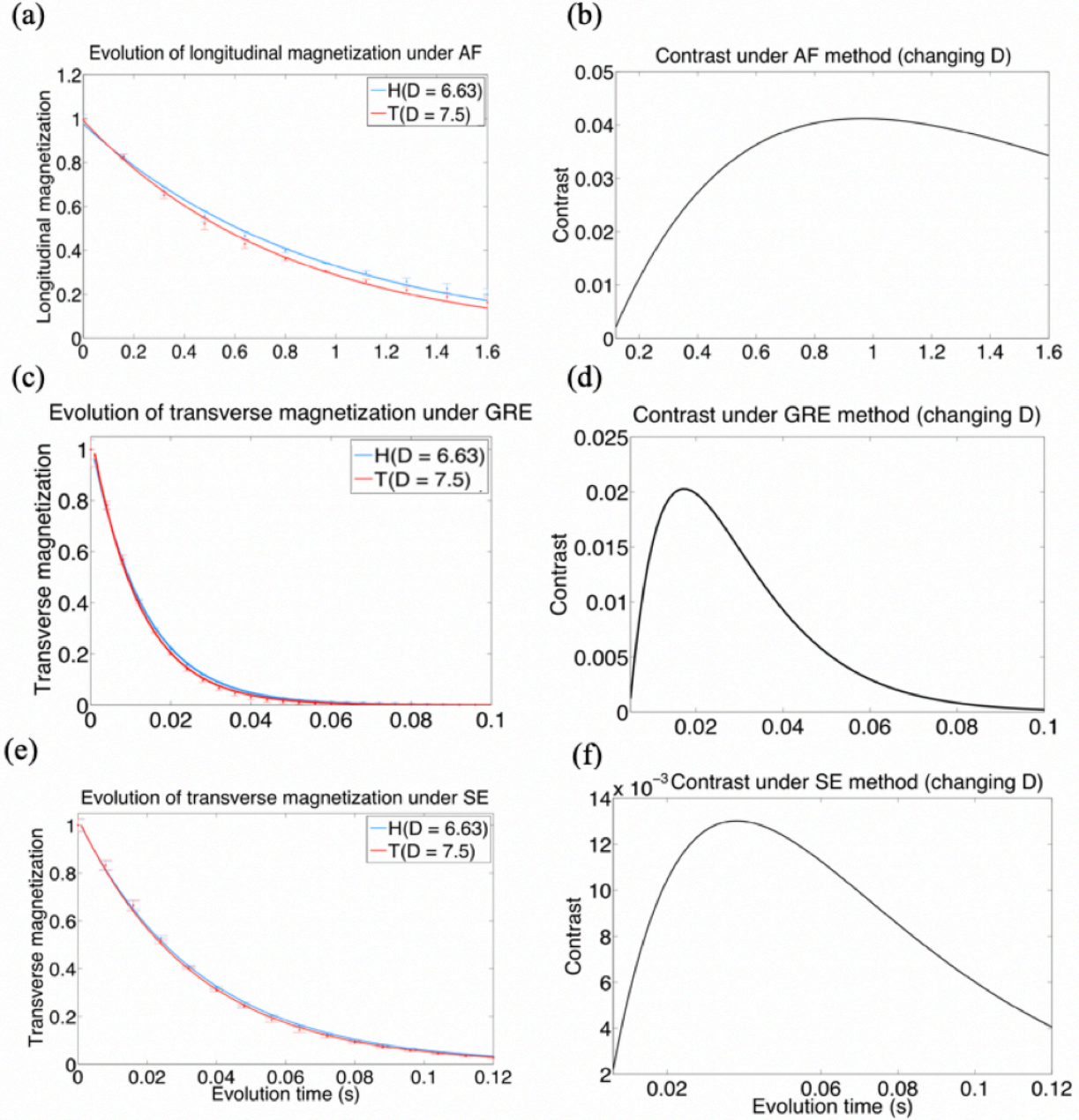


Figure 12. Simulation result (dot) and exponential fit (line) with different diffusion coefficients in tissue H and T, $D_H = 6.63 \times 10^{-10} \text{ m}^2/\text{s}$, $D_T = 7.5 \times 10^{-10} \text{ m}^2/\text{s}$. (a) The longitudinal magnetization decay under the active-feedback method. Feedback phase $\varphi = 180^\circ$, time constant $\tau_{AF} = 10\text{ms}$, one sub-block time-duration $t_{FB} = 2\text{ms}$. (b) The contrast under the active-feedback method, the maximum contrast appears at 0.041. (c) The transverse magnetization decay under the

gradient echo sequence. TE = 40ms. (d) The contrast under the GRE method; the maximum contrast appears at 0.022. (e) The transverse magnetization decay under the spin echo sequence. TE = 100ms. (d) The contrast under the SE method, the maximum contrast appears at 0.013.

Table 5. Relaxation time, maximum contrast and contrast enhancement using different method with different diffusion coefficients $D_H = 6.63 * 10^{-10} m^2/s$, $D_T = 7.5 * 10^{-10} m^2/s$

method	Relaxation time	Max contrast	Enhancement
T_2	$T_H = 35.0ms$, $T_T = 33.7ms$	0.013	-
T_2^*	$T_H = 13.0ms$, $T_T = 12.1ms$	0.022	1.96
AF	$T_H = 0.92s$, $T_T = 0.81s$	0.041	3.17

With a small difference in diffusion coefficients, the active-feedback method, gradient echo and spin echo pulse sequences generate maximum contrast 0.041, 0.022 and 0.013, respectively. As compared with T_2 -weighted imaging, the active-feedback method enhances the contrast by 3.17 times and T_2^* enhances contrast by 1.96 times.

A simulation result with different blood volume fractions is shown in figure 13 and table 6. The blood volume fraction in tissue H and T are $f_H = 5\%$, $f_T = 3\%$, respectively. Figure 13(a)(c)(e) show the longitudinal magnetization using the active-feedback method and the transverse magnetization using SE and GRE. Figure 13(b)(d)(f) show the contrast calculated from the decay curves.

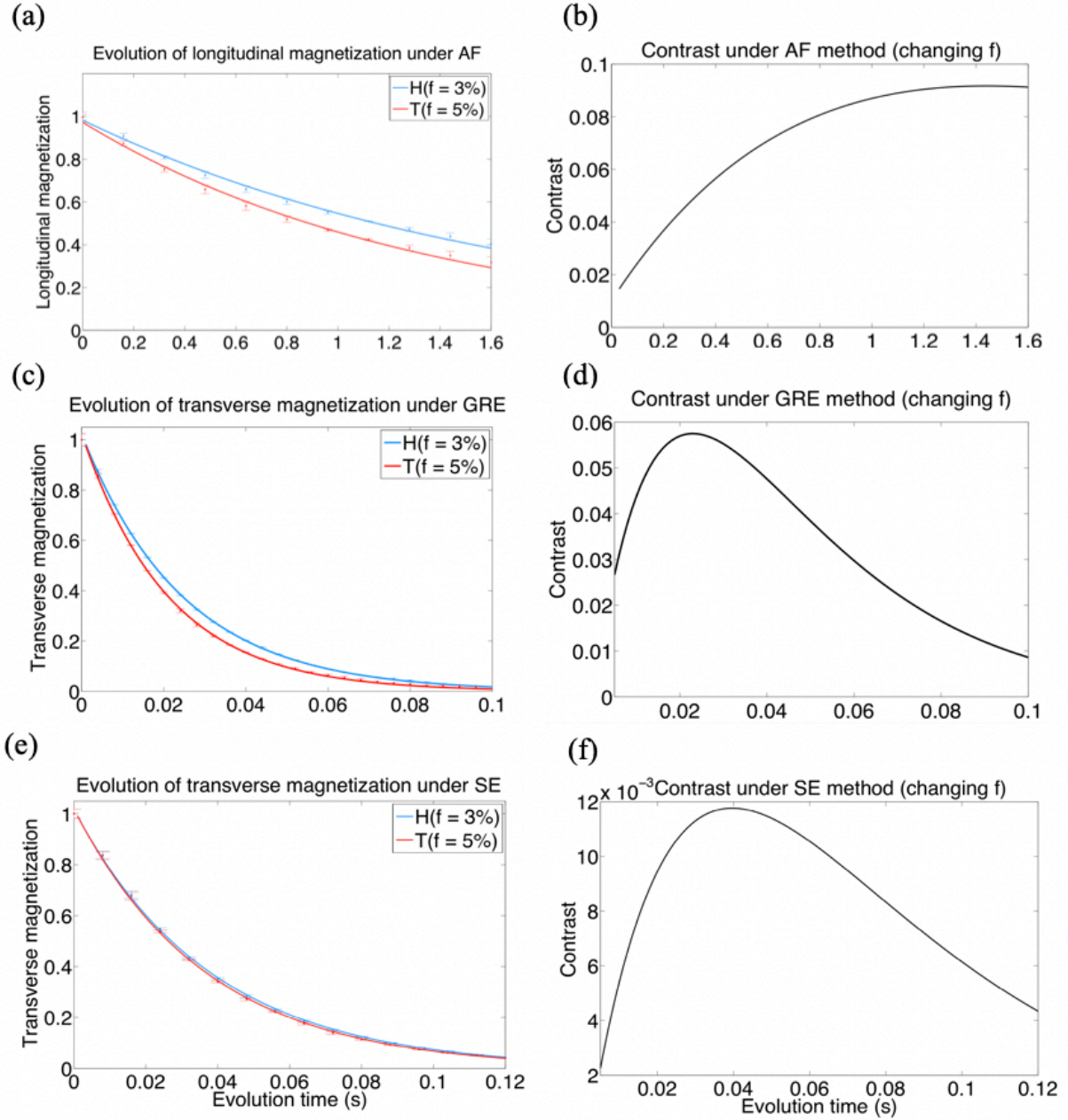


Figure 13. Simulation result (dot) and exponential fit (line) with different blood volume fractions in tissue H and T, $f_H = 5\%$, $f_T = 3\%$. (a) The longitudinal magnetization decay under the active-feedback method. Feedback phase $\varphi = 180^\circ$, time constant $\tau_{AF} = 10\text{ms}$, one sub-block time-duration $t_{FB} = 2\text{ms}$. (b) The contrast under the active-feedback method, the maximum contrast appears at 0.092. (c) The transverse magnetization decay under the gradient echo sequence. TE =

40ms. (d) The contrast under the GRE method, the maximum contrast appears at 0.058. (e) The transverse magnetization decay under the spin echo sequence. TE = 100ms. (d) The contrast under the SE method, the maximum contrast appears at 0.012.

Table 6. Relaxation time, maximum contrast and contrast enhancement using different method with different blood volume fractions $f_H=5\%$, $f_T=3\%$.

method	Relaxation time	Max contrast	Enhancement
T_2	$T_H= 38.1\text{ms}$, $T_T=36.9\text{ms}$	0.012	-
T_2^*	$T_H= 24.6\text{ms}$, $T_T= 21.1\text{ms}$	0.058	4.83
AF	$T_H= 1.70\text{s}$, $T_T= 1.33\text{s}$	0.092	7.67

The active-feedback method, gradient echo and spin echo pulse sequence generates maximum contrast of 0.092, 0.058 and 0.012, respectively. As compared with T_2 -weighted imaging, the active-feedback method enhances the contrast by 7.67 times and T_2^* enhances contrast by 4.83 times.

The results of T_2 and T_2^* match literature results^{30,31}.

Contrast is significantly enhanced by active-feedback method in all tested conditions with only a small change in tissue properties. In addition to a huge contrast enhancement, the contrast is more robust since the spin dynamic freezes at fixed point and the maximum contrast is locked.

The longitudinal magnetization decays much more slowly than the transverse magnetization essentially because the longitudinal component is insensitive to the field inhomogeneity. In addition, the AFF has the effect of bringing the magnetization to $+z$. The slow decay of longitudinal magnetization allows full development of contrast.

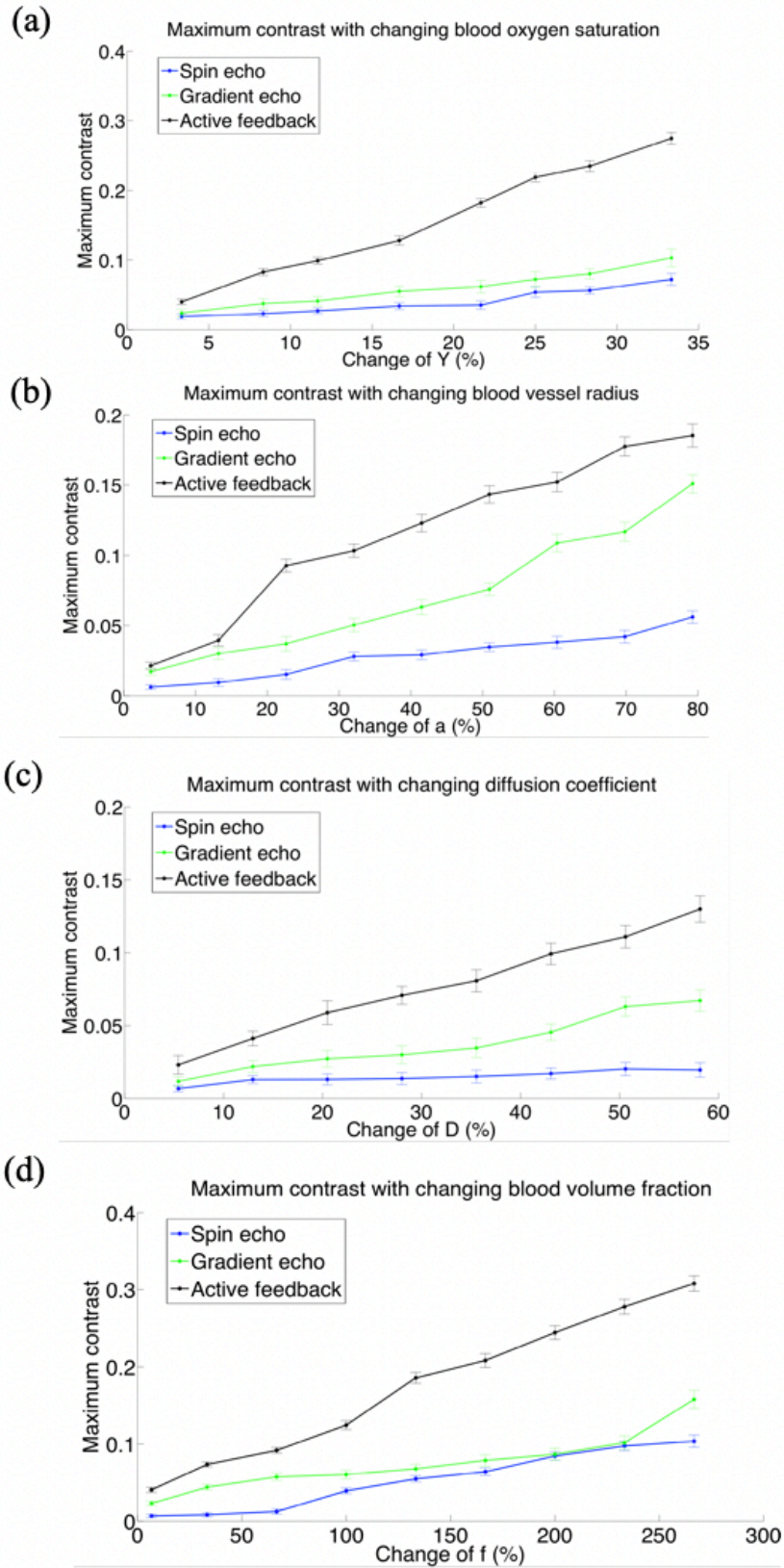


Figure 14. Maximum contrast with different percentage changes in (a) blood-oxygen saturation, (b) blood-vessel radius, (c) blood volume fraction and (d) diffusion coefficient. Baseline values used: Blood-oxygen saturation $Y = 0.6$, Blood-vessel radius $a = 5.3\mu\text{m}$, Blood volume fraction $f = 6.0\%$, Diffusion coefficient $D = 6.63 \times 10^{-10} \text{m}^2/\text{s}$.

Contrast with broader differences in tissue properties were calculated and shown in figure 14. When one parameter is altered, the rest are held constant using baseline values shown in table 1. It matches the expectation that the contrast becomes larger in both methods when there is a larger difference in inherent tissue properties. However, the contrast resulting from the active-feedback method always outperforms that from the gradient echo and the spin echo methods. Specifically, as compared to the SE method, the contrast is enhanced 2.0 times with a 3% difference in blood-oxygen saturation, 3.5 times with a 4% difference in blood-vessel radius, 6.1 times with a 7% difference in blood volume fraction, and 3.4 times with a 5% difference in diffusion coefficient. As compared to the GRE method, the contrast is enhanced 1.7 times with a 3% difference in blood-oxygen saturation, 1.3 times with a 4% difference in blood-vessel radius, 1.8 times with a 7% difference in blood volume fraction, and 2.0 times with a 5% difference in diffusion coefficient.

It is important to notice that increasing the difference in an intrinsic property will raise the contrast in all three methods, but the active-feedback method provides a better contrast under all conditions, which means that the active-feedback method is more sensitive to small local variations. However, the enhancement using the active-feedback decreases as the property differs more. It is due to the fact that the spin echo and the gradient echo methods have the ability to distinguish tissues when the differences in inherent properties are sufficiently. There is no direct relationship

between the percentage increase in intrinsic property and the percentage increase in contrast because the baseline values chosen play an important role in the spin evolution. Moreover, different intrinsic properties have different mechanisms of field inhomogeneity and contrast generation. The oxygen saturation level directly relates to the level of deoxy-Hb and thus affects local magnetic field inhomogeneity^{3,5,43}. The diffusion coefficient does not affect the local magnetic field and frequency shift directly but it controls the movement of spin and influences the field gradient experienced in each step, thus, affecting the spin relaxation⁴⁴ and the AFF. The volume fraction and blood-vessel size have more complicated mechanisms since they affect both the frequency distribution and the spin motion^{30,33,44}.

The MR contrast observed can be understood by the frequency shift due to different inherent properties. Tissues with lower blood-oxygen level, higher blood volume fraction, small blood-vessel size and/or faster diffusion have more field distortion³⁸, and thus produce a longer frequency shift. Those spins with large frequency shift will not be tilted due to frequency mismatch while spins that meet the on-resonance condition are tilted towards the +z direction, which results a spread of magnetization along the z direction. Consequently, contrast is generated along the z direction between tissues with different intrinsic properties.

The contrast from the active-feedback method is more conspicuous due to the novel contrast enhancement mechanism. The MR contrast in the transverse plane from the spin echo method depends on the width of the frequency distribution. In the case that the width does not differ much, the spin echo and gradient echo methods lose their power. However, as discussed above the MR contrast generated by the active-feedback method results from the frequency shift. Although the width does not differ, the large frequency shift always exists and the MR contrast along the z direction can be observed.

3.4 Conclusions

In this work, active-feedback magnetic resonance was introduced to improve sensitivity to intrinsic tissue properties and enhance contrast. This method is conceptually new because it allows the spin to be self-excited by adding an active-feedback field that depends on the average transverse magnetization. The active-feedback method is extremely sensitive to small field inhomogeneity. Significant and robust contrast were confirmed by the Monte Carlo simulation. Contrast is enhanced by 2.0 times with a 3% difference in blood-oxygen saturation, 3.5 times with a 4% difference in blood-vessel radius, 3.4 times with a 5% difference in diffusion coefficient and 7.6 times with a 7% difference in blood volume fraction when it is compared with the spin echo method. And contrast is enhanced 1.7 times with a 3% difference in blood-oxygen saturation, 1.3 times with a 4% difference in blood-vessel radius, 1.8 times with a 7% difference in blood volume fraction, and 2.0 times with a 5% difference in diffusion coefficient when compared with the gradient echo method. This huge contrast enhancement makes the MRI technique more powerful in research and clinical use.

The essential advantages of the active-feedback method in comparison with the traditional MRI methods are twofold. Firstly, the huge contrast enhancement under different conditions is confirmed by the simulation results. The fundamental difference between this new method and the other methods is result of in the selective self-excitation. The active-feedback can be viewed as a continuous RF pulse generated by the magnetization itself. Hence, the excitation and nutation are directed by the magnetization itself. However, the evolution in traditional methods is dominated by T_1 and T_2 relaxation, which can be too short to develop contrast beyond the noise level.

Secondly, the active-feedback field shows promise in creating not only an enhanced but also a robust contrast because of the dependence of the active-feedback field on the on-resonance spin. When the on-resonance spin reaches the fixed point with a small transverse magnetization, the active-feedback field is diminished and prevents the off-resonance spin from catching up. Therefore, the large contrast is locked.

References

- [1] Weinmann, H. J., Brasch, R. C., Press, W. R., Press, G. E. Characteristics of Gadolinium-DTPA Complex: A Potential NMR Contrast Agent. American Roentgen Ray Society 1983, 142 (6), 619-624.
- [2] Zlokovic, B.V. Neurovascular pathways to neurodegeneration in Alzheimer's disease and other disorders. Nature Reviews Neuroscience 2014, 12 (12), 723-738.
- [3] Pauling, L. & Coryell, C. D. The magnetic properties and structure of hemoglobin, oxyhemoglobin and carbonmonoxy hemoglobin. Proc Natl Acad Sci 1936, 22, 210-216.
- [4] Hoppel, B. E., Weisskoff, R. M., Thulborn, K. R., Moore, J. B., Kwong, K. K. & Rosen, B. R. Measurement of regional blood-oxygenation and cerebral hemodynamics. Magnetic Resonance in Medicine 1993, 30(6), 715-723.
- [5] Silvennoinen, M. J., Clingman, C. S., Golay, X., Kauppinen, R. A., van Zijl, P. C. M. Comparison of the dependence of blood R2 and R2* on oxygen saturation at 1.5 and 4.7 Tesla. Magnetic Resonance in Medicine 2003, 49(1), 47-60.
- [6] Posse, S., Cuenod, C. A., Le Bihan, D. Human brain: proton diffusion MR spectroscopy. Radiology 2014, 188(3), 719-725.
- [7] Bradley, W. G., Waluch, V. Blood Flow: Magnetic Resonance Imaging. Radiology 1985, 154, 443-450.
- [8] Huang, S. Y., Chung, A. P., Lin, Y. Y. Visualizing Feedback-Enhanced Contrast in Magnetic Resonance Imaging. Concepts Magn. Reson. 2007, 36A(6), 378-393.
- [9] Datta, S., Huang, S. Y., Lin, Y.-Y. Understanding Spin Turbulence in Solution Magnetic Resonance Through Phase Space Dynamics and Instability. Concepts Magn. Reson. 2006, 28A(6), 410-421.

- [10] Huang, S. Y., Anklin, C., Walls, J. D., Lin, Y. Y. Sizable concentration-dependent frequency shifts in solution NMR using sensitive probes. *Journal of the American Chemical Society* 2004, 126(49), 15936-15937.
- [11] Huang, S. Y., Wolahan, S. M., Mathern, G. W., Chute, D. J., Akhtari, M., Nguyen, S. T., Huynh, M. N., Salamon, N. Lin, Y. Y. Improving MRI differentiation of gray and white matter in epileptogenic lesions based on nonlinear feedback. *Magnetic Resonance in Medicine* 2006, 56(4), 776-786.
- [12] Jeener, J., Vlassenbroek, A., Broekaert, P. Unified derivation of the dipolar field and relaxation terms in the Bloch-Redfield equations of liquid NMR. *The Journal of Chemical Physics* 1995, 103(4), 1309-1332.
- [13] Khitrin, A. K., Jerschow, A. Simple suppression of radiation damping. *Journal of Magnetic Resonance* 2012, 225, 14-16.
- [14] Abergel, D. Chaotic solutions of the feedback driven Bloch equations. *Physics Letters, Section A: General, Atomic and Solid State Physics* 2002, 302(1), 17-22.
- [15] Warren, W. S., Hammes, S. L., Bates, J. L. Dynamics of radiation damping in nuclear magnetic resonance. *Physical Review* 1989, 91(10), 5895.
- [16] Augustine, M. P. Transient properties of radiation damping. *Progress in Nuclear Magnetic Resonance Spectroscopy* 2002, 40, 111-150.
- [17] Li, Z., Hsu, C. H., Dimitrov, N., Hwang, D. W. Chang, H. W., Hwang, L. P., Lin, Y. Y. Sensitive imaging of magnetic nanoparticles for cancer detection by active feedback MR. *Magnetic Resonance in Medicine* 2015, 74, 33-41.
- [18] Goldman, M. Advances in magnetic resonance: Formal theory of spin-lattice relaxation. *Journal of Magnetic Resonance* 2001, 149(2), 160-187.

- [19] Bloch, F. Nuclear induction. *Physical Review* 1946, 70, 460-474.
- [20] Yokoo, T., Bae, W. C., Hamilton, G., Karimi, A., Borgstede, J. P., Bowen, B. C., Sirlin, C. B., Chung, C. B., Crues, J.V., Bradley, W. G., Bydder G. M. A Quantitative Approach to Sequence and Image Weighting. *Journal of Computer Assisted Tomography* 2010, 34(3), 317-331.
- [21] Elster, A. D. An index system for comparative parameter weighting in MR imaging. *Journal of Computer Assisted Tomography* 1988, 12(1), 130-134
- [22] Mintorovitch, J., Moseley, M. E., Chileuitt L., Shimizu H., Cohen Y., Weinstein P. R. Comparison of diffusion- and T2-weighted MRI for the early detection of cerebral ischemia and reperfusion in rats. *Magnetic Resonance in Medicine* 1991, 18, 39-50.
- [23] Muller, R. N.; Gillis, P.; Moiny, F.; Roch, A. Transverse Relaxivity of Particulate MRI Contrast Media: from Theories to Experiments. *Magnetic Resonance in Medicine* 1991, 22, 178-182.
- [24] Mugler J. P. III. Basic principles. In: Edelman R. R., Hesselink J. R., Zlatkin M. B., Crues J. V., eds. *Clinical magnetic resonance imaging*. 3rd ed. Philadelphia, Pa: Saunders Elsevier, 2006; 23-57.
- [25] Nitz W. R., Reimer P. Contrast mechanisms in MR imaging. *European Radiology* 1999, 9, 1032-1046.
- [26] Haacke E. M., Tkach J. A., Parrish T. B. Reduction of T2* dephasing in gradient field-echo imaging. *Radiology* 1989, 70, 457-462.
- [27] Chavhan G. B., Babyn P. S., Thomas B., Shroff, M. M., Haacke, M. Principles, techniques, and applications of T2*-based MR imaging and its special applications. *Radiographics* 2009, 29, 1433-1449.

- [28] Feinberg D. A., Mills C. M., Posin J. P., Ortendahl D. A., Hylton N. M., Crooks, L. E., Watts J. C., Kaufman L., Arakawa M., Hoenninger J. C., Zawadzki M. B. Multiple spin-echo magnetic resonance imaging. *Radiology* 1985, 155, 437-442.
- [29] Ishiyama K., Hashimoto M., Izumi J., Watarai J., Shibata S., Sato T., Yamamoto Y. Tumor-liver contrast and subjective tumor conspicuity of respiratory-triggered T2-weighted fast spin-echo sequence compared with T2*-weighted gradient recalled-echo sequence for ferucarbotran-enhanced magnetic resonance imaging of hepatic malignant tumors. *J Magn Reson Imaging* 2008, 27(6), 1322–1326.
- [30] Boxerman, J. L., Hamberg, L. M., Rosen, B. R. & Weisskoff, R. M. MR Contrast Due to Intravascular Magnetic Susceptibility Perturbations. *Magnetic Resonance in Medicine* 1995, 34 (4), 555-566.
- [31] Uludag, K., Müller-Bierl, B., Ugurbil, K. An integrative model for neuronal activity-induced signal changes for gradient and spin echo functional imaging. *NeuroImage* 2009, 48, 150-165.
- [32] Yablonskiy, D. A., Haacke, E. M. Theory of NMR Signal Behavior in Inhomogeneous Tissues: The Static Dephasing Regime. *Magnetic Resonance in Medicine* 1994, 32, 749-763.
- [33] Ogawa, S., Menon, R. S., Tank, D. W., Kim, S. G., Merkle, H., Ellermann, J. M., Ugurbil, K. Functional brain mapping by blood-oxygenation level-dependent contrast magnetic resonance imaging. *Biophysical journal* 1993, 64, 803-812.
- [34] Spees, W. M., Yablonskiy, D. A., Oswood, M. C., Ackerman, J. J. H. Water Proton MR Properties of Human Blood at 1 . 5 Tesla : Magnetic Susceptibility , T1 , T2 , T* and Non-Lorentzian Signal Behavior. *Magnetic Resonance in Medicine* 2001, 45, 533-542.

- [35] Darwin, R. H., Drayer, B. P., Riederer, S. J., Wang, H. Z., Macfall, J. R. T2 Estimates in Healthy and Diseased Brain Tissue: A Comparison Using Various MR Pulse Sequence. *Radiology* 1986, 160, 375-381.
- [36] Li, Y., Srinivasan, R., Ratiney, H., Lu, Y., Chang, S. M. Nelson, S. J. Comparison of T1 and T2 metabolite relaxation times in glioma and normal brain at 3T. *Journal of Magnetic Resonance Imaging* 2008, 28(2), 342-350.
- [37] Pawlik, G., Rackl, A., Bing, R. J. Quantitative Capillary Topography and Blood Flow in the Cerebral cortex of Cats: an in vivo Microscopic study. *Brain research* 1981, 208, 35-58.
- [38] Weisskoff, R., Zuo, C. S., Boxerman, J. L., Rosen, B. R. Microscopic susceptibility variation and transverse relaxation: Theory and experiment. *Magnetic Resonance in Medicine* 1994, 31(6), 601-610.
- [39] Yao, J., Maslov, K. I., Zhang, Y., Xia, Y., Wang, L. V. Label-free oxygen-metabolic photoacoustic microscopy in vivo. *Journal of Biomedical Optics* 2011, 16(7), 076003.
- [40] Hoehn-Berlage, M., Eis, M., Schmitz, B. Regional and directional anisotropy of apparent diffusion coefficient in rat brain. *NMR in Biomedicine* 1999, 12, 45-50.
- [41] Le Bihan, D. Looking into the functional architecture of the brain with diffusion MRI. *Nature Reviews Neuroscience* 2003, 4, 469-480.
- [42] Bouchet, A., Bidart, M., Miladi, I., Le Clec'h, C., Serduc, R., Coutton, C., Regnard, P., Khalil, E., Dufort, S., Lemasson, B., Laissue, J., Pelletier, L. Le Duc, G. Characterization of the 9L gliosarcoma implanted in the Fischer rat: An orthotopic model for a grade IV brain tumor. *Tumor Biology* 2014, 35(7), 6221-6233.

- [43] Bren, K. L., Eisenberg, R., Gray, H. B. Discovery of the magnetic behavior of hemoglobin: A beginning of bioinorganic chemistry. *Proceedings of the National Academy of Sciences* 2015, 112(43), 13123-13127.
- [44] Boxerman, J. L., Bandettini, P. A., Kwong, K. K., Baker, J. R., Davis, T. L., Rosen, B. R., Weisskoff, R. M. The intravascular contributions of fMRI signal change: Monte Carlo modeling and diffusion-weighted studies. *Magnetic Resonance in Medicine* 1995, 34, 4-10.

Chapter 4

Local-Magnetic-Field-Dependent Active-Feedback Magnetic Resonance and its Application in Early Glioblastoma Detection

4.0 Abstract

Glioblastoma multiforme (GBM), a graded IV astrocytoma, is the most aggressive and fatal brain cancer found in humans. However, the detection of early-stage glioblastoma remains unsolved. For this purpose, local-magnetic-field dependent active-feedback magnetic resonance is introduced to detect the field variations in early GBM due to differences in deoxyhemoglobin concentration and vasculature. We take advantage of the slightly lower deoxyhemoglobin (deoxy-Hb) concentration, and higher vascular size in early GBM and a new technique termed “active-feedback magnetic resonance” to sensitively detect the early-stage GBM. To further enhance the contrast, the active-feedback MR was designed to be dependent on the deoxy-Hb-induced local magnetic field.

Monte Carlo simulation was carried out to test the validity of this technique. Monte Carlo simulations showed that the local-field dependent active-feedback MR enhanced the contrast 8.4 times in comparison to spin echo T_2 -weighted imaging and 6.8 times in comparison with T_2^* -weighted image with only 3% change in blood-oxygen level. Contrast in early GBM model was improved by 2.3 times as compared to active-feedback MRI without local-field dependence, by 5.2 times as compared to the conventional gradient echo method and by 7.2 times as compared to the conventional spin echo method. The local-magnetic-field dependent active-feedback MR can

create a narrower selective self-excitation profile, which can be translated into more sensitive detection of the magnetic susceptibility variations in GBM tissues.

4.1 Introduction

Glioblastoma multiforme (GBM), a graded IV astrocytoma, is the most aggressive and fatal brain cancer found in humans^{1,2}. Enhancing the imaging contrast in early detection of high-grade malignancy, such as glioblastoma multiforme significantly increases not only the treatment options available, but also the patient survival rate.

Early-stage GBM is characterized by hypermetabolism and hyperoxia^{3,4} and abnormal vasculature development^{5,6}. The higher level of oxygen saturation indicates a decreased level of deoxygenated hemoglobin (deoxy-Hb)⁷, an iron-containing oxygen-transport metalloprotein that exhibits paramagnetism and induces irreversible magnetic fields^{8,9}. Studies also have shown that the blood-vessel size is significantly increased in early-stage GBM and continues to grow in later stage^{3,12} which alters field inhomogeneity and proton movement, thus having a significant effect on MR relaxation^{10,13,14}. Relaxation-based MR contrast mechanisms like T_1 -, T_2 - and T_2^* -weighted images are the most fundamental and powerful tools for tumor detection. However, these methods fail to detect GBM at early-stage because differences between the tumor and the surrounding healthy tissue are subtle¹⁵.

An advanced MR method called active-feedback MR was introduced to enhance the contrast¹⁶. Active-feedback field (AFF) is manually added on the transverse plane to induce nonlinear spin behavior¹⁷⁻¹⁹. Earlier work has shown that the active-feedback MR is capable of distinguishing tissues with subtle differences in blood-oxygen saturation, blood vessel structure and diffusion coefficient. In this work, active-feedback characteristics and mechanism are further explored. Specifically, we introduce a local-magnetic-field dependent active-feedback method. In

Chapter 3, the AFF is identical everywhere despite the local field inhomogeneity. However, in this work, this field is modified based on the local magnetic field. Such modification is achieved by making the active-feedback-phase dependent on the local magnetic field.

Computational work has been done to illustrate the mechanism of the local-magnetic-field dependent active-feedback method. Monte Carlo simulation shows that with only a 3% change in blood-oxygen saturation, the local-field dependent active-feedback MR enhanced the contrast 8.4 times as compared to the spin echo method, 6.8 times as compared to the gradient echo method and 4.2 times as compared to the previous active-feedback method without local-field dependence. Moreover, the method was applied on early-stage GBM to illustrate the potential application. The contrast was significantly increased to 0.301, which is a 7.2 times enhancement in comparison with the spin echo method, 5.2 times enhancement in comparison with the gradient echo method and 2.3 times enhancement in comparison with traditional active-feedback MR. The local-magnetic-field dependent active-feedback method creates a robust improvement in signal contrast when compared to the traditional active-feedback method, spin echo and gradient echo methods, which makes early GBM detection possible.

4.2 Theory and Method

4.2.1 AFF and Selective Self-Excitation

In addition to the local magnetic field induced by deoxy-Hb^{4,8,20}, an AFF is introduced to the system to sensitively detect the local field distortion. The field can be described as^{21,22}:

$$\gamma \vec{B}_{+,AF}(t) = \frac{1}{\tau_{AF}} \langle i \vec{m}_{+}(\vec{r}, t) \rangle e^{i\varphi} \quad (1)$$

where γ is the gyromagnetic ratio and $m_{+}(t) \equiv m_x + im_y$ is the normalized transverse magnetization with respect to the equilibrium magnetization of pure water. The AFF, $B_{+,AF}(t) \equiv$

$B_{AF,x} + iB_{AF,y}$, is added in the transverse plane. The inverse of the feedback time constant τ_{AF} describes the feedback strength. The AFF becomes greater when τ_{AF} is shorter. The feedback phase φ characterizes the angle between the feedback field $\vec{B}_{+,AF}$ and the transverse magnetization $\vec{m}_{+}(\vec{r}, t)$.

The addition of the AFF successfully renders the spin behavior nonlinear^{22,23} and enhances contrast through a selective self-excitation process^{4,24}. The spin dynamics have been illustrated in Chapter 3. To summary, the core of active-feedback MR is to add an AFF to the transverse plane that tilts the water ^1H spins up or down at different efficiency based on their precession frequency. Since the average transverse magnetization $\langle \vec{m}_{+}(\vec{r}, t) \rangle$ is mainly contributed from bulk water ^1H spins that are far away from the dipolar center, according to Eqn. (1), the AFF $\vec{B}_{+,AF}$ will possess a frequency that matches the procession frequency of the bulk water ^1H magnetization. Thus, bulk water spins are on-resonance and tilted more effectively than those spins around the dipolar center with a procession frequency far from the AFF frequency.²⁵ Contrast along the z direction is generated when the bulk water ^1H magnetization is effectively driven up or down while the ^1H magnetization near the dipolar center is still near the original position. As shown in figure 1, bulk water protons (blue arrows) are effectively driven up by AFF while protons near the dipolar center (black arrow) stay near their original position. As a result, contrast along z direction is created.

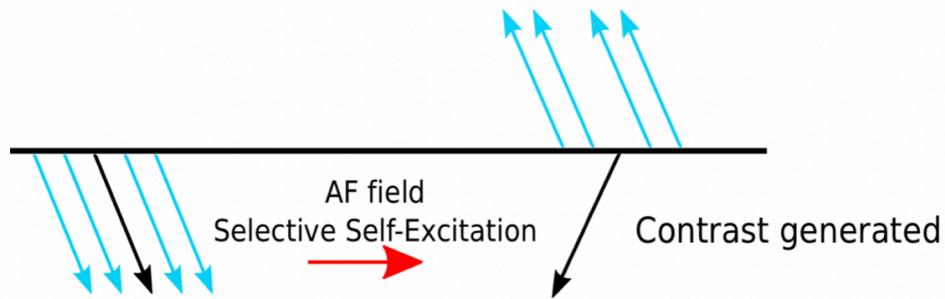


Figure 1. Demonstration of contrast along the z direction created by selective self-excitation. All spins are originally near $-z$. Selective self-excitation tilts bulk water spins (blue arrows) up since they are on-resonance while spins that are near dipolar center (black arrows) are off-resonance and remain around original orientation. As a result, contrast along the z direction is generated.

4.2.2 Local-Magnetic-Field-Dependent Active-Feedback MR

Active-feedback phase φ is a tunable factor defined from 0° to 180° . It influences the spin evolution since it determines the angle between $\vec{B}_{+,AF}$ and $\vec{m}_+(\vec{r}, t)$. For any $\varphi > 180^\circ$, it controls the spin evolution the same way with $\varphi - 180^\circ$. $90^\circ < \varphi \leq 180^\circ$ is called positive phase since $\vec{B}_{+,AF}$ is behind $\langle \vec{m}_+(\vec{r}, t) \rangle$ and drives the magnetization toward $+z$. The lag of $\vec{B}_{+,AF}$ is 90° at $\varphi = 180^\circ$. $0^\circ \leq \varphi < 90^\circ$ is called negative phase since $\vec{B}_{+,AF}$ is ahead of $\langle \vec{m}_+(\vec{r}, t) \rangle$ and drives the magnetization toward $-z$. $\vec{B}_{+,AF}$ is 90° ahead of $\langle \vec{m}_+(\vec{r}, t) \rangle$ at $\varphi = 0^\circ$. $\vec{B}_{+,AF}$ is aligned with $\langle \vec{m}_+(\vec{r}, t) \rangle$ when $\varphi = 90^\circ$. Because spins are tilted to $\pm z$ at different speeds when they have different active-feedback phases, this phase factor can effectively control the spin evolution.

Recent studies have shown that the early-stage GBM blood-oxygen saturation is slightly higher than that of normal brain tissue due to an increase in blood supply and a lower oxygen extraction fraction^{4,24}, resulting in a lower level of the deoxygenated hemoglobin (deoxy-Hb)⁷ and lower blood-oxygen saturation level. Moreover, increased vascular size has been found in early-stage GBM along with a lower vascular density^{3,12}. Such abnormal developments induce a local magnetic field variation that is characterized by^{14,26}:

Outside blood vessel:

$$B_v = 2\pi\Delta\chi * \text{Hct} * (1 - Y)B_0\sin^2(\theta) \left(\frac{a}{r}\right)^2 \cos(2\varphi) \quad (2a)$$

Inside blood vessel:

$$B_v = 2\pi\Delta\chi * \text{Hct} * (1 - Y)B_0(3\cos^2(\theta) - 1)/3 \quad (2b)$$

The deoxy-Hb-induced field is aligned with the external Zeeman field B_0 ; Y is the blood-oxygen saturation; Hct is the hematocrit; $\Delta\chi$ is the susceptibility difference between fully oxygenated and fully deoxygenated hemoglobin; a is the blood-vessel radius; r is the distance between a point of interest and the center of the cylinder cross section and θ is the vessel orientation.

In previous work, the AFF is identical at any point in time despite the variations in local environment because the active-feedback phase and active-feedback strength are independent of time and location. Therefore, spins at different locations feel the same AFF, as shown in figure 2(a). In this work, the AFF is altered to be local-magnetic-field sensitive by making the active-feedback phase local-magnetic-field dependent. Specifically, the active-feedback phase will be modified based on the magnitude of the local field, as shown in figure 2(b).

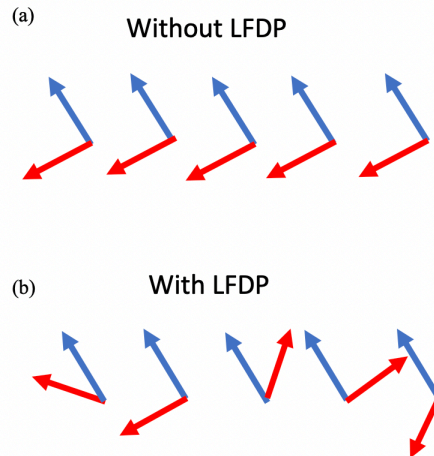


Figure 2. Graphic description of the active-feedback phase with and without local-magnetic-field dependence. (a) Active-feedback phase is local-magnetic-field independent and is the same at any

point. (b) Active-feedback phase is local-magnetic-field dependent. The phase is altered based on the local magnetic field.

The local field distribution in different tissues differs if the level of deoxy-Hb is different. Figure 1 shows the frequency distribution in different tissues with a 0.02 difference in oxygen saturation ($Y = 0.6$ and 0.62 , $a = 5.3\mu\text{m}$, $f = 6\%$). Red and blue bars represent the frequency distribution with $Y = 0.62$ and $Y = 0.6$, respectively. Such a distribution disparity results in a difference in spin population represented by black bars. As a result, it is natural to take advantage of the distribution and population differences to further enhance contrast. This goal is achieved by making the AFF dependent on the local frequency so that it is more sensitive to the frequency shift and is able to increase the selective self-excitation effect. The active-feedback phase is linearly dependent on the local frequency as shown by the blue line in figure 3.

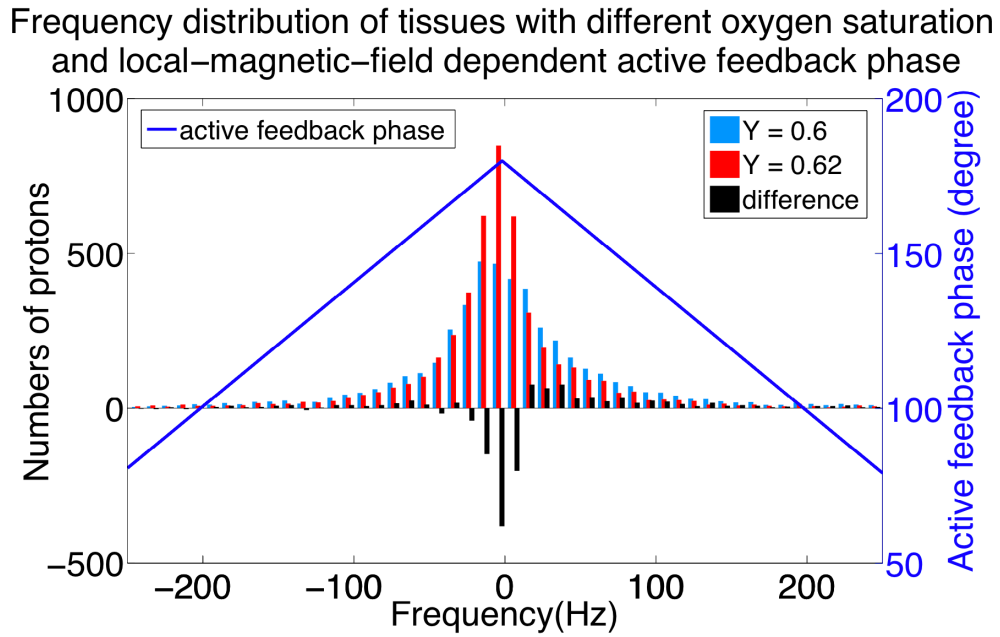


Figure 3. Graphic description of the local-magnetic-field dependent active-feedback phase (blue line) and frequency distribution with different blood-oxygen saturation. $Y = 0.6$ (blue bar) and $Y = 0.62$ (red bar). Difference in frequency distribution (black bar). The active-feedback phase is linearly dependent on local frequency.

To create an AFF that depends on the local magnetic field, we make the active-feedback phase local-magnetic-field dependent. Concretely, the active-feedback phase is assigned different values based on the magnitude of the local field, as shown in figure 2 (blue line). The dependence of the active-feedback phase φ on local field B_v is characterized by:

$$\varphi = k \times \gamma |B_v| + c \quad (3)$$

where γ is the gyromagnetic ratio and k is the sensitivity of the dependence. The larger k is, the more sensitive the active-feedback phase is to the local magnetic field inhomogeneity. c is the intercept that controls the active-feedback phase of bulk water spin with 0Hz frequency. The absolute value of B_v was taken because we mainly care about the frequency shift from which contrast originates, and the direction of the local field does not have any effect on the contrast generating.

4.2.3 Monte Carlo Simulation and Tumor Model

A multi-cylinder vascular model was introduced in Chapter 3. Randomly oriented blood vessels containing deoxy-Hb are modeled as long cylinders with radius a ^{26,27}, as shown in the center voxel in figure 4. The center voxel is area of interest. 100 extra voxels free from deoxy-Hb induced magnetic field are used to model bulk water 1H proton effect^{25,28}. Each voxel contains 8000 ¹H spins that are initially located on a $20 \times 20 \times 20$ grid. Each spin undergoes a three-dimensional random walk with walking step $\sqrt{6D\Delta t}$. where D is the diffusion coefficient and

the step time $\Delta t = 0.1\text{ms}$. The size of each voxel is $30 \times 30 \times 30 \mu\text{m}^3$. The water permeability is neglected to reduce computational cost¹⁰. Detailed model was discussed in Chapter 3.

Early-stage GBM was found to be hyperoxic despite hypermetabolism due to high supply of oxygen to rapidly growing tumor. The oxygen saturation in tumor center was found to be higher than surrounding normal tissue using both computational method and histology measurements^{4,24}. The oxygenation level $Y = 0.6$ in normal tissue and $Y = 0.67$ in tumor tissue was used to calculate the deoxy-Hb induced magnetic field.

Irregular microvascular development was found in early-stage GBM by histology measurements⁵. The early-stage vessel size in a tumor is significantly higher than that in the contralateral striatum at early-stage. It keeps increasing in later days along with a decrease in vessel density found at the tumor center^{6,12}. The blood volume fraction remains similar over time to that of the contralateral striatum¹². To model microvasculature, we use blood-vessel radius of $5.3 \mu\text{m}$ in normal tissue, $8.8 \mu\text{m}$ in a tumor and a volume fraction of 3% in both the tumor and normal tissue.

The apparent diffusion coefficient of water was found to increase significantly in early-stage GBM and remains elevated^{12,29}. $D = 7.2 \times 10^{-10} \text{ m}^2/\text{s}$ in normal tissue and $D = 9.7 \times 10^{-10} \text{ m}^2/\text{s}$ in tumor is used to model the ^1H spin diffusion. Table 1 shows the parameters used in modeling normal tissue and early GBM.

Table 1. Parameters used to model early-stage GBM and healthy tissue.

Parameter	Normal tissue	Early GBM
blood-vessel radius, a (μm)	5.3	8.8
blood volume fraction, f (%)	6.0	6.0
Oxygenation saturation, Y	0.60	0.67
diffusion coefficient, D ($10^{-10} \text{ m}^2/\text{s}$)	7.2	9.7

4.3 Results and Discussion

4.3.1 Effect of Active-Feedback Phase on Selective Self-Excitation

To demonstrate how the active-feedback phase affects the spin evolution, the evolution of one spin was first simulated. The active-feedback time constant $\tau_{AF} = 5\text{ms}$. Results are shown in figure 3. The spin under different active-feedback phases is tilted to different directions at different speeds.

As illustrated in figure 4(a)(b), when the spin has a positive active-feedback phase ($\varphi > 90^\circ$), the magnetization is driven to the $+z$ direction since the AFF $\vec{B}_{+,AF}$ is behind M_{xy} . However, with a different angle between the field vector and transverse magnetization vector, spin is driven at different speeds. As shown in figure 4(a), when $\varphi = 180^\circ$, the angle between the two vectors is 90° and M_z is tilted to $+z$ the fastest, which indicates the most efficient excitation. As φ decreases to 120° , shown in figure 4(b), it takes a longer time to reach the $+z$ direction compared with a 180° phase since the angle is smaller and spin keeps rotating on the Bloch sphere. Spin evolves to $-z$ direction with negative active-feedback phase ($\varphi < 90^\circ$). As shown in figure 4(d), when $\varphi = 0^\circ$, $\vec{B}_{+,AF}$ is 90° ahead of M_{xy} and effectively drives the spin toward the $-z$

direction. Although it is not shown, with an active-feedback phase of 0° , the spin should be tilted toward the $-z$ direction more effectively than any other negative phases. At the special case with $\varphi = 90^\circ$, the angle between AFF vector and M_{xy} is zero all the time resulting in an AFF that cannot be felt by the spins. Therefore, M_z remains unchanged with an active-feedback phase 90° as shown in figure 4(c).

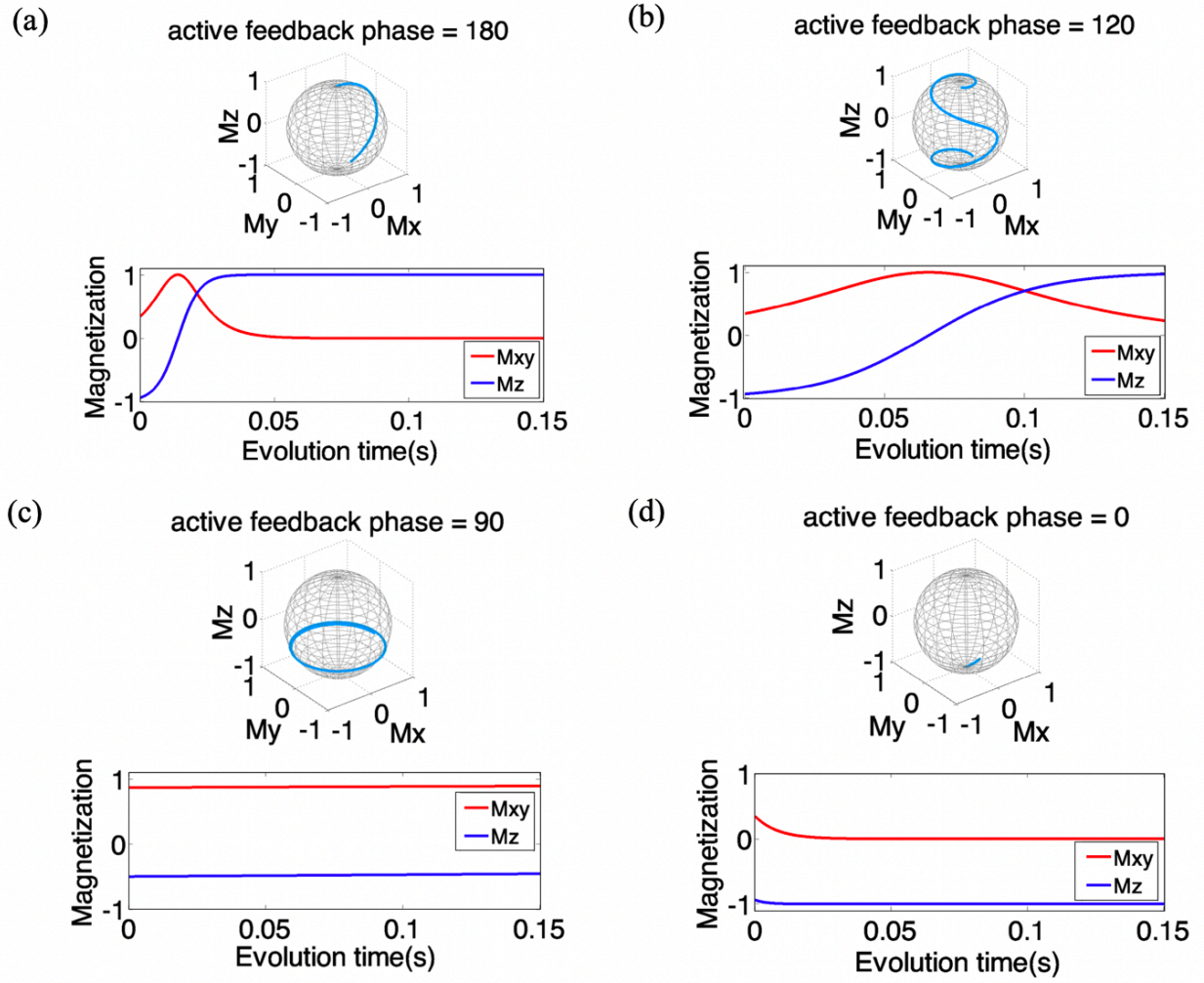


Figure 4. The evolution of one spin with different feedback phases. $\tau_{AF} = 5\text{ms}$. (a) $\varphi = 180^\circ$. The spin is driven to the $+z$ direction within 0.05s. (b) $\varphi = 120^\circ$. The spin is driven to the $+z$

direction but at a slower rate with a rotation around the z axis. (c) $\varphi = 90^\circ$. The pin rotates in the transverse plane and is hardly tilted away from its original position. (d) $\varphi = 0^\circ$. The spin is driven to the -z direction without any rotation around the z axis.

The changing rate of longitudinal magnetization is the largest with a 90° angle between the field vector and the transverse magnetization vector ($\varphi = 0^\circ$ or 180°) and the changing rate is decreasing with a smaller angle when the active-feedback phase is further away from 0° or 180° . Thus, it takes a longer time to fully develop the longitudinal magnetization with an active-feedback phase other than 0° or 180° .

To understand the effect of the active-feedback phase on selective self-excitation and contrast development, two spin packets were assigned with different active-feedback phase. The active-feedback time constant $\tau_{AF} = 5\text{ms}$.

A total number of 100 spins are distributed into two packets with a 50Hz frequency offset. One packet with a frequency of 0Hz consists of 90 spins. The other packet with a frequency of 50Hz consists of 10 spins. The spin packet with 90 spins contributes 90% to the average transverse magnetization, which makes the frequency of the AFF match their precession frequency. Therefore, they are on-resonance with the AFF. The packet with 10 spins contributes only 10% and will be off-resonance due to frequency mismatch. Spins in the two packets are denoted as “on-resonance” and “off-resonance” respectively. The on-resonance spin packet always has a positive active-feedback phase 180° while the off-resonance spin packet has a different active-feedback phase. The active-feedback phase of the off-resonance spin packet is set to 180° , 120° , 90° , 0° . Simulation results are shown in figure 5.

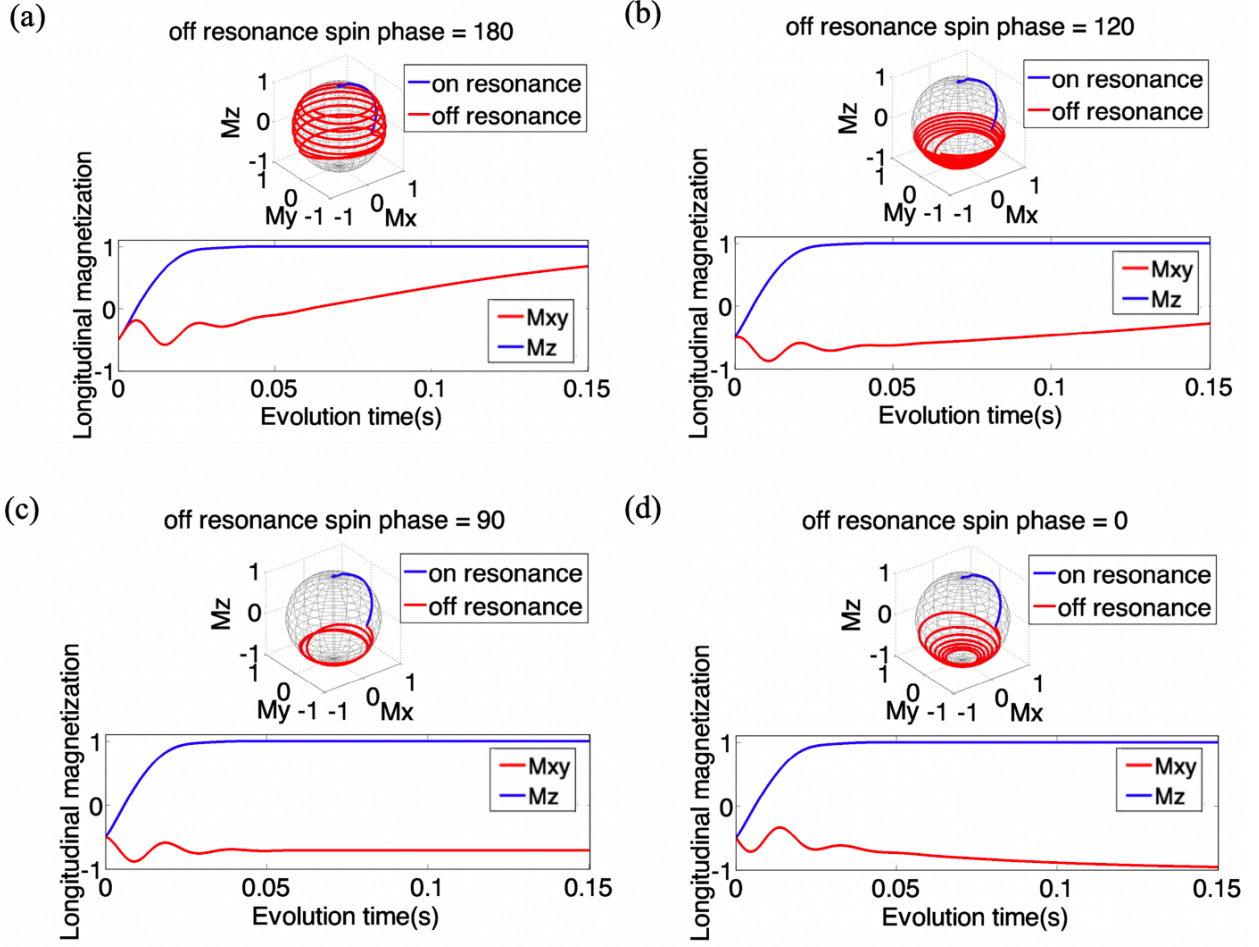


Figure 5. The evolution of two spin packets with different active-feedback phases (100 spins, 90 on-resonance spins and 10 off-resonance spins, frequency offset = 50Hz). On-resonance spins have an active-feedback phase $\varphi = 180^\circ$. Off-resonance spins have different active-feedback phases. Active-feedback time constant $\tau_{AF} = 5\text{ms}$. (a) Off-resonance spins with $\varphi = 180^\circ$. Spins in both packets are tilted up. On-resonance spins are tilted to $+z$ faster than the off-resonance ones and a contrast along the z direction is created. (b) Off-resonance spins with $\varphi = 120^\circ$. Both on- and off-resonance spins are driven up. Off-resonance spins are tilted to $+z$ much more slowly than the on-resonance spins. (c) Off-resonance spins with $\varphi = 90^\circ$. On-resonance spins are effectively excited while off-resonance spins rotate around the z axis without any magnetization development in the z direction. (d) Off-resonance spins with $\varphi = 0^\circ$. On and off-resonance spins are excited

toward opposite directions. On-resonance spins are tilted to $+z$ with a positive phase and off-resonance spins are driven to $-z$ due to a negative phase.

Figure 5(a) shows the spin evolution with a positive active-feedback phase 180° assigned to both on-resonance and off-resonance spins. This is the same as in the previous work where active-feedback is the same for all spins despite their location and local magnetic field. On-resonance spins are excited to fixed point along $+z$ faster than off-resonance spins as expected due to the selective self-excitation. A small contrast along the z direction is generated. As shown in figure 5(b), when off-resonance spins have an active-feedback phase of 120° , both on-resonance spins and off-resonance spins are tilted up since $\varphi > 90^\circ$ for both. However, as compared to the case in which off-resonance spins have a 180° active-feedback phase, with $\varphi = 120^\circ$, the off-resonance spins are driven up less effectively. As explained earlier, $\varphi = 180^\circ$ has the strongest longitudinal effect on spin evolution. Under the same evolving time, the off-resonance spins with 120° phase move more slowly than with a 180° phase, which provides a greater contrast. As shown in figure 5(c), when off-resonance spins have $\varphi = 90^\circ$, they are hardly excited by the AFF since the field is aligned with the average transverse magnetization. With a positive phase, on-resonance spins are tilted up effectively while the off-resonance spins are tilted in the opposite direction when they have a negative phase with $\varphi = 0^\circ$ as shown in figure 5(d). Since the two spin packets are evolving in different directions, it creates the largest contrast among all cases with different active-feedback phase assigned to off-resonance spins.

As shown by the simulation, the contrast generating process through selective self-excitation is more effective when on-resonance spins and off-resonance spins have a greater active-feedback phase disparity and the most effective selective self-excitation process happens when on-

resonance spins and off-resonance spins are driven in opposite directions with active-feedback phase 180° and 0° , respectively.

When the on-resonance spins make contributions to the average transverse magnetization, the off-resonance spins are not excited and keep rotating around the z axis. After on-resonance spins reach the fixed point along z, their contribution to the average transverse magnetization disappears, which leaves the off-resonance spins as the major contributor. Thus, off-resonance spins meet the on-resonance condition and are excited due to the selective self-excitation process. As shown in figure 4, off-resonance spins are only excited after 0.02s when the on-resonance spins stay at +z with zero contribution to the average transverse magnetization.

We do not make the active-feedback time constant local-magnetic-field dependent mainly because it cannot affect the spin evolution in a way that enhances contrast. First, the effect of active-feedback strength on spin separation is not as obvious as that of active-feedback phase. The active-feedback time constant controls the active-feedback strength, which influences evolution of all the spins in the same way. The spin is tilted by the AFF at a faster speed when the active-feedback strength is greater, and is slowly tilted when the strength is small. Second, it is extremely difficult to find the optimal dependence. A higher strength does not promise a greater contrast because quick spin evolution to a fixed point will decrease the active-feedback filed at a fast rate and shorten the selective self-excitation process. Thus, a high AFF strength may hinder the accumulation of contrast.

4.3.2 MR Contrast with Local-Magnetic-Field-Dependent Active-Feedback Field

We introduced the local-magnetic-field dependent active-feedback MR through local-magnetic-field dependent active-feedback phase. The phase is characterized by $\varphi = k \times \gamma |B_v| + c$ where $|B_v|$ is the magnitude of the deoxy-Hb-induced field, c is the active-feedback phase in

the absence of the local magnetic field or when the net local magnetic field is zero, as shown in figure 1. Here c was set to 180° because we want the on-resonance spins to be tilted up most effectively to create greater contrast.

This method is first carried out on a multi-cylinder model with different blood-oxygen saturation $Y = 0.6$ and 0.62 , same blood-vessel radius $a = 5.3\mu\text{m}$, same diffusion coefficient $D = 6.64 \times 10^{-10} \text{ m}^2/\text{s}$, and same blood volume fraction $f = 6\%$. Figure 6 shows the simulation results for spin echo method (SE, $TE = 100\text{ms}$), gradient echo method (GRE, $TE = 40\text{ms}$), active-feedback method without local-magnetic-field dependent (AF, $t_{AF} = 2\text{ms}$) and active-feedback method with local-magnetic-field dependent (local-field dependent AF, $t_{AF} = 2\text{ms}$). The relaxation time and maximum contrast for the four different methods are shown in table 2. Maximum contrast is compared with the spin echo method by comparing the maximum contrast between the alternative method and the spin echo method.

The decay of transverse magnetization under the spin echo method is shown in figure 6(a) and the contrast is shown in figure 6(b). The curves decays rapidly with relaxation time $T_{0.6} = 30.5\text{ms}$, $T_{0.62} = 31.8\text{ms}$. The contrast reaches 0.016 at 0.02s and decay to zero within 0.1s. The decay of transverse magnetization under the gradient echo method and corresponding contrast is shown in figure 6(c) and (d). The relaxation times are $T_{0.6} = 25.7\text{ms}$, $T_{0.62} = 28.8\text{ms}$. The maximum contrast 0.02 appears at 0.02s and decreases rapidly after that. The decay of longitudinal magnetization under active-feedback method without local-magnetic-field ($\tau_{AF} = 8\text{ms}$, $\varphi = 180^\circ$) and corresponding contrast are shown in figure 6(e) and (f). The decay is much slower with $T_{0.6} = 1.51\text{s}$, $T_{0.62} = 1.66\text{s}$, which allows a full contrast development. The maximum contrast is 0.032 and is enhanced 2.0 times as compared to that under spin echo method. Shown in figure 6(g) and (h), when using the active-feedback method with local-magnetic-field ($\tau_{AF} = 8\text{ms}$, $k = -3.5$,

$c = 180^\circ$), although the relaxation time does not change much ($T_{0.6} = 1.14\text{s}$, $T_{0.62} = 1.53\text{s}$), the maximum contrast achieves 0.135, which enhances the contrast by 4.2 times when it is compared with active-feedback without local-field dependence. With only 3% change in blood-oxygen level, the contrast is enhanced 8.4 times and 2 times using the active-feedback method with and without the local-magnetic-field dependent phase while there is nearly no improvement using the gradient echo method.

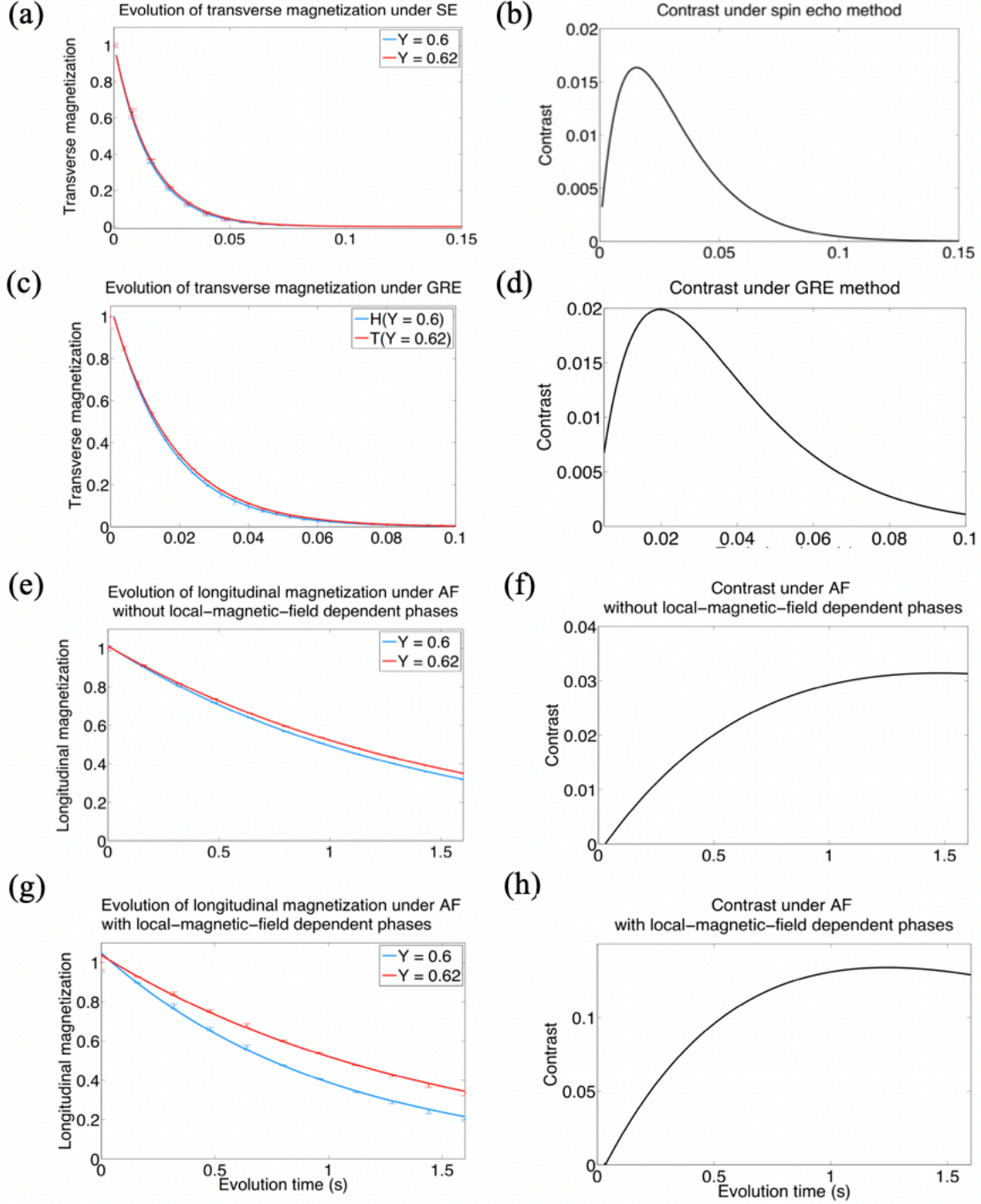


Figure 6. Decay of magnetization of tissues with different oxygen saturation levels and the contrast using different MR methods. $Y = 0.6$ and $Y = 0.62$, $a = 5.3\mu m$, $D = 6.64 \times 10^{-10} m^2/s$, $f = 6\%$. (a) Plot of transverse magnetization under the spin echo method ($TE = 100ms$). (b) The

contrast resulting from the spin echo method. (c) Plot of transverse magnetization under the gradient echo method (TE = 40ms). (d) The contrast resulting from the GRE. Plot of longitudinal magnetization under the active-feedback method (e) without local-magnetic-field dependence, $\tau_{AF} = 8\text{ms}$, $\varphi = 180^\circ$ and (g) with local-magnetic-field dependence. $\tau_{AF} = 8\text{ms}$, $k = -3.5$, $c = 180^\circ$. The contrast resulting from the active-feedback method (f) without local-magnetic-field dependence and (h) with local-magnetic-field dependence.

Table 2. Simulation results of tissues with different blood-oxygen saturation ($Y = 0.6$ and $Y = 0.62$) using the spin echo, gradient echo, and the active-feedback methods with and without local-magnetic-field dependent phases. The contrast enhancement is calculated by:

Max contrast(alternative method)/Max contrast(SE).

method	relaxation time(AF)	Max contrast	Enhancement
SE	$T_{0.6} = 30.5\text{ms}$, $T_{0.62} = 31.8\text{ms}$	0.016	-
GRE	$T_{0.6} = 25.7\text{ms}$, $T_{0.62} = 28.8\text{ms}$	0.020	1.3
AF	$T_{0.6} = 1.51\text{s}$, $T_{0.62} = 1.66\text{s}$	0.032	2.0
Local-field dependent AF	$T_{0.6} = 1.14\text{s}$, $T_{0.62} = 1.53\text{s}$	0.135	8.4

The slope k was set to different negative values to test the local-magnetic-field dependent active-feedback MR. Negative slope was applied to make sure that spin with large shift from the on-resonance condition will have a small positive or negative phase in order to enhance contrast. Maximum contrast under local-magnetic-field dependent active-feedback MR with different slopes is shown in figure 7. $\tau_{AF} = 8\text{ms}$, $c = 180^\circ$.

The largest contrast reaches 0.135 at $k = -3.5$. Further decreasing or increasing the slope diminishes the contrast. To understand the optimal slope, the different frequency distributions with different blood-oxygen level ($Y = 0.6$ and $Y = 0.62$) should be examined. As shown in figure 1, the major population differences appear around 0Hz (on-resonance) and $\pm 50\text{Hz}$ (off-resonance). Ideally, we would want on-resonance spins to have positive active-feedback phase 180° and off-resonance spins to have negative active-feedback phase 0° so they are driven to opposite directions to obtain the greatest contrast. Indeed, the slope $k = -3.5$ and intercept $c = 180^\circ$ that provides the largest contrast gives $\varphi = 5^\circ$ at $\pm 50\text{Hz}$ and $\varphi = 180^\circ$ at 0Hz. As the slope is increased or decreased, the active-feedback phase associated with $\pm 50\text{Hz}$ is greater than 5° , which hinders the contrast generating process by selective self-excitation.

$k = 0$ resulting $\varphi = 180^\circ$ everywhere despite the variation in local magnetic field, is equivalent to active-feedback MR without local-magnetic-field dependent phases. Indeed, the same maximum contrast 0.032 was obtained with $k = 0$.

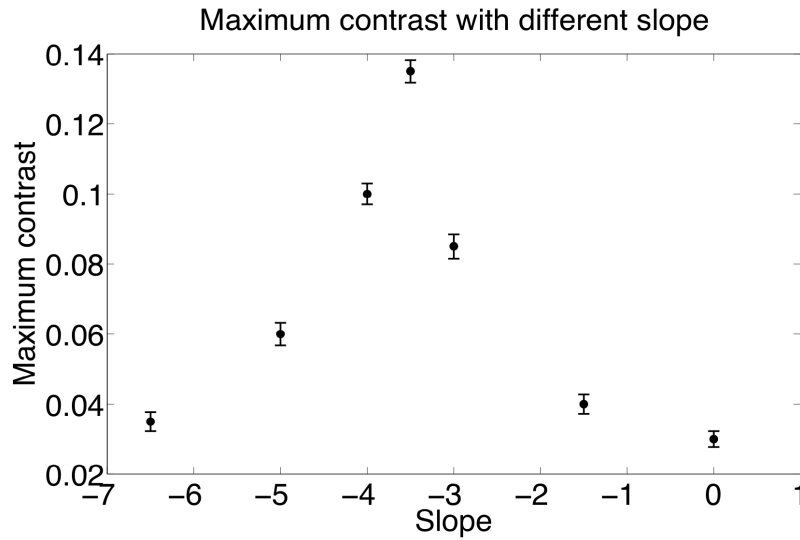


Figure 7. The plot of maximum contrast under local-magnetic-field dependent active-feedback MR with different slopes. $c = 180^\circ$, $\tau_{AF} = 8\text{ms}$. Largest contrast 0.0135 appears at $k = -3.5$. Contrast was decreased when the slope is increased or decreased. Contrast is 0.032 when $k = 0$, which matches the contrast generating from the active-feedback method without local magnetic field dependence.

The enhancement in contrast with local-magnetic-field dependent active-feedback MR is achieved in two ways. First, consider spins that have a frequency close to but not exactly at the on-resonance frequency. These spins have a chance to be excited as well due to the fact that they have some contribution to the AFF and they can control the field behavior once on-resonance spins reach the fixed point. Hence, instead of exciting a single frequency, the selective self-excitation process has a selection band. With local-magnetic-field dependent active-feedback MR, spins that are close to but different from the on-resonance frequency will have an active-feedback phase slightly different from 180° . So they are less likely to be excited in comparison with having a 180° active-feedback phase, which results in a narrower selection band and a more restricted on-resonance condition. Second, consider the spins that are far away from the on-resonance frequency. After the on-resonance spins reach their fixed point and stop contributing to the AFF, the off-resonance spins will meet the on-resonance condition and be excited. Due to the negative slope, those off-resonance spins have a small positive or negative active-feedback phase, resulting in a less effective excitation or excitation in the opposite direction. Consequently, further contrast enhancement is achieved.

The choice of the active-feedback phase functional form should follow several principles. Most importantly, it should be able to help distinguish the on-resonance spins from the off-

resonance spins, which means it should be able to generate different phases at different frequencies. Larger phase disparity between on-resonance and off-resonance spins will provide better contrast. Specifically, if the phase at on-resonance frequency is 180° , it is better to generate 0° phases at the off-resonance frequency. Moreover, a good functional form should enable active-feedback phases to be tuned flexibly and the optimal setup to be found easily. Since the local-magnetic-field dependent active-feedback MR takes advantage of different frequency distributions and spin populations in tissues to improve the contrast, it is crucial that the adjustment of phase is flexible so the optimal dependence on local field can be found without knowing the frequency distribution beforehand. Lastly, the functional form should be engineering feasible to apply to electronic devices.

4.3.3 Contrast enhancement in Early-Stage GBM

Now we apply the local-magnetic-field dependent active-feedback MR in the early-stage GBM model. Parameters $Y = 0.6$, $a = 5.3\mu\text{m}$, $f = 3\%$, $D = 7.2 \times 10^{-10} \text{ m}^2/\text{s}$ were used in normal tissue and $Y = 0.67$, $a = 8.8\mu\text{m}$, $f = 3\%$, $D = 9.7 \times 10^{-10} \text{ m}^2/\text{s}$ were used in an early-stage GBM brain tumor. The spin frequency distribution of the early-stage GBM tumor and normal tissue are shown in figure 8. The tumor centered at 1Hz with FWHM 23Hz is represented by red bars and normal tissue is centered at 3Hz with FWHM 31Hz and represented by blue bars. The difference in spin populations resulting from the frequency shift is obvious, shown by the black bars. The tumor has more spins within a small frequency shift (10Hz) while normal tissue has more spin within a frequency shift range 20Hz to 60Hz.

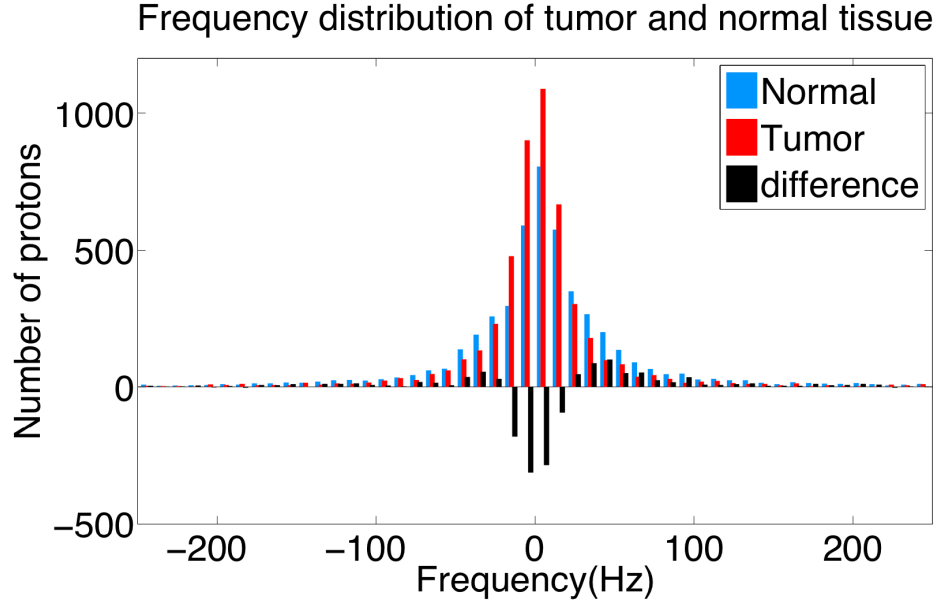


Figure 8. Frequency distribution of early-stage GBM and normal tissue and the difference. Frequency distribution of tumor (red bars) is centered at 1Hz with FWHM 23Hz and distribution of normal tissue (blue bars) is centered at 3Hz with FWHM 31Hz. The major differences (black bars) appear at -10 to +10 and 20 to 60Hz. Tumor has more spins within a small frequency shift (10Hz) as compared to normal tissue while normal tissue has more spin with a frequency shift range from 20 to 60Hz.

Simulation results are shown in figure 9. Relaxation time and contrast are shown in table 3. Under the spin echo method (SE, $TE = 100\text{ms}$), the transverse magnetization decays to 0 rapidly, which results in a small contrast peaking at 0.042, as shown in figure 9(a)(b). Figure 9(c) and (d) shows the transverse magnetization under the gradient echo sequence and the corresponding contrast. The contrast reaches its maximum of 0.058 at 0.02s and decreases to zero within 0.1s. The decay of the longitudinal magnetization is much slower in the presence of the AFF. Results for the field-independent active-feedback method ($t_{AF} = 2\text{ms}$, $\tau_{AF} = 8\text{ms}$, $\varphi = 180^\circ$) are shown

in figures 9(e) and (f), the maximum contrast appears around 0.130 with a 3.1 times enhancement when compared with the spin echo method and the contrast develops steadily and persists at a high level. Figures 9(g) and (h) show the decay of longitudinal magnetization and contrast under local-magnetic-field dependent active-feedback MR ($t_{AF} = 2\text{ms}$, $\tau_{AF} = 8\text{ms}$, $k = -3.7$, $c = 180^\circ$). The contrast is dramatically improved with the maximum value 0.301, which is 7.2 times greater as compared with spin echo method. The slope that characterizes the active-feedback phase dependence is -3.7 when the best results were generated. With $k = -3.7$ and $c = 180^\circ$, spins that have a frequency shift within 10Hz have active-feedback phase close to 180° . The active-feedback phase experienced by spins with a 20Hz shift is 106° and becomes negative ($0^\circ \leq \varphi < 90^\circ$) when the frequency shift ranges from 24Hz to 49Hz.

The effect of such phase disparity is revealed in the relaxation time. Although the relaxation time of a tumor using the field-dependent and independent active-feedback methods do not differ much. Relaxation time 1.81s with field-dependence as compare to 1.73s without field-dependence, the normal tissue decays much faster using the field-dependent active-feedback method, with a relaxation time 0.79s as compared to 1.23s without field dependence. This indicates that the local-field dependent phase successfully excites the normal tissue that has greater frequency shift to the opposite direction. Contrast is further enhanced 2.3 times in comparison with the traditional active-feedback method which is independent of the local field.

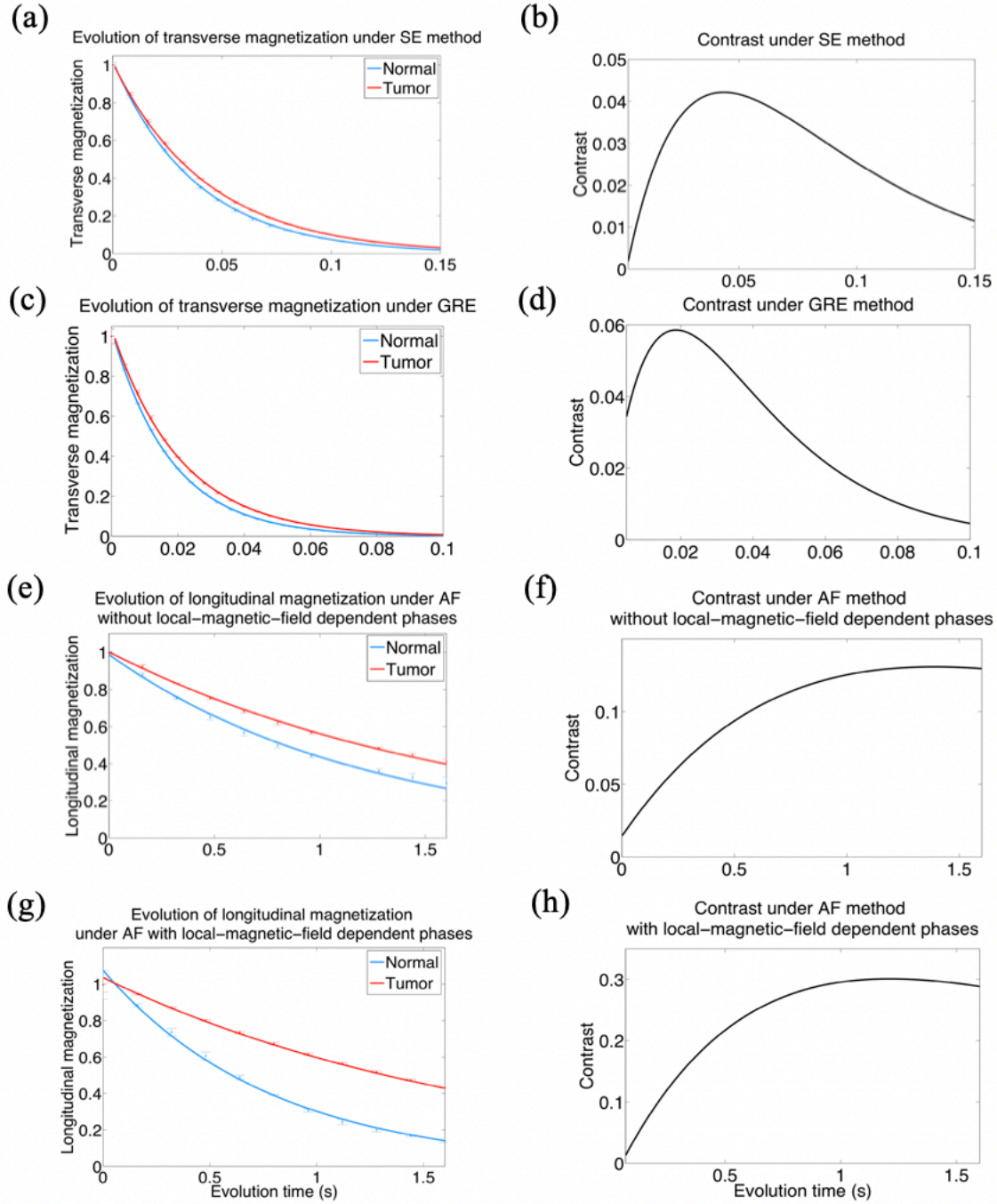


Figure 9. Simulation results of normal tissue and early-stage GBM using the spin echo method, gradient echo method, active-feedback method with and without local-magnetic-field dependent phases. (a) Transverse magnetization under spin echo method ($TE = 100\text{ms}$). (b) Contrast under the spin echo method, maximum contrast is 0.042. (c) Plot of transverse magnetization using the

gradient echo method ($TE = 40\text{ms}$). (d) Contrast generated using the gradient echo method. Maximum contrast is 0.058. (e) Longitudinal magnetization under the active-feedback method without field-dependence ($\tau_{AF} = 8\text{ms}$, $\varphi = 180^\circ$). (f) Contrast generated under the active-feedback method without field-dependence. Maximum value is 0.130. (g) Longitudinal magnetization with the local-magnetic-field-dependent active-feedback method ($\tau_{AF} = 8\text{ms}$, $k = -3.7$, $c = 180^\circ$). (h) Contrast under the local-magnetic-field-dependent active-feedback method. Maximum contrast is 0.301.

Table 3. Relaxation and contrast for normal tissue and early-stage GBM using the spin echo, the gradient echo, and the active-feedback methods with and without local-magnetic-field dependent phases. The contrast enhancement is calculated by:

Max contrast(alternative method)/Max contrast(SE).

method	relaxation time(AF)	Max contrast	Enhancement
SE	$T_{\text{normal}} = 38.1\text{ms}$, $T_{\text{tumor}} = 43.0\text{ms}$	0.042	-
GRE	$T_{\text{normal}} = 32.6\text{ms}$, $T_{\text{tumor}} = 39.2\text{ms}$	0.058	1.4
AF	$T_{\text{normal}} = 1.23\text{s}$, $T_{\text{tumor}} = 1.73\text{s}$	0.130	3.1
Local-field dependent AF	$T_{\text{normal}} = 0.79\text{s}$, $T_{\text{tumor}} = 1.81\text{s}$	0.301	7.2

4.4 Conclusions

In this work, a novel MR technique “local-magnetic-field dependent active-feedback MR” is established to further improve contrast. The local-magnetic-field dependent feature is achieved by manipulating the active-feedback phase, which controls spin evolution. This work has shown

that the local-magnetic-field dependent active-feedback MR is highly sensitive to small variations in the local field. The enhanced contrast originates from a narrower selection band and a less effective excitation due to the phase disparity.

Monte Carlo simulations showed that contrast was further enhanced 4.2 times in comparison with the traditional active-feedback method and 8.4 times in comparison with the spin echo method with only 3% change in blood-oxygen saturation. This method was also applied to early-stage GBM model to show potential clinical application. A robust contrast was generated using the local-magnetic-field dependent active-feedback MR. Maximum contrast 0.301 was reached which is 7.2 times greater than the spin echo method and 2.3 times greater than the active-feedback method without a local-field-dependent phase. The robust contrast and huge contrast enhancement makes the detection of early-stage GBM possible in clinics.

References

- [1] Louis, D. N., Ohgaki, H., Wiestler, O. D., Cavenee, W. K., Burger, P. C., Jouvet, A., Scheithauer, B. W. Kleihues, P. The 2007 WHO classification of tumours of the central nervous system. *Acta Neuropathol* 2007, 114, 97-109.
- [2] Bleeker, F. E., Molenaar, R. J., Leenstra, S. Recent advances in the molecular understanding of glioblastoma. *Journal of Neuro-Oncology* 2012, 108(1), 11-27.
- [3] Bouchet, A., Bidart, M., Miladi, I., Le Clec'h, C., Serduc, R., Coutton, C., Regnard, P., Khalil, E., Dufort, S., Lemasson, B., Laissue, J., Pelletier, L. Le Duc, G. Characterization of the 9L gliosarcoma implanted in the Fischer rat: An orthotopic model for a grade IV brain tumor. *Tumor Biology* 2014, 35(7), 6221-6233.
- [4] Chakhoyan, A., Corroyer-Dulmont, A., Leblond, M. M., G rault, A., Toutain, J., Chazaviel, L., Divoux, D., Petit, E., MacKenzie, E. T., Kauffmann, F., Delcroix, N., Bernaudin, M., Touzani, O. Carbogen-induced increases in tumor oxygenation depend on the vascular status of the tumor: A multiparametric MRI study in two rat glioblastoma models. *Journal of Cerebral Blood Flow and Metabolism* 2017, 37(6), 2270-2282.
- [5] Farrell, C. L., Farrell, C. R., Stewart, P. A., Del Maestro, R. F., Ellis, C. G. The functional microcirculation in a glioma model. *International Journal of Radiation Biology* 1991, 60(2), 131-137.
- [6] Farrar, C. T., Kamoun, W. S., Ley, C. D., Kim, Y. R. Kwon, S. J., Dai, G. P., Rosen, B. R., Tomaso, E., Jain, R. K., Sorensen, A. G. In vivo validation of MRI vessel caliber index measurement methods with intravital optical. *Neuro-Oncology* 2010, 12(4), 341-350.

- [7] Biswal, N. C., Xu, Y., Zhu, Q. Imaging Tumor Oxyhemoglobin and Deoxyhemoglobin Concentrations with Ultrasound-Guided Diffuse Optical Tomography. *Technology in Cancer Research & Treatment* 2013, 10(5), 417-429.
- [8] Thulborn, K. R., Waterton, J. C., Matthews, P. M., Radda, G. K. Oxygenation dependence of the transverse relaxation time of water protons in whole blood at high field. *BBA - General Subjects* 1982, 714(2), 265-270.
- [9] Bren, K. L., Eisenberg, R., Gray, H. B. Discovery of the magnetic behavior of hemoglobin: A beginning of bioinorganic chemistry. *Proceedings of the National Academy of Sciences* 2015, 112(43), 13123-13127.
- [10] Weisskoff, R., Zuo, C. S., Boxerman, J. L., Rosen, B. R. Microscopic susceptibility variation and transverse relaxation: Theory and experiment. *Magnetic Resonance in Medicine* 1994, 31(6), 601-610.
- [11] Pauling, L., Coryell, C. D. The magnetic properties and structure of hemoglobin, oxyhemoglobin and carbonmonoxy hemoglobin. *Proc Natl Acad Sci* 1936, 22, 210-216.
- [12] Valable, S., Lemasson, B., Farion, R., Beaumont, M., Segebarth, C., Remy, C., Barbier, E. L. Assessment of blood volume, vessel size, and the expression of angiogenic factors in two rat glioma models: a longitudinal in vivo and ex vivo study. *NMR in Biomedicine* 2007, 21, 1043-1056.
- [13] Boxerman, J. L., Hamberg, L. M., Rosen, B. R., Weisskoff, R. M. MR Contrast Due to Intravascular Magnetic Susceptibility Perturbations. *Magnetic Resonance in Medicine* 1995, 34(4), 555-566.
- [14] Yablonskiy, D. A., Haacke, E. M. Theory of NMR Signal Behavior in Inhomogeneous Tissues: The Static Dephasing Regime. *Magnetic Resonance in Medicine* 1994, 32, 749-763.

- [15] Ideguchi, M., Kajiware, K., Goto, H., Sugimoto, K., Nomura, S., Ikeda, E., Suzuki, M. MRI findings and pathological features in early-stage glioblastoma. *Journal of Neuro-Oncology* 2015, 123(2), 289-297.
- [16] Huang, S. Y., Chung, A. P., Lin, Y. Y. Visualizing Feedback-Enhanced Contrast in Magnetic Resonance Imaging. *Concepts Magn. Reson.* 2007, 36A(6), 378-393.
- [17] Datta, S., Huang, S. Y., Lin, Y. Y. Understanding Spin Turbulence in Solution Magnetic Resonance Through Phase Space Dynamics and Instability. *Concepts Magn. Reson.* 2006, 28A(6), 410-421.
- [18] Huang, S. Y., Anklin, C., Walls, J. D., Lin, Y. Y. Sizable concentration-dependent frequency shifts in solution NMR using sensitive probes. *Journal of the American Chemical Society* 2004, 126(49), 15936-15937.
- [19] Huang, S. Y., Wolahan, S. M., Mathern, G. W., Chute, D. J., Akhtari, M., Nguyen, S. T., Huynh, M. N., Salamon, N. Lin, Y. Y. Improving MRI differentiation of gray and white matter in epileptogenic lesions based on nonlinear feedback. *Magnetic Resonance in Medicine* 2006, 56(4), 776-786.
- [20] Hirscha, N. M., Totha, V., Förschlerb, A., Kooijmanc, H., Zimmera, C., Preibisch, C. Technical considerations on the validity of blood-oxygenation level-dependent-based MR assessment of vascular deoxygenation. *NMR in Biomedicine* 2014, 27(7), 853-862.
- [21] Jeener, J., Vlassenbroek, A., Broekaert, P. Unified derivation of the dipolar field and relaxation terms in the Bloch-Redfield equations of liquid NMR. *The Journal of Chemical Physics* 1995, 103(4), 1309-1332.
- [22] Abergel, D. Chaotic solutions of the feedback driven Bloch equations. *Physics Letters, Section A: General, Atomic and Solid State Physics* 2002, 302(1), 17-22.

- [23] Warren, W. S., Hammes, S. L., Bates, J. L. Dynamics of radiation damping in nuclear magnetic resonance. *Physical Review* 1989, 91(10), 5895.
- [24] Yao, J., Maslov, K. I., Zhang, Y., Xia, Y., Wang, L. v. Label-free oxygen-metabolic photoacoustic microscopy in vivo. *Journal of Biomedical Optics* 2011, 16(7), 076003.
- [25] Li, Y., Srinivasan, R., Ratiney, H., Lu, Y., Chang, S. M. Nelson, S. J. Comparison of T1 and T2 metabolite relaxation times in glioma and normal brain at 3T. *Journal of Magnetic Resonance Imaging* 2008, 28(2), 342-350.
- [26] Ogawa, S., Menon, R. S., Tank, D. W., Kim, S. G., Merkle, H., Ellermann, J. M., Ugurbil, K. Functional brain mapping by blood-oxygenation level-dependent contrast magnetic resonance imaging. *Biophysical journal* 1993, 64, 803-812.
- [27] Uludag, K., Müller-Bierl, B., Ugurbil, K. An integrative model for neuronal activity-induced signal changes for gradient and spin echo functional imaging. *NeuroImage* 2009, 48, 150-165.
- [28] Darwin, R. H., Drayer, B. P., Riederer, S. J., Wang, H. Z., Macfall, J. R. T2 Estimates in Healthy and Diseased Brain Tissue: A Comparison Using Various MR Pulse Sequence. *Radiology* 1986, 160, 375-381.

Chapter 5

Conclusions and Outlook

Since nuclear magnetic resonance was introduced in medical imaging in 1971, it has become one of the most powerful tools in not only diagnostics but also in biomedical research. Doctors and researchers have been exploring and developing novel techniques and have brought many breakthroughs.

In this dissertation, I have proposed another advanced technique called active-feedback magnetic resonance imaging. This technique has been proven to be more sensitive to local environment than other relaxation based MR techniques. Both computer simulation and experiments have shown its feasibility to detect brain tumor at a very early stage. This technique distinguishes itself from the rest in two ways. First, it introduces fixed points and nonlinear spin dynamics and allows spins to be selectively excited. Second, the contrast enhancement mechanism is unique, the MR contrast generated by the active-feedback technique comes from frequency shift while most of the relaxation based techniques produce MR contrast based on different frequency widths. I believe that this novel technique will become one of the leading imaging techniques for detecting early-stage tumor due to its great ability to enhance contrast and broad application in different areas.

However, there are many work need to be done to realize the clinical application of the active-feedback magnetic resonance imaging. Among all, improving the active-feedback electronic device to accurately control the active-feedback phase and the carrying out in vivo experiments to confirm the stability of the technique have the most importance. Moreover, with

the fast development in artificial intelligence, it is also possible to utilize AI techniques such as compressed sensing and machine learning to broaden the research scope.